Die approbierte Originalversion dieser Dissertation ist an der Hauptbibliothek der Technischen Universität Wien aufgestellt (http://www.ub.tuwien.ac.at).

The approved original version of this thesis is available at the main library of the Vienna University of Technology (http://www.ub.tuwien.ac.at/englweb/).

TECHNISCHE
UNIVERSITÄT
WIEN
Vienna University of Technology

DISSERTATION

Experimental and computational micromechanics of mineralized tendon and bone

Under supervision of

Professor Philippe K. Zysset

Institute of Lightweight Design and Structural Biomechanics
at Vienna University of Technology
Department of Mechanical and Industrial Engineering

by

Ewa M. Spiesz, MSc

Vienna, October 2011 Ewa M. Spiesz

Acknowledgments

Colleagues, external partners, my family and friends gave me a lot of support during my stay in Austria and encouraged me in my work on this thesis. My sincerest thanks go to all of them, but I would like to address some people in particular.

First of all, I would like to thank my supervisor Prof. Philippe Zysset for his his enthusiasm and interest in this work. Together with his strong expertize and comprehension in the field of bone biomechanics, it makes him the best teacher.

I would like to thank Dr. Paul Roschger from the Ludwig Boltzman Institute of Osteology for his help with the qBEI measurements, as well as his advise and commitment to preparation of the manuscripts resulting from this thesis.

Part of the work of this thesis was conducted during my stay at the University of Washington in Seattle, WA, where I was supervised by Prof. Werner Kaminsky, who not only hepled me in the scientific way, but also made my stay in the US very interesting and comfortable, which I am very grateful for.

I am also grateful to Prof. Peter Fratzl for evaluating this thesis and for his helpful advise in the early stages of this work.

I would also like to express my gratitude to my colleagues in the ILSB in Vienna for the great working atmosphere and prompt support.

Finally, I would like to thank my husband Przemek and my Parents for the continuous support.

Abstract

In-depth understanding of morphology and micromechanics of bone is important in prediction and treatment of bone metabolic diseases, like osteoporosis - a disease causing high morbidity and mortality among the elderly population. In this thesis, an extensive experimental and computational research program has been achieved in order to better understand the structure-function relationships of mineralized tissues.

Mineralized turkey leg tendon (MTLT) was used in the study, as a mechanical model of mineralized collagen fibers, also present in bone. Quantitative backscattered electron (qBEI) and light microscopy images revealed two morphology zones in this tissue. The zones differed in mineralization, amount of organic phase, size of the mineralized fibers and microporosity, as well as stiffness. A mean field homogenization model applied in prediction of the indentation stiffness as compared to the measured one, helped in interpretation of some features of the two phases that were not accessible experimentally, like the distribution of mineral between the collagen fibrils and the extrafibrillar space. Indentation modulus of MTLT was measured using different final indentation depths, contributing to the knowledge about the indentation size effects in mineralized tissues. The measurements were performed in dried and re-hydrated state, providing insights in the elastic anisotropy of unidirectionally oriented mineralized fibers in different hydration states. Additionally, a multiscale verification of stiffness in MTLT was performed. At the macroscale, stiffness obtained with uniaxial tension tests was compared to the one predicted with a micro finite element models. The same samples were tested at the microscale, where the experimentally measured indentation modulus was compared with the one predicted with the mean field model, based on morphological parameters measured in the sites of indentation.

As the arrangement of collagen fibers in bone is complex and not fully understood, a technique allowing its assessment was adapted in this thesis to provide quantitative information on the collagen out-of-plane angle in bone sections. The technique employing circularly polarized light was calibrated on the uniaxial MTLT samples in order to provide quantitative information normalized to sample thickness and wavelength of the probing light to enable a universally applicable assessment.

This collagen arrangement assessment technique - the quantitative polarized light microscopy (qPLM) was applied to osteons of human mid-shaft femurs, along with a site-matched mineralization assessment (qBEI), nanoindentation and the mean field homogenization method of indentation modulus prediction. A weak correlation between the measured and predicted indentation moduli revealed that additional factors that contribute to the tissue stiffness, like nanoporosity, collagen cross-links or non-collagenous proteins, need to be taken into account.

Generally, in the course of this thesis new protocols and techniques helpful in assessment of the structure-function relationships were developed contributing to a better understanding of the elasticity of mineralized tissues.

Zusammenfassung

Ein detailliertes Verständnis der Morphologie und Mikromechanik von Knochen ist wichtig bei der Vorhersage und Behandlung von Knochen- Stoffwechselkrankheiten, wie Osteoporose - eine Krankheit, die hohe Morbidität und Mortalität bei der älteren Bevölkerung hervorruft. In dieser Arbeit werden umfassende experimentelle und theoretische Anstrengungen unternommen, um ein besseres Verständnis der Struktur-Funktions-Beziehungen von mineralisierten Sehnen und lamellare Knochen zu erreichen.

Mineralisierte Truthahnbeinsehne (MTLT) wurde in der Studie als mechanisches Ersatzmodell für mineralisierte Kollagenfasern von Knochen verwendet. Quantitative Rückstreuungs-Elektronenmikroskopie (qBEI) und Lichtmikroskopieaufnahmen ergaben zwei Morphologiezonen in diesem Gewebe. Die Zonen unterschieden sich hinsichtlich der Mineralisierung, des Anteils der organischen Phase, der Größe der mineralisierten Fasern und der Mikroporosität. Ein mikromechanisches Modell wurde zur Vorhersage der Indentationssteifigkeit eingesetzt, welche mit der Gemessenen verglichen werden konnte. Dieser Vergleich erlaubte eine indirekte Bestimmung der Verteilung des Minerals zwischen den Kollagenfibrillen und der extra-fibrilären Matrix. Der Einfluss der Indentationstiefe auf die gemessene Indentationsteifigkeit wurde mit MTLT-Gewebe untersucht und für mineralisiertes Gewebe verallgemeinert. Die Messungen wurden in getrocknetem und rehydriertem Zustand durchgeführt. Einblicke in die elastische Anisotropie der unidirektional orientierten mineralisierten Fasern in unterschiedlichen Umgebungsbedingungen wurden gewonnen. Zusätzlich wurde eine Untersuchung der Multiskalensteifigkeit durchgeführt. Auf der Makroebene wurde die Steifigkeit mit einem einachsigen Zugversuch gemessen und mit den Ergebnissen eines passenden Mikro-Finite-Elemente-Modells verglichen. Die gleichen Proben wurden auch auf der Mikroskala getestet. Der experimentell ermittelte Indentationsmodul wured mit einem, mittels eines Modells errechneten, Indentationsmodul verglichen. Die numerische Vorhersage basierte auf morphologischen Parametern, die exakt an den Indentationstellen ermittelt wurden.

Da die Anordnung der Kollagenfasern in Knochen komplex und noch nicht vollständig verstanden ist, wurde eine Technik entwickelt um die durchschnittliche Kollagenanordnung quantitativ zu erfassen. Die Technik verwen-

det zirkular polarisiertes Licht und wurde auf den unidirektionalen MTLT Proben kalibriert. So konnten quantitative Daten, normiert auf Probendicke und Wellenlänge des Lichts, gewonnen werden.

Diese Methode zur Messung der Kollagenanordnung - die quantitative Polarisationsmikroskopie (qPLM) - wurde auf Osteonen aus dem menschlichen Femurschaft angewandt, zusammen mit einer Messung der Mineralisierung (qBEI) und des Indentationsmoduls an exakt uebereinstimmenden Messorten. Mit Hilfe der qPLM und qBEI Daten wurde mit dem mikromechanischen Modell ein numerischer Indentatonsmodul errechnet und mit dem Gemessenen verglichen. Eine schwache Korrelation zwischen dem gemessenen und vorhergesagten Modul zeigte, dass zusätzliche Faktoren, welche die Gewebesteifigkeit beinflussen, wie Nanoporosität, Kollagenvernetzung oder nicht-kollagene Proteine, berücksichtigt werden müssten.

Im Allgemeinen werden im Rahmen dieser Arbeit neue, hilfreiche Protokolle und Techniken zur Beurteilung der Struktur-Funktions-Beziehungen in Knochen entwickelt, um so ein besseres Verständnis der Elastizität von mineralisierten Geweben zu erreichen.

Contents

Acknowledgments **I**

Abstract **II**

Zusammenfassung **IV**

1 Introduction **2**
1.1 Motivation 2
1.2 Structure-function relationships in mineralized tissues 3
1.2.1 Morphology 3
1.2.2 Micromechanics 6
1.3 Methodology 8
1.3.1 Nano- and microindentation 8
1.3.2 Quantification of the mineral content 11
1.3.3 Quantification of the organic matrix arrangement . . . 13
1.3.4 Modeling of mineralized tissues 16
1.4 Objectives of the thesis 19
1.5 Outline 20

2 Morphology of MTLT **22**
2.1 Abstract 22
2.2 Introduction 22
2.3 Materials and Methods 24
2.3.1 Samples preparation 24
2.3.2 Estimation of mineral and collagen volume fractions . 25
2.3.3 Fiber array model 29
2.3.4 Microindentation 30
2.4 Results 30
2.5 Discussion 36
2.6 Acknowledgements 40

3 Quantitative polarized light microscopy **41**
3.1 Abstract 41
3.2 Introduction 42

3.3 Methods . . . 44
3.3.1 Samples . . . 44
3.3.2 Birefringence measurements . . . 45
3.4 Results . . . 47
3.5 Discussion . . . 48
3.6 Acknowledgments . . . 50
3.7 Appendix: Derivation of the calibration formula . . . 50

4 Indentation **52**
4.1 Abstract . . . 52
4.2 Introduction . . . 53
4.3 Materials and Methods . . . 55
4.3.1 Samples . . . 55
4.3.2 Morphological analyzes . . . 55
4.3.3 Indentation . . . 56
4.4 Results . . . 58
4.4.1 Microindentation in dried and physiological conditions 58
4.4.2 Nanoindentation in dried conditions . . . 61
4.4.3 Comparison between nano- and microindentation results 61
4.5 Discussion . . . 63
4.6 Acknowledgments . . . 65

5 Homogenization **66**
5.1 Abstract . . . 66
5.2 Introduction . . . 67
5.3 Materials and Methods . . . 67
5.3.1 Design of the study . . . 67
5.3.2 Samples . . . 69
5.3.3 Geometry, mineral and collagen content determination 69
5.3.4 Evaluation of elastic properties of the tissue at microlevel 70
5.3.5 Evaluation of elastic properties of the structures at macrolevel . . . 72
5.4 Results . . . 73
5.4.1 Validation at microscale . . . 73
5.4.2 Validation at macroscale . . . 75
5.5 Discussion . . . 76
5.6 Acknowledgments . . . 78

6 Lamellar bone **79**
6.1 Abstract . . . 79
6.2 Introduction . . . 80
6.3 Materials and Methods . . . 81
6.3.1 Sample Preparation . . . 81
6.3.2 Quantitative backscattered electron imaging (qBEI) . 81

6.3.3 Quantitative polarized light microscopy (qPLM) . . . 83
6.3.4 Nanoindentation . . . 83
6.3.5 Site-matched assessment of E_{ind}, ${}^{\mathrm{mi,fa}}\varphi$ and θ . . . 85
6.3.6 The modeled indentation modulus $\tilde{E}_{\mathrm{ind}}$ . . . 85
6.3.7 Statistics . . . 88
6.4 Results . . . 88
6.4.1 qBEI results . . . 88
6.4.2 qPLM results . . . 88
6.4.3 Indentation and model results . . . 88
6.4.4 Correlation . . . 89
6.4.5 ANOVA results . . . 91
6.5 Discussion . . . 92
6.6 Conclusion . . . 96
6.7 Acknowledgments . . . 96

7 Conclusions **97**
7.1 Summary of original contributions . . . 97
7.2 General discussion . . . 99
7.3 Outlook . . . 103

List of Figures **110**

List of Tables **112**

Bibliography **127**

Curriculum Vitae **128**

Chapter 1

Introduction

1.1 Motivation

In the aging populations of industrialized countries, bone metabolic diseases represent significant health care costs. Diseases such as osteoporosis cause high morbidity and mortality among the elderly population.

In a report presented recently on the burden of the osteoporosis in the European Union (Stroem et al., 2011) it was stated that the economic burden of this disease has increased in the last decade. The related health care costs in 2010 were estimated for 30.7 billion Euro, which corresponds to 3.5% of the total health care costs. In Europe's five largest countries and Sweden, the death rate attributed to fragility fractures was as high as eighty people per day.

Better understanding of fragility fractures could have a considerable impact on improving treatments and prediction of the diseases.

The mechanics of bone is well understood at the macrolevel. Large number of experimental and numerical approaches have been applied to understand bone in terms of its global composition (mainly fraction of the mineral) and geometry. Less is known about the underlying micromechanics that result is such an exceptional performance of healthy bone at the macroscale.

In this thesis, a multiscale experimental and computational approach was employed in order to understand the micromechanics of mineralized collagen fibers present in bone. As the organization of these fibers in bone is complex and not fully understood, a simpler tissue - mineralized turkey leg tendon - was used as a model of mineralized collagen fibers.

1.2 Structure-function relationships in mineralized tissues

1.2.1 Morphology

Bone

Bone is an organ that belongs to the connective tissues family and its main function is providing the stiffness for the action of muscles, protection of the vital organs, but also homeostasis of calcium and phosphorus, as well as hematopoiesis. Bone tissue possesses a complex hierarchical structure, as shown in Fig. 1.1.

Looking at it on the nanoscale, bone comprises a network of collagenous molecules interpenetrated by a calcium phosphate phase. About 90% of the organic matrix of bone consists of collagen (Knott and Bailey, 1998). Collagen molecules are deposited in the extracellular space by the osteoblasts and later assemble into fibrils (Fratzl and Weinkamer, 2007). A specific packing of the tripe-helical, about 300nm long collagen molecules in the fibrils is characterized by a staggered arrangement along the axial direction by approximately 67 nm, that creates a characteristic "gap-overlap" pattern as suggested by Hodge and Petruska (Hodge and Petruska, 1963; Landis et al., 1996). The pattern is visible in transmission electron microscopy images as a banded structure. A newer model of the fibril arrangement was proposed by Burger et al. (2008) that suggests lateral packing of mineral crystals in collagen fibrils as an irregular stacks of platelet-shaped crystals, intercalated with layers of collagen molecules. The structure is connected with collagen cross-links - strong, stable chemical bonds that likely control the space available within the collagen fibrils, and may limit the number of mineral crystals that can be accommodated in the intrafibrillar space. The packing of collagen molecules within a fibril appears therefore to be a critical factor determining bone calcification (Glimcher, 2006).

The mineral phase of bone consists of calcium phosphate phase, often referred to as non-stoichiometric hydroxyapatite. The content of calcium in bone mineral is lower that the one in a synthetic, highly crystallized hydroxyapatites, which is reflected in its properties (Glimcher, 2006). The calcium is partially replaced with sodium ions and the phase contains significant amounts of carbonate and hydrogen phosphate groups (LeGeros et al., 1969; Glimcher, 2006). At this scale, bone mineral forms plate-like nanocrystals with thickness of 1.5 - 4.5 nm as measured using transmission electron microscopy and small-angle X-ray scattering (Fratzl and Weinkamer, 2007; Fratzl et al., 2004; Rubin et al., 2004). The mineral platelets placed within collagen fibrils seem to be arranged mostly parallel to each other and along the fibrils long axis. A certain fraction of mineral may be placed in the extrafibrillar space. The fraction of mineral deposited within the fibrils (de-

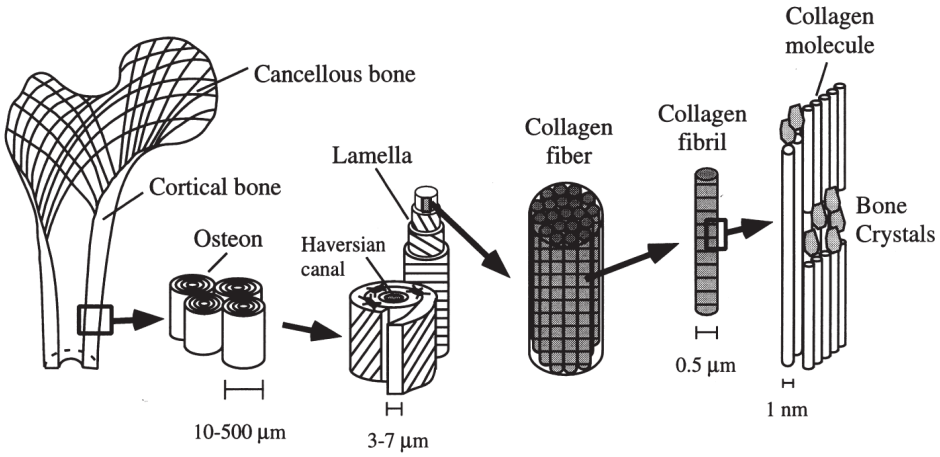

Figure 1.1: An overview of the hierarchical structure of bone. Image modified from Rho et al. (1998).

noted as mineral distribution parameter α, Reisinger et al. (2010)) is considerably discussed in the literature, as discussed in Chapter 2. The degree of mineralization in bone was studied using quantitative electron backscattered imaging (Roschger et al., 1998) or microradiography (Boivin, 1984). Additionally, Raman and Fourier transform infrared (FTIR) spectroscopies were used for compositional investigations (Boskey and Pleshko Camacho, 2007; Gamsjaeger et al., 2010; Paschalis et al., 2011; Camacho et al., 1999).

Additional minor constituents of bone are proteoglycans (decorin, osteoglycan, fibromodulin), glycosaminoglycans - GAGs (hyaluronan), glycoproteins (osteonectin, osteopontin, sialoproteins) and others. Not all roles of those constituents are clearly understood, but they are thought to play a role in the remodeling of bone, the mineralization process, as well as, in the fibrils assembly.

The mineralized collagen fibrils are assembled into fibril arrays (or fibers), which in turn form planar structures - lamellae - a complex arrangement of the fibers. A few models of the possible arrangement of the collagen fibers within lamellar planes were proposed. Most of the models assume uniaxial arrangement of the fibers within one sublamella and a certain rotation angle of the collagen arrangement between the consecutive sublamellae (Gebhardt, 1906; Ascenzi and Bonucci, 1967, 1968; Weiner et al., 1999; Wagermaier et al., 2006). Details of the models are described in Chapter 3. No final agreement on that issue was reached so far and as the arrangement of the fibers is of possible influence on mechanical properties of the composite - bone, one of the objectives of this study was to develop a quantitative method of collagen arrangement evaluation.

Next level of hierarchy is represented by bone structural units: osteons

(in dense cortex or compact bone) and trabecular packets (in the porous, sponge-like trabecular bone). Osteons are cylindrical structures built up by lamellae, that are arranged around blood vessels (Haversian channels). The wall thickness of these structures is about 40-60 μm and they are a result of the bone turnover - a coordinated action of the bone resorbing cells - osteoclasts and bone forming calls - osteoblasts. Different types of lamellae morphotypes were presented in in the literature. A common assumption is differentiating three types: transverse, longitudinal and alternating lamellae(Ascenzi et al., 2003). The types are characterized by the average collagen arrangement, with the longitudinal lamellae with fibers mainly arranged in parallel to the osteon axis, transverse ones with the fibers arranged in a circumferential manner around the Haversian channel and the alternating lamellae with fibers arranged at average in 45^o to the osteons axis.

As the arrangement of collagen fibers in lamellar bone is not clearly resolved and likely very complex, in this study a tissue with simply, uniaxial arranged mineralized collagen fibers was used.

Mineralized tendon

Mineralized turkey leg tendon (MTLT) is a tissue generally similar in composition to bone, consisting mainly of mineral, collagen and water. 90-95% of the organic matrix consists of collagen type I, with the rest of collagen type V and XII, as well as, proteins including osteopontin, sialoproteins, osteocalcin and proteoglycans (Glimcher et al., 1979; Landis, 1986). The non-mineralized and mineralized parts of turkey leg tendons show different distribution of proteoglycans. In the non-mineralized sites the proteoglycans can be found throughout the fibers, while in the mineralized parts only between the fibers (Liu and Kuboki, 1996).

The tendons of the avians mineralize naturally over time, starting at 10-14 weeks of animal age (Landis et al., 1996; Landis and Silver, 2002), which makes them attractive models for studying the mineralization process. MTLT could be also used as a model to study mechanical properties of mineralized fibers (for details see Chapter 2).

Different tendons extracted from wild or domestic turkeys (Prostak and Lees, 1996; Knott et al., 1997; Lees et al., 1994; Landis et al., 1996; Silver et al., 2001, 2000; Traub et al., 1989; Landis and Silver, 2002; Siperko and Landis, 2001; Kohler et al., 1995; Arsenault, 1988) were used. Most frequently the digital tendons (Bigi et al., 1996; Gupta et al., 2004) or Achilles gastrocnemius tendons (Landis et al., 1996; Silver et al., 2001, 2000) were used. In this study digital tendons of domestic turkeys were used and extracted as schematically shown in Fig. 1.2.

The mineralization patterns in MTLT is likely to be different than the ones in bone, as the already existing collagenous matrix is mineralizing over time, unlike in bone where the mineralization begins faster after the col-

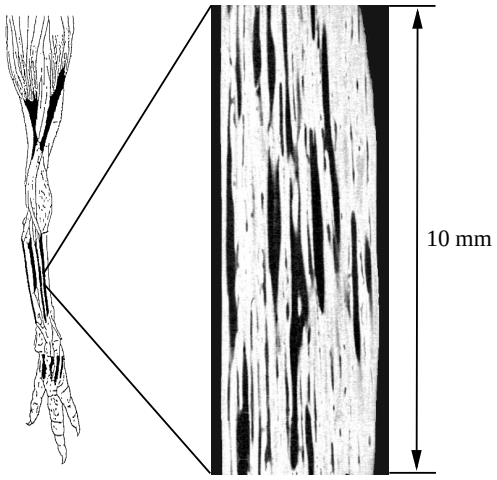

Figure 1.2: A scheme of extraction of the digital tendons from domestic turkey's legs.

lagenous network is laid down. The cells of tendons called tenocytes or tendonoblasts (Landis and Silver, 2002) remain viable in lacunae surrounded by mineral, which is similar to osteocytes in the mineralized matrix of bone (Landis and Silver, 2002). The mineralization process can occur in two locations simultaneously: within collagen fibrils, resulting in highly organized mineralization patterns, and in the extrafibrillar space, resulting in randomly dispersed mineral crystals in radially shaped clusters (Landis, 1986; Arsenault, 1988).

1.2.2 Micromechanics

One of the main interest of the study was to assess the contribution of the hierarchical structure described above on elastic properties of the mineralized tissues. Mechanics of whole bones were studied widely over last decades and are reasonably well understood, but the underlying micro- and nanomechanics are still not fully resolved. Some investigations at lower length scales involved bending, tensile or torsion tests of compact and trabecular bone specimens. High importance of the vascular and lacuno-canalicular porosity was noted in bending tests of compact and trabecular bone microspecimens (Liu et al., 1999). Scanning acoustic microscopy studies shower that microporosity was the main factor determining elasticity in human cortex (Granke et al., 2011). Microscale tensile tests were also performed on bone specimens (Rho et al., 1993; Bini et al., 2002). On the lower length scale, mechanical properties of single osteons were measured (Ascenzi et al., 1994). Numerical compression experiments on single osteons of different morphotypes were performed recently, giving insights of the possible explanation of the distri-

bution of the osteons type in lamellar bone (De Micheli and Witzel, 2011). Shear strength of the interfaces between single osteons was tested in microscale push out tests performed on different osteon morphotypes (Bigley et al., 2006).

Recently nano- and microindentation is becoming more and more used in accessing elastic properties of mineralized tissues at nano- and microlevels (Hengsberger et al., 2002b; Oyen, 2006; Ebenstein and Pruitt, 2006; Franzoso and Zysset, 2009; Wolfram et al., 2010a; Zhang et al., 2010; Reisinger et al., 2011). This technique involves local material deformation under controlled force applied with a stiff diamond tip, which allows for high resolution of the stiffness assessment needed for testing of heterogeneous materials. Single osteons were tested with this technique and the degree of elastic anisotropy was quantified (Rho et al., 2001; Franzoso and Zysset, 2009; Reisinger et al., 2011). Some approaches have been made in order to be able to test bone specimens in physiological conditions, as the sample hydration level is reflected in the measured stiffness.

A study employing synchrotron diffraction (small angle X-ray scattering, SAXS) for evaluating the sub-micrometer deformation mechanisms in mineralized tendons was performed by Gupta et al. (2004). Strains in MTLT tissue were measured as the changes in axial periodicity of collagen molecules with applied loads. Splitting of peaks in the diffraction spectra was attributed to the inhomogeneous fibril deformation, with a part that is relaxed to the unstressed length and a part that reminds stretched. The behavior was attributed to the mineralized and non-mineralized parts of MTLT in the tendons of 24 weeks old turkeys. The degree of inhomogeneity in the fibril deformation was decreasing with animal age (so also the extent of mineralization).

1.3 Methodology

1.3.1 Nano- and microindentation

As described above, a few techniques have been employed for evaluation of elastic properties of mineralized tissues at the microscale. For this project, nano- and microindentation were chosen as the techniques validated for the use on mineralized tissues (Hengsberger et al., 2002b; Oyen, 2006; Ebenstein and Pruitt, 2006; Donnelly et al., 2006; Lewis and Nyman, 2008; Franzoso and Zysset, 2009; Wolfram et al., 2010a; Zhang et al., 2010; Reisinger et al., 2011; Zysset et al., 1999; Zysset, 2009). The aim of this work was performing a site-matched combination of techniques allowing for measurement of morphological (mineralization and collagen fibers arrangement) and mechanical data. In this context, an additional advantage of using indentation was the fact that the required sample preparation was compatible with requirements of the other techniques used in the study (see Sections 6.3.2 and 6.3.3).

Indentation is a technique using contact mechanical testing (Oyen, 2011; Fischer-Cripps, 2002), which measures local properties, therefore it has found many applications in testing of inhomogeneous composite materials, including mineralized tissues.

The technique is based on pressing a stiff probe (indenter, most often made of diamond) with known shape onto a plane surface of a tested material. During indentation, the load and the displacement are monitored and the process can be controlled with load or displacement.

The indenter shape used most frequently for mineralized tissues is the three- sided pyramid Berkovich indenter (shown schematically in Fig. 4.2). An imprint made with such a tip in mineralized tendon sample is shown in Fig. 1.3. For softer tissues, a spherical indenters are often used in order to minimize the stress concentration, minimize the plastic deformation and damage accumulation (Ebenstein and Pruitt, 2006). A mechanism of deconvolution of elastic modulus and hardness of an elastic-plastic material was published by Oliver and Pharr (1992). It became very popular and nowadays is incorporated in many commercial indentation software (eg. TriboScan, Hysitron, USA or CSM Instruments Indentation software, Peseux, Switzerland) and widely used. The so called Oliver and Pharr method assumes that the unloading part of the indentation curve is purely elastic. The reduced modulus of the contact E_r can be related to the unloading stiffness S via:

$$E_r = \frac{\sqrt{\pi}}{2}\frac{S}{\sqrt{A}} \tag{1.1}$$

The probe-sample contact area is defined with a calibration function $A(h_c)$, where h_c is the contact depth. Contact area $A(h_c)$ is calibrated on a reference material with a fixed E_r (most commonly fused silica) solving Equation 1.1 for a range of contact depths h_c, in order to account for the non-perfect

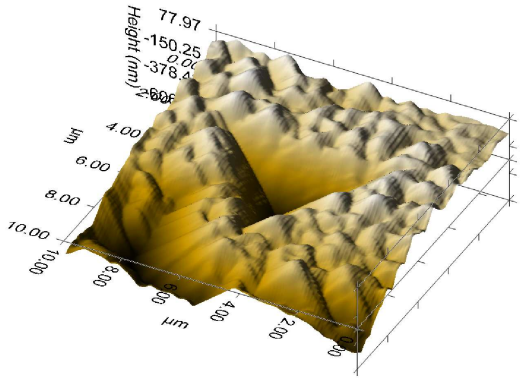

Figure 1.3: An indentation imprint of a Berkovich indenter in axial direction of MTLT sample imaged with the indentation tip used in scanning probe microscopy mode of the TriboIndenter, Hysitron, USA.

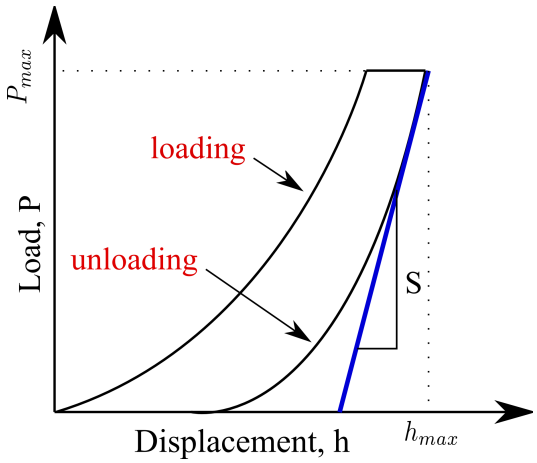

Figure 1.4: An exemplary indentation curve involving a loading, holding and unloading phases.

shape of the probe. The contact depth is defined as:

$$h_c = h_{\max} - 0.75\frac{\mathrm{P}_{\max}}{S} \ , \tag{1.2}$$

where $\mathrm{P}_{\max}$ is the maximal load and $h_{\max}$ the maximal displacement. In the Oliver and Pharr method the three parameters: $\mathrm{P}_{\max}$, $h_{\max}$ and the S are directly obtained from the loading-unloading indentation curve (as shown in Fig. 1.4). For isotropic materials the reduced modulus is directly related to the Poisson's ratio of a sample ν and the indenter ν_{tip}, as well as, the

Young's modulus of the indenter E_{tip}:

$$\frac{1}{E_r} = \frac{1-\nu^2}{E} + \frac{1-\nu_{tip}^2}{E_{tip}} \,, \tag{1.3}$$

where the indentation modulus of an isotropic material is related to its Young's modulus only with the Poisson's ratio:

$$^{ind}E = \frac{E}{1-\nu^2} \tag{1.4}$$

For anisotropic materials (as for example bone or mineralized tendon), the interpretation of the indentation data is more complex, but the following equation was developed by Swadener and Pharr (2001) to relate the indentation modulus with the stiffness tensor $\mathbb{S}$ and the direction of the indentation $\mathbf{a}_3$:

$$^{ind}E(\mathbb{S}, \mathbf{a}_3) = \frac{4\pi}{\displaystyle\int_0^{2\pi} \frac{\mathbf{B}^{-1}(\mathbf{t}(\gamma), \mathbb{S}) : [\mathbf{a}_3 \otimes \mathbf{a}_3]}{\sqrt{(a_1/a_2)\,\cos^2\gamma + (a_2/a_1)\,\sin^2\gamma}}\,\mathrm{d}\gamma}, \tag{1.5}$$

where $\mathbf{B}(\mathbf{t}(\gamma), \mathbb{S})$ is the second order Barnett-Lothe tensor taking into account material's elastic properties. Equation 1.5 degenerates into Equation 1.4 for isotropic materials.

Recently, an inverse procedure to the one of Swadener and Pharr (2001) was proposed by Franzoso and Zysset (2009). The procedure allows iterative estimation of a stiffness tensor of an anisotropic material from indentation moduli obtained in two indentation directions, for transverse isotropic, and three, for orthotropic materials.

In the procedure described in detail in Franzoso and Zysset (2009), the micro-structural fabric-based elasticity model was used to describe the elastic anisotropy of lamellar bone using a second-order fabric tensor $\mathbf{M}$:

$$\mathbf{M} = m_i \mathbf{M}_i = m_i(\mathbf{m}_i \otimes \mathbf{m}_i) \,, \tag{1.6}$$

where m_i are the eigenvalues and $\mathbf{m}_i$ the eigenvectors of $\mathbf{M}$, (Franzoso and Zysset, 2009).

Using the fabric tensor $\mathbf{M}$, a locally orthotropic fabric-based elastic compliance tensor $\mathbb{E}(\mathbf{M})$ can be defined as (Curnier et al., 1995):

$$\mathbb{E}(\mathbf{M}) = \frac{1}{\epsilon_0}\left[\sum_{i=1}^{3}\frac{1}{m_i^2}\Big(\mathbf{M}_i \otimes \mathbf{M}_i\Big) - \sum_{\substack{i,j=1\\ i\neq j}}^{3}\frac{\nu_0}{m_i m_j}\Big(\mathbf{M}_i \otimes \mathbf{M}_j\Big) + \sum_{\substack{i,j=1\\ i\neq j}}^{3}\frac{\epsilon_0}{2\,\mu_0 m_i m_j}\Big(\mathbf{M}_i \,\underline{\overline{\otimes}}\, \mathbf{M}_j\Big)\right] \tag{1.7}$$

The following assumptions need to be made in order to estimate a compliance tensor $\mathbb{E}(\mathbf{M})$ depending on the six parameters $(\epsilon_0, \nu_0, \mu_0, m_1, m_2, m_3)$. First, the eigenvectors of the $\mathbf{M}$ are oriented along the principle material directions. Then,

$$\mathrm{tr}(\mathbf{M}) = 3 \tag{1.8}$$

provides that the constants $(\epsilon_0,\ \nu_0,\ \mu_0)$ have the physical meaning (Young's modulus, Poisson's ratio and shear modulus of a virtual isotropic material, respectively). Additionally equation:

$$\mu_0 = \frac{\epsilon_0}{2(1+\nu_0)} \tag{1.9}$$

holds and values of ν_0 and m_1 are fixed ($\nu_0 = 0.32$, $m_1 = 0.747986$), (Franzoso and Zysset, 2009).

The procedure involves normalization of the compliance tensor $\mathbb{E}(\mathbf{M})$ by setting ϵ_0 to 1 and computing the indentation moduli in two directions (axial and transverse; $\mathbf{m}_2, \mathbf{m}_3$) for a varied parameter m_2.

For a given indentation direction, the relation between the normalized (${}^{ind}E_{norm}$) and measured indentation moduli (${}^{ind}E_{exp}$) is given by:

$${}^{ind}E_{exp}(\mathbf{m}_2) = \epsilon_0 {}^{ind}E_{norm}(m_2, \mathbf{m}_2) \tag{1.10}$$

$${}^{ind}E_{exp}(\mathbf{m}_3) = \epsilon_0 {}^{ind}E_{norm}(m_2, \mathbf{m}_3) \tag{1.11}$$

From the ratio of equations 1.10 and 1.11, m_2 can be solved, which allows calculation of ϵ_0. Those two values put into the equation 1.7 allow construction of an estimated compliance tensor (Franzoso and Zysset, 2009).

1.3.2 Quantification of the mineral content

Mineral phase of bone is one of the three major components of bone, next to collagen and water, as mentioned above. It is also the stiffest of the components, with Young's modulus of 110.15 GPa (Yao et al., 2007) and is therefore often treated as the main factor determining the bone stiffness. As the overall correlations of mineral content to stiffness show only a limited success (Raum et al., 2006; Hengsberger et al., 2002a; Boivin et al., 2008; Follet et al., 2004; Zebaze et al., 2011), especially in describing local trends, some other factors as microporosity or arrangement of the organic matrix, are being investigated, as described later on.

Some techniques of quantifying the mineral content at the microlevel are available. Quantitative backscattered electron imaging (qBEI) is a state of the art technique frequently employed for quantification of mineralization of bone matrix. This technique quantifies electrons backscattered from a thin layer ($\sim 1.5\ \mu$m) of a polished sample under the beam of an electron scanning microscope, see Fig. 1.5. The grey-levels of such a backscattered electrons

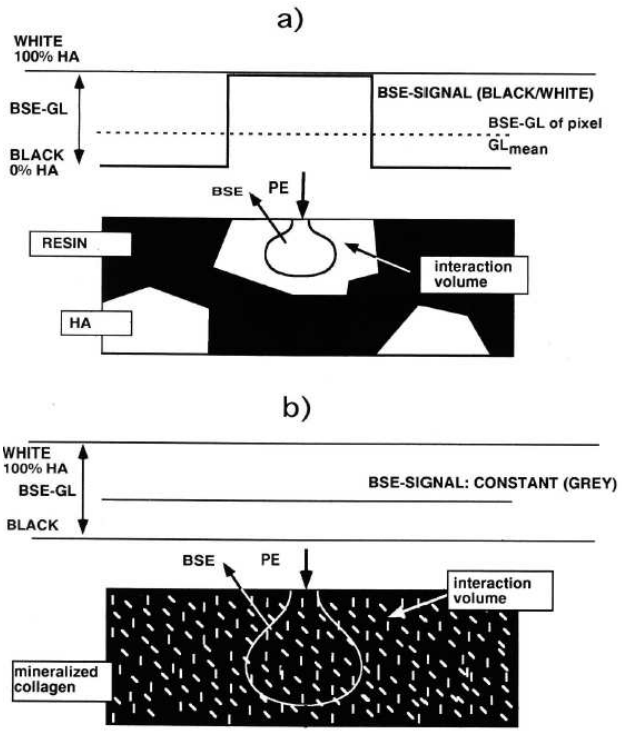

Figure 1.5: A scheme of the electron beam (PE - primary electrons) interaction with a sample surface resulting in backscattering of the electrons (BSE - backscattered secondary electrons). a) beam interaction with a standard hydroxyapatite material and the grey levels difference between the resin and mineral. b) bone tissue with a distribution of the grey values. Image from Roschger et al. (1995)

image are related to the atomic number and amount of atoms in the material scanned. As calcium possesses the highest atomic number among the bone constituents, it is dominating the response. Calcium weight fraction (weight percent) was calibrated to the grey scales observed using standard materials of aluminum and carbon (Roschger et al., 1995, 1998). These relations were used for mineral concentration evaluation on bone, see Fig. 1.6. The method proved to be successful for comparison between treated and untreated bones or bone metabolic diseases, for example by Roschger et al. (2001); Grabner et al. (2001); Valenta et al. (2005); Blouin et al. (2009); Fratzl-Zelman et al. (2010); Paschalis et al. (2011).

Here, it is important to mention that while qBEI evaluates the mass fraction of mineral phase, it is the mineral volume fraction that actually triggers the mechanical properties of mineralized tissues. In this sense, volumetric methods seem to be more suitable. Microradiography provides this type of

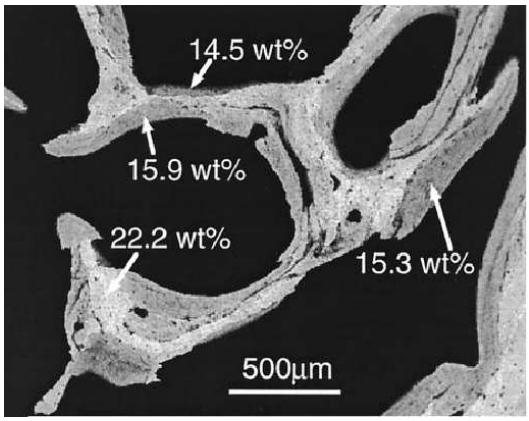

Figure 1.6: An example of calcium weight fraction evaluation on a human bone. Image adapted from Roschger et al. (1998).

information and was systematically applied to bone (Boivin, 1984), but it requires complicated sample preparation. Sample fixation involving dehydration in graded alcohols solutions and resin infiltration is recommended in order to obtain uniform thin bone sections. Such sections are not suitable for indentation and therefore this technique was not used.

1.3.3 Quantification of the organic matrix arrangement

The arrangement of collagen fibrils and fibers in bone is a matter of considerable dispute. A few models of the arrangement of the fibers in lamellar bone were proposed and are reviewed in Chapter 3. There are a few methods that were employed to quantify the collagen orientation, for example scanning small angle X-ray scattering (SAXS) and wide angle X-ray diffraction (WAXD), (Wagermaier et al., 2006). A combination of this techniques allowed obtaining quantitative information of local crystallite orientation of several osteons. Assuming that the arrangement of the crystallites is compliant with the arrangement of the collagen fibers, conclusions about the organics matrix arrangement may be drawn. This assumption appears to be a downside of this approach, as there is possibly mineral that is placed within the extrafibrillar matrix in bone (Fritsch and Hellmich, 2007; Sasaki et al., 2002) and its arrangement may be different to the intrafibrillar one. Another disadvantage is the limited volume of a sample tested.

Acoustic microscopy was another technique used for quantification of the collagen arrangement in intact, decollagenized and demineralized bone by Turner et al. (1995) by measuring the elastic anisotropy of bone, mineral and collagen, respectively. The assumption that the elastic symmetry of bone reflects its fundamental structure was used. Interestingly, the results

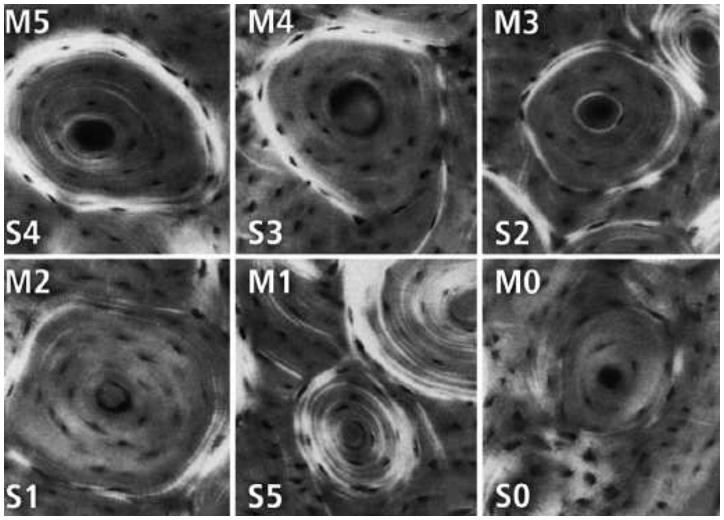

Figure 1.7: Birefringence patterns of osteons with different morphotypes. Letters in the top corners contain the original scale by Martin (Martin et al., 1996). The bottom corners contain the updated scale by Skedros et al. (2009). Image from (Skedros et al., 2009).

depicted a certain misalignment of collagen and mineral in bone. Mineral was oriented along the long axis of osteons and collagen was aligned at a angle of 30^o to the long axis. Authors have drawn a conclusion that there must be a certain amount of the extrafibrillar mineral in bone and that it is likely arranged in a different manner, as compared to the intrafibrillar one.

Polarized light techniques were used before to investigate the collagen arrangement in bone in a qualitative manner. First attempts were made by Gebhardt (1906), Ascenzi and Bonucci (1976), Martin and Ishida (1989) and Boyde and Riggs (1990), with some modifications by Martin et al. (1996), (Bromage et al., 2003) and Skedros et al. (2009). The general idea was to relate the observed birefringence of a bone sample under a circularly polarized light to the average collagen arrangement in a section. Martin et al. (1996) proposed a scale including six types of the secondary osteons, see Fig 1.7. The morphotypes were defined based on the appearance of the peripheral lamellae (the brighter outer ring) and the distribution of the "bright" lamellae throughout an osteon. The scale was later updated by Skedros et al. (2009). The information about the collagen arrangement was not quantitative in those attempts, but allowed for general characterization of the preferred fiber orientation in for example human femurs (Goldman et al., 2003) and apes femurs (Kalmey and Lovejoy, 2002) or equine metacarpal bone (Martin et al., 1996).

Bromage et al. (2003) introduced the idea of calibration of the polarized

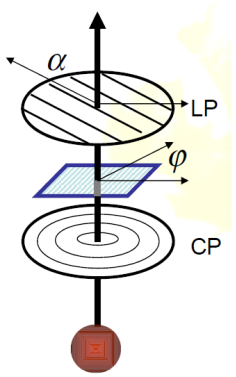

Figure 1.8: Schematic representation of the circular and linear polarizers set-up. Light source in red, CP - circular polarizer, ϕ - extinction angle, in blue - a sample, LP - linear polarizer, α - angle of the polarizer orientation.

light technique using uniaxial oriented fibers of MTLT cut at two orthogonal planes. The proposed method required a uniform sections transparency, thickness and uniformity of the illuminating system, which limited the possibility of an universal use of the method.

One of the scopes of the thesis was filling the gap in universality of the circularly polarized light technique, as well as its calibration that would provide possibilities of quantitative collagen arrangement assessment, normalized to the sample thickness and the wavelength of the probing light. Calibration and normalization procedure using MTLT is described in detail in Chapter 3.

The experimental set-up used for the calibration study was composed of the following parts (see Fig. 1.8):

- light source
- interference filter
- circular polarizer (linear polarizer + quarter wave-plate)
- sample
- image multiplexer
- CCD camera with four linear polarizers at angles α: 0^o, 45^o, 90^o and 135^o.

The intensity of light passing through this system is measured by the CCD camera and is given by:

$$I = \frac{1}{2} I_0 (1 + sin2(\alpha_i - \phi) sin\delta) \tag{1.12}$$

where: I_0 - transmission intensity, α_i - discrete polarizer angles, ϕ - extinction angle (orientation of the slow axis) and δ - phase factor. A combination of four polarizers at angles α: 0^o, 45^o, 90^o and 135^o was used to obtain quantitative information of phase factor δ (related to the birefringence, as described in detail in Chapter 3) and the extinction angle. In the calibration study presented in Chapter 3 the phase factor was measured on MTLT samples cut a variety of angles and related to the out-of-plane collagen fibers angle, sample thickness and wavelength of the probing light, resulting in an universally applicable relationship allowing quantification of the average collagen arrangement in bone sections.

1.3.4 Modeling of mineralized tissues

Micromechanical modeling

Micromechanical modeling is based on derivation of the mechanical properties of a composite from the properties of the composite's components, as well as their spatial arrangement. A few continuum mechanics (homogenization theory) models of bone at different lengthscales were proposed before (Sevostianov and Kachanov, 2000; Hellmich and Ulm, 2002). For bone, as mentioned in Section 1.2.1, the main components are mineral, collagen and water/pores. In the previous modelling attempts, the mineralized collagen matrix was treated as mineral reinforced collagen matrix (Jaeger and Fratzl, 2000) or as a mineral matrix with collagen inclusions (Hellmich and Ulm, 2002), or a combination of the both approaches at different length scales (Fritsch and Hellmich, 2007; Reisinger et al., 2010).

The Mori-Tanaka homogenization method was used in this study. The scheme was designed to model elasticity of composites with a matrix-inclusions topology (Mori and Tanaka, 1973). In the model all field quantities, such as strain and stress are described in terms of volume averages of the corresponding phases. The phases of mineralized collagen fibril array were modeled as unidirectional aligned Eshelby-type spheroidal inclusions that were randomly distributed in space and perfectly bonded to the matrix (Reisinger et al., 2010). The model predicts the stiffness tensor of a fibril array, containing mineralized collagen fibrils, mineralized extrafibrillar matrix and micropores. Input data of the model are mechanical and morphological parameters of mineralized collagen fibrils and mineralized extrafibrillar matrix, like elastic moduli of the phases, degree of mineralization, mineral distribution between the phases and others.

The model presented in Chapter 5 was adapted from Reisinger et al. (2010). At the nanoscale the mineral reinforced collagen matrix system was modeled (see Fig. 1.9 a). At the microscale, the collagen (or internally and partially mineralized collagen) inclusions in the mineral (or "mineral foam") matrix were modeled, see Fig. 1.9 b. The isotropic "mineral foam"

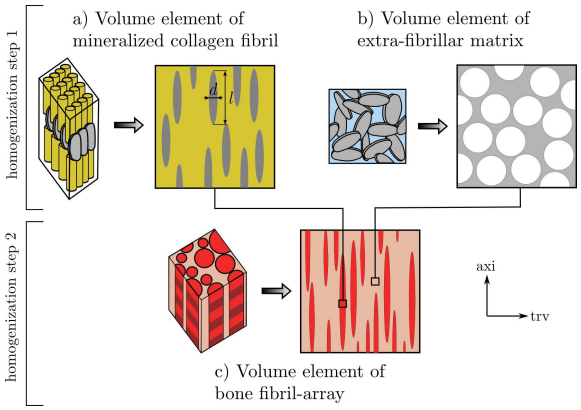

Figure 1.9: The homogenization scheme involving two levels of tissue hierarchy: first step of homogenization involves modeling of a mineralized collagen fibril and the extrafibrillar matrix. Than the two are assembled in order to model a mineralized collagen fibril array. Image from Reisinger et al. (2010).

may seem counterintuitive, as a certain anisotropy of mineral platelets is known, but as this is the extrafibrillar mineral, a random arrangement of the platelets is likely, as suggested for example by Turner et al. (1995).

A uniaxial arrangement of the mineralized collagen fibrills in the extrafibrillar mineral matrix was modeled in order to help understanding the elasticity of the transverse isotropic structure of MTLT. The stiffness tensor predicted with this model at microscale was used in assigning elastic properties of finite element models of MTLT at macroscale.

Finite element method

The finite element (FE) method consists in dividing a sample in simple geometric elements connected by a finite number of nodes. The material properties of an element are described by constitutive laws. The local formulations are assembled to a global equation characterizing the whole sample (Varga, 2010). Following the equilibrium principle and knowing the stress-strain relationships for the elements, after applying a specific load case on the sample, the global displacements can be calculated.

The FE was first applied in orthopedics in 1972, as reported by Huiskes and Chao (1983). Since then it was more and more successfully employed in modeling of prostheses, but also in investigation of the fundamental laws governing the musculoskeletal structures. The method was widely used for trabecular bone (Van Rietbergen et al., 1996; Kabel et al., 1999; Bayraktar and Keaveny, 2004). Different anatomical sites were investigated with this method including vertebral bodies (Chevalier et al., 2007; Wolfram et al., 2010b; Dall'Ara et al., 2010a), distal radius (Varga and Zysset, 2009; Varga

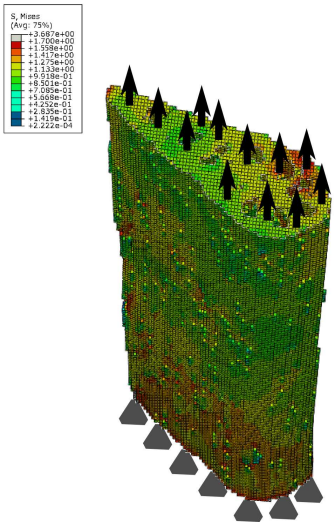

Figure 1.10: An example of von Mises stresses distribution in a sample of MTLT tested in tension.

et al., 2009, 2010; Pistoia et al., 2002) and femur (Verhulp et al., 2006; Keyak et al., 1993; Keyak, 2000, 2001; Orwoll et al., 2009).

In this work the μFE method was employed. At the mesoscale, which for the mineralized turkey leg tendon means the scale of a tendon, the method was used to model the stiffness of the tendons in uniaxial tension tests. This method involves high resolution μCT (micro computed tomography) scans that can be converted to finite element meshes directly. The loading case for this simulations was based on the experimental setup used for uniaxial tension tests of the MTLT samples in the elastic region (as described in Chapter 5). Elastic properties of the elements were assigned using information from the microlevel experiments on one hand (two-directional indentation), and micromechanical modeling, on the other.

1.4 Objectives of the thesis

The global objective of the thesis was a multi-scale, site-matched combination of the degree of mineralization, collagen arrangement and stiffness in mineralized tendon and lamellar bone. The hypothesis was that stiffness of mineralized tendon and lamellar bone can be predicted with morphological parameters like arrangement of the phases and their volume fractions.

In the course of this thesis, experimental protocols for checking the hypothesis were developed and validated with modeling approaches. The investigation of the influence of the morphological parameters on the resulting stiffness at micro- and macrolevels was performed.

Specific goals

- Improving the morphological investigation methods of mineralized tissues by bringing the polarized light microscopy technique, formerly used in a non-quantitative way, to an applicable quantitative stage. This technique, after calibration on uniaxial mineralized turkey leg tendons, could be systematically applied in investigations of collagen arrangement in bone sections. Information gained with this technique could improve the general understanding of the fiber arrangement in bone and improve the modeling possibilities of mineralized tissues.

- Validation of an experimental scheme comprising measurements of morphology of the phases and their arrangement, using modeling approaches at different scales of the mineralized tendon and application of the scheme to lamellar bone.

- Quantification of the degree of elastic anisotropy in MTLT. This uniaxial tissue is assumed to have the highest degree of anisotropy among the mineralized tissues, but this hypothesis was not tested experimentally.

1.5 Outline

Introduction

Provides an overview of the morphology of mineralized tendon and bone and their micromechanics. State of the art investigation methods of the structure-function relationships in these tissues are briefly reviewed. The techniques chosen for the investigation in the course of this thesis are described in Chapter 1.

Investigation of the morphology of mineralized turkey leg tendons (MTLT)

Chapter 2 describes the morphology of mineralized turkey leg tendons (MTLT) as seen by (polarized) light microscopy and quantitative backscattered electron microscopy (qBEI). The tendons from domestic turkeys investigated in the course of this thesis showed two zones of morphology not described in the literature before. Additional goal of the study was to understand the differences between the zones in terms of their morphology and elasticity. Mean field homogenization model was instrumental for interpreting the differences between the zones, in the lack of direct experimental evidence at nanoscale.

Calibration of the quantitative polarized light (qPLM) technique

Chapter 3 describes the procedure leading to calibration of a polarized light technique using MTLT sections for quantitative universal assessment of the average collagen out-of-plane angles, as well as its application in quantifying the collagen arrangements in human osteons.

Two directional nano- and microindentation of mineralized turkey leg tendons

In Chapter 4 the elastic anisotropy of MTLT was assessed experimentally. Two-directional indentations were performed in dried and re-hydrated conditions, in order to evaluate sample's re-hydration effects on the tissue stiffness. Indentation depth effect - increase of measured indentation modulus with decreasing sampling volume was tested using two different final indentation depths.

Experimental validation of the fiber array model of MTLT at two levels of hierarchy is presented in Chapter 5

The experimental procedure used in this part of work involved microindentation, macroscopic tensile testing, as well as, quantitative backscattered electron imaging (qBEI), ashing, demineralization and μCT scanning of the

MTLT samples. The computational part involved micromechanical homogenization models and μFE simulations.

A site-matched assessment of mineralization, collagen fibers arrangement, measured and predicted indentation stiffness in lamellar bone

The Chapter 6 combines all the methodologies used and/or validated in previous chapters, employed to better understand structure-function relations in human secondary osteons.

Conclusions

Summary of the original contributions, as well as, the general discussion about the outcome of this study along with the main conclusions is given in Chapter 7.

Chapter 2

Morphology of MTLT

This chapter describes the morphology of mineralized turkey leg tendons (MTLT) as seen by (polarized) light microscopy and quantitative backscattered electron microscopy (qBEI).
Based on manuscript:
"Influence of mineralization and microporosity on tissue elasticity. Experimental and numerical investigation on mineralized turkey leg tendons."
By Ewa M. Spiesz, Paul Roschger and Philippe K. Zysset
Accepted for publication in Calcified Tissue International, 2011.

2.1 Abstract

A combined experimental and numerical study correlating indentation stiffness with mineralization and microporosity was performed on mineralized turkey leg tendon (MTLT). Two distinct tissue morphologies were distinguished by quantitative backscattered electron imaging (qBEI) and called circumferential and interstitial zones. These two zones showed different tissue organization, microporosity and mineralization. The stiffness measured with microindentation was also different in the two zones. Mean field method of modeling of mineralized collagen fibers was employed as an attempt to explain the differences.

2.2 Introduction

The structure of the mineralized turkey leg tendon is approximately transverse isotropic, with fibers aligned to the long axis of the tendon Lees et al. (1994), which makes it an attractive model to study mechanical properties of mineralized collagen fibers. The tendons of avians normally mineralize over time, which additionally makes them attractive models to study the mechanisms of mineralization Landis et al. (1996); Landis and Silver (2002). The tendons undergo a gradual mineralization from a point mid-way along

the tendon in the proximal direction, giving possibilities to study different stages of the process, depending on the distance from the mineralization front. The cells of the tendon (called tenocytes or tendonoblasts) can be found in columnar arrangements along the collagen fibers Landis and Silver (2002). Constituents of MTLT are mainly collagen (90% collagen type I), hydroxyapatite and water. Mineral content of tendons of 24 weeks old domestic turkeys was reported to be slightly lower than this of human bone Gupta et al. (2004). The morphology of the MTLT of 12-24 weeks old animals, as seen on quantitative backscattered electron images (qBEI) shows discrete unmineralized and mineralized collagen fiber bundles Gupta et al. (2004).

Even though the topographic relation of mineral to collagen fibers in mineralized tissues was studied for many years, it is still a matter of considerable dispute Fratzl (2008). The two possible locations of hydroxyapatite are inside the collagen fibrils or between them. The mineral distribution parameter α defines what fraction of the mineral is placed within the fibrils Reisinger et al. (2010). There are different views on where the majority of the mineral is placed. Weiner et al. Weiner et al. (1999) and Gao et al. Gao et al. (2003) suggest that most of the mineral is placed within the collagen fibrils, while Fritsch and Hellmich Fritsch and Hellmich (2007) state that the mineral is mostly extrafibrillar. Sasaki et al. Sasaki et al. (2002) using atomic force microscopic studies estimated that 77% of the mineral in bovine femoral cortex is placed outside of the collagen fibrils. Similar attempt combined with electron microscopy performed by Lees et al. Lees et al. (1994) resulted in 70-75% of mineral seen in the extrafibrillar space in mineralized leg tendon of domestic turkey. It was shown that the extrafibrillar mineralization of the collagen fibrils enhances their mechanical properties, when the crystals adhere strongly to the fibrils Nikolov and Raabe (2008). The influence of mineral distribution on the stiffness was not addressed experimentally.

Indentation, next to scanning acoustic microscopy Raum et al. (2005); Preininger et al. (2011) is a widely-used technique used for accessing the elastic properties of inhomogeneous materials at the micro- and nanolevel. In this technique indentation modulus can be evaluated based on elastic contact theory Oliver and Pharr (1992); Fischer-Cripps (2002), for rate-independent, elasto-plastic materials. For isotropic materials, the indentation modulus is directly related to elastic modulus and Poisson's ratio. For anisotropic materials, like bone and MTLT, indentation modulus is related to the stiffness tensor with more complex function, but can be evaluated using iterative schemes Franzoso and Zysset (2009).

A Mori-Tanaka mean field method that estimates homogenized linear anisotropic elastic properties of composites, consisting of an inclusion-matrix topology was used Mori and Tanaka (1973). This type of model with two hierarchical levels of homogenization was recently proposed to model min-

eralized collagen fibrils Reisinger et al. (2010). In the model all field quantities, such as strain and stress, are described in terms of volume averages of the corresponding phases. Unidirectionally aligned Eshelby-type spheroidal inclusions are randomly distributed in space and perfectly bonded to the matrix Reisinger et al. (2010). The model predicts the stiffness tensor of a fibril array, containing mineralized collagen fibrils and mineralized extrafibrillar matrix. Input data of the model are mechanical and morphological parameters of mineralized collagen fibrils and mineralized extrafibrillar matrix, like elastic moduli of the phases, degree of mineralization, mineral distribution between the phases and others. This model was used here to obtain stiffness tensors of unidirectional mineralized fibers present in MTLT.

The goal of this work was to correlate the stiffness of MTLT, assessed experimentally with microindentation and numerically with mean field modeling, with the morphological parameters, mainly amount of mineral and its distribution between the collagen fibrils and extrafibrillar matrix, as well as microporosity of the tissue. In the course of the study, two zones of distinct morphology of MTLT - circumferential and interstitial - were observed and described.

2.3 Materials and Methods

2.3.1 Samples preparation

Mineralized parts of digital flexor tendons of domestic turkeys Knott et al. (1997); Lees et al. (1994); Landis et al. (1996); Silver et al. (2001, 2000); Traub et al. (1989); Landis and Silver (2002); Siperko and Landis (2001); Kohler et al. (1995); Arsenault (1988) older than 24 weeks were used in this study. Ten tendons were harvested from eight legs obtained from a local market. The soft nonmineralized tendon material was present on both ends of the stiff rod shaped tendons, making sure that the insertion sites were not included in the specimens. The tendons were kept frozen at -20 $^{\circ}C$ until preparation.

Four methods of samples preparation were used in this study:

1. Samples for quantitative backscattered electron imaging (qBEI, Fig. 2.3) and microindentation:
   Ten $\sim$10 mm long specimens (about 40-60% of the hard mineralized tendon length), taken from 8 legs, were divided in four parallel samples each. A total of 39 (one section was destroyed during preparation) fresh, undecalcified, non-dehydrated tendon cross-sections were embedded in epoxy resin (EpoFix, Struers, Ballerup, Denmark), cut into thin (approximately 1mm) slices, mounted on glass slides and polished using silicon carbide papers series and a 1μm diamond suspension on a cloth with a polishing machine (PM5, Logitech, UK). Before qBEI

measurements (see section 2.3.2), the polished surfaces of the samples were covered with a thin carbon layer by vacuum evaporation (SEM Caraon coater, Agar Scientific Limited). The layer was polished away before indentation.

2. Stained samples for histological analyzes and (polarized) light microscopy (Fig. 2.2 c-f):
   Fresh, undecalcified, dehydrated in graded series of ethanol samples were embedded in poly(methylmethacrylate) (PMMA, Merck Schuchardt OHG, Hohenbrunn, Germany), which infiltrates the structures. Approximately 5 μm thin longitudinal sections of MTLT were prepared with a microtome (Leica SM 2500). These sections were stained with Goldner's trichrome stain Gruber (1992); Fratzl-Zelman et al. (2004) and used for light microscopy observations (Axiophot, Zeiss).

3. Samples for light microscopy (Fig. 2.2 a-b):
   Fresh, undecalcified, dehydrated in graded series of ethanol samples were embedded in poly(methylmethacrylate) (PMMA, Merck Schuchardt OHG, Hohenbrunn, Germany). Transverse ground sections of approximately 80 μm thickness were performed with a polishing machine (PM5, Logitech, UK) for transmission light microscopic observations (Axiophot, Zeiss).

4. Samples for ashing and demineralization:
   Residual parts of the mineralized tendons (approximately 30-40% or 60-70% of the hard mineralized tendon length) were analyzed with ashing and demineralization. Fresh, undecalcified and non-dehydrated samples were used.

2.3.2 Estimation of mineral and collagen volume fractions

A scheme of mineralized collagen fibers present in MTLT is shown in Fig. 2.1. The collagen fibrils (up to 500 nm in diameter, depending on the tissue and stage of development Canty and Kadler (2005)) assemble in fibers with diameters up to 30 μm. These in turn create fiber bundles (or fiber arrays). The packing of mineralized collagen fiber arrays implies varying amount of microporosity.

Using quantitative backscattered electron imaging (qBEI) the intensity of electrons backscattered from a thin surface layer (1,5 μm in thickness) of a sectioned sample area was measured and correlated to the concentration of mineral in a sample Roschger et al. (1998). qBEI images were captured using digital scanning electron microscope with a fourquadrant semiconductor backscattered electron detector (DSM 962, Zeiss), at a working distance of 15 mm. Probe current was adjusted to 110 $\pm$ 0,4 pA and electron beam energy used was 20 keV. In each of the 39 sections of MTLT prepared

Symbol	Variable
α	Mineral distribution parameter between the fibrils and extrafibrillar matrix ($\alpha = 1$: all mineral placed within the fibrils)
${}^{Ca,fi}\psi$	Mass fraction of calcium in the fibrils
${}^{mi,fi}\psi$	Mass fraction of the mineral in the fibrils
${}^{col,fb}\psi$	Mass fraction of the collagen in fiber array
${}^{mi,fi}\phi$	Volume fraction of the mineral in the solid constituents of MTLT - no porosity considered
${}^{mi,fb}\phi$	Volume fraction of the mineral in the fiber array (with micro- and nanoporosity)
${}^{p(micro),fb}\phi$	Volume fraction of the micropores in the fiber array
${}^{p(nano),fb}\phi$	Volume fraction of the nanopores in the fiber array
${}^{col,fb}\phi$	Volume fraction of the collagen in the fiber array
${}^{cir}\phi$	Volume fraction of the circumferential zone
${}^{int}\phi$	Volume fraction of the interstitial zone
${}^{mi}\rho$	Density of the mineral
${}^{col}\rho$	Density of the collagen
${}^{org}\rho$	Density of the organics
${}^{tot}m$	Total mass of the tissue
${}^{mi}m$	Mass of the mineral
${}^{org}m$	Mass of the collagen
${}^{tot}V$	Total volume
${}^{ind}E_{fb(exp)}$	Measured indentation modulus
${}^{ind}E_{fb(com)}$	Computed indentation modulus

Table 2.1: Nomenclature used in this manuscript was defined in a way that ϕ stands for volume fraction and ψ for mass fraction. The first part superscript means the quantity described (mi - mineral, col - collagen, org - organics, Ca - calcium, p(nano) - nanoporespores, p(micro) - micropores). The second part of the superscript (after a comma) means the quantity over which the fraction is calculated (fi - fibrils, fb - fiber array). Additionally subscript cir or int refers to the circumferential or interstitial zones.

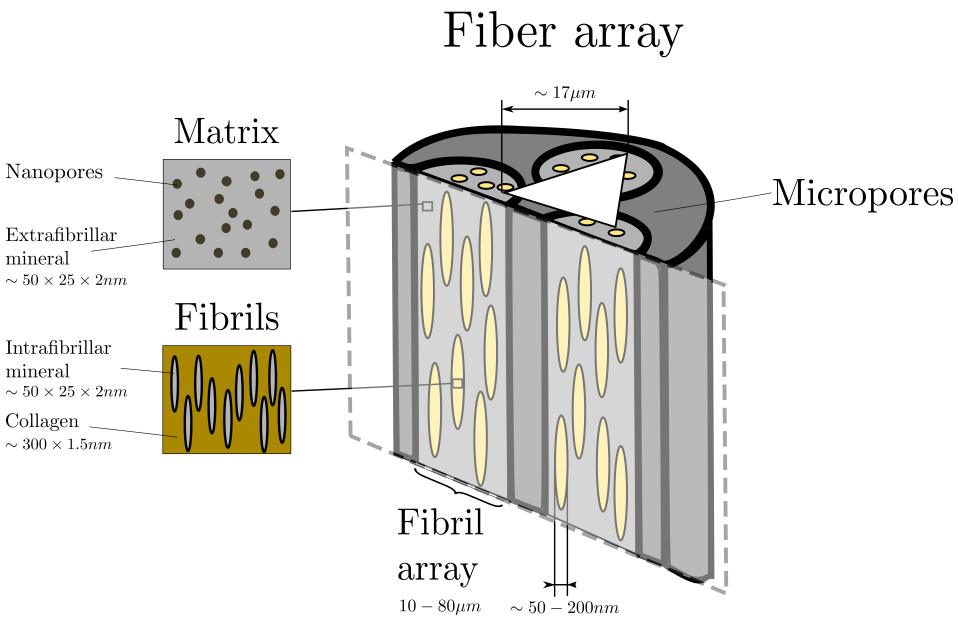

Figure 2.1: Graphical representation of the fiber array consiting of mineralized collagen fibrils, mineralized extrafibrillar matrix and micropores. Fibrils consist of collagen and intrafibrillar mineral, and the matrix consists of extrafibrillar mineral and nanopores. Microindentation imprint averaging the properties of a fiber array is schematically represented in white. The proportions are not preserved

according to point one in section 2.3.1, 6-10 regions containing both circumferential and interstitial morphology were selected randomly for the 400 magnification qBEI images (image size approximately 250 x 315 μm). qBEI images were analyzed for area fraction for nonmineralized sample areas (soft tissue and/or pure embedding medium/pores) by thresholding. The grey level range above this threshold represented the areas of mineralized tissue. Macroporosity defined as the sum of vascular porosity (large rounded pores visible with μCT and qBEI) was thresholded. The average mineral content of two morphologically different tissue zones, circumferential and interstitial, were evaluated from grey-levels of images, separately. Even though the biological apatites are non-stoichiometric, with presence of foreign ions Bigi et al. (1996), the inorganic phase consisting of carbonated calcium phosphate was idealized as hydroxyapatite $Ca_{10}(PO_4)_6(OH)_2$. The fractions of calcium in the solid constituents of MTLT ($^{Ca,fi}\psi$) evaluated from grey-levels of images Roschger et al. (1998), were converted to hydroxyapatite mass fractions ($^{mi,fi}\psi$) using stoichiometric relationships.

Mass factions of mineral were converted to volume fractions ($^{mi,fi}\phi$ - volume fraction of mineral in the solid constituents of MTLT - no porosity

considered) according to Roschger et al. (1995); Manjubala et al. (2009) using the density of hydroxyapatite of $3.18g/cm^3$ and density of collagen $1.47g/cm^3$ Manjubala et al. (2009), see Equation 2.1.

$$^{mi,fi}\phi = \frac{1}{1 + \frac{^{mi}\rho}{^{col}\rho}(\frac{1}{^{mi,fi}\psi} - 1)} \tag{2.1}$$

To estimate mineral volume fractions at the fiber array level ($^{mi,fb}\phi$), both volume fractions of micropores obtained by light microscopy for the two morphology zones ($^{p(micro),fb}\phi_{cir}$, $^{p(micro),fb}\phi_{int}$) and nanopores estimated based on Fritsch et. al. ($^{p(nano),fb}\phi \sim 0.23$) Fritsch and Hellmich (2007) were added, see Equation 2.2. The quantitative evaluation of mineralization was performed using the higher magnification images (400x), while the two lower magnifications (50x, 200x) served as sample maps allowing recognition of the qBEI-imaged regions for indentation. 526 regions of interest were selected.

$$^{mi,fb}\phi = ^{mi,fi}\phi(1 - ^{p(nano),fb}\phi - ^{p(micro),fb}\phi) \tag{2.2}$$

Samples prepared for ashing and demineralization, with length of about 10mm were scanned using a μCT40 scanner (Scanco Medical) with 12 μm isotropic spatial resolution. The samples were scanned in air, using an X-ray tube potential of 20 - 50 keV (160 ďż˝ďż˝A). The whole samples (approximately 10mm) were chosen as volume of interest. The tissue mineral density (TMD) was determined according to Bouxsein et al. Bouxsein et al. (2010). The average difference in mineralization (TMD) observed with μCT between the three adjacent slices was 1.48% and was considered negligible. Six MTLT samples adjacent to the samples from the main procedure were ashed in a laboratory furnace at 650°C for 24 hours Ohman et al. (2007). The six ashed samples came from five different animals. Two were distal, four proximal with respect to the main procedure samples. Five samples were demineralized in EDTA solution for 20 days Ehrlich et al. (2009). The samples came from five different animals. Three were distal, two were proximal to the original location. qBEI images of MTLT showed some additional unmineralized tissue outside of the tendon (soft tissue envelope) and also at the edges of pores (see Fig. 2.3 c, white arrows). Volume fraction of this organics was quantified and then assuming non-mineralized collagen density of $1.47g/cm^3$ Manjubala et al. (2009), the extra organics mass was subtracted from the total mass measured in ashing and demineralization experiments. The total mass of a sample was than decomposed into a mass of mineral and mass of organics (in the mineralized tissue): $^{tot}m = ^{mi}m + ^{org}m$. An average organics density in a sample $^{org}\rho$ was calculated with the Equation 2.3, where ^{tot}V is a total volume of a sample obtained with μCT, $^{p(micro),fb}V$ is the sample specific microporosity ($^{p(micro),fb}V = ^{tot}V\ ^{p(micro),fb}\phi$) and $^{mi}\rho$

is the density of hydroxyapatite ($3.18 g/cm^3$ Manjubala et al. (2009)).

$$ {}^{org}\rho = \frac{{}^{org}m}{{}^{tot}V - \frac{{}^{mi}m}{{}^{mi}\rho} - {}^{p(micro),fb}V} \tag{2.3} $$

Volume fraction of organics ${}^{org,fb}\phi$ for each sample was calculated from the ashing/demineralization data and the sample-wise collagen density, using Equation 2.4.

$$ {}^{org,fb}\phi = \frac{{}^{org}m}{{}^{org}\rho {}^{tot}V} \tag{2.4} $$

The assumption that 90% of organics in MTLT is collagen type I Landis and Silver (2002); Fritsch and Hellmich (2007) was used (Eq. 2.5) in order to estimate the volume fraction of collagen that contributes to the mechanical properties of the samples (${}^{col,fb}\phi$). The rest 10% of organics was treated as nanopores.

$$ {}^{col,fb}\phi = 0.9 {}^{org,fb}\phi \tag{2.5} $$

In the course of the study two zones of distinct morphology were noted in MTLT, as described in detail in the results section of this manuscript. In these zones, called circumferential and interstitial, volume fractions of collagen (${}^{col,fb}\phi_{cir}$ and ${}^{col,fb}\phi_{int}$) were evaluated separately in a least squares minimization procedure:

$$ {}^{col,fb}\phi = {}^{col,fb}\phi_{cir} \; {}^{cir}\phi + {}^{col,fb}\phi_{int} \; {}^{int}\phi, \tag{2.6} $$

resulting with a coefficient of determination $R^2 = 0.61$ ($n = 10$). Average volume fractions of a morphology zone in a sample (${}^{cir}\phi$, ${}^{int}\phi$) were evaluated from qBEI images used for the mineralization quantification (400x magnification).

2.3.3 Fiber array model

Mean field methods were applied to model mineralized fiber arrays of MTLT. This fiber arrays were composed of mineralized collagen fibrils, the extrafibrillar matrix Reisinger et al. (2010) and micropores (see Fig. 2.1). Mineralized collagen fibrils were modeled as continuous collagen matrix with spheroidal mineral inclusions. Extrafibrillar matrix was modeled as continuous mineral matrix with spherical voids (a mineral foam). Mineralized collagen fibers were modelled as long spheroidal fibrils in the extracellular matrix with additional micropores.

Stiffness tensors were computed as a function of degree of mineralization (${}^{mi,fb}\phi$), mineral distribution between fibrils and extra-fibrillar matrix (α varied between 0.05 to 0.95, with α=1 meaning the whole mineral placed within the collagen fibrils) and fibril volume fraction (${}^{fl,fb}\phi$), as well as stiffness of hydroxyapatite and collagen. Less influential parameters as collagen

and mineral Poisson ratios, mineral platelet aspect ratio, void aspect ratio in extrafibrillar matrix and fibril aspect ratio in the fibril array, were kept at the operation point used by Reisinger et. al. Reisinger et al. (2010). Dried conditions were simulated with the stiffness of collagen of 5 GPa (in the range cited in the literature Buehler (2007); van der Rijt et al. (2006); Akkus (2005)). Indentation moduli ${}^{ind}E_{fb}(com)$ were calculated from the obtained stiffness tensors based on the Swadener and Pharr theory Swadener and Pharr (2001).

2.3.4 Microindentation

An indentation technique was applied to measure indentation moduli of MTLT, ${}^{ind}E_{fb(exp)}$. This technique involves the application of controlled load to the surface to induce local surface deformation with monitoring of load and displacement during the loading and unloading. Indentations were performed in the regions of interest where the mineral content was quantified with qBEI, placing 30-60 indents in each 400x magnification qBEI image using a light microscope of the indenter to avoid lacunae, micropores or other surface defects. Indentations were performed in dried conditions using Nano-Hardness Tester (CSM Instruments, Peseux, Switzerland) with a Berkovich indenter. The measurements were conducted in load control to a maximal displacement of 2.5 μm (resulting in the deformation region of approximately 17 μm in diameter), what allowed for characterization of the tissue at the fiber array hierarchical level (including the mineralized collagen fibers and micropores, see Fig. 2.1). Indentation protocol involved trapezoidal loading/unloading with constant rate of 120 mN/s with 60 seconds holding time at maximum load to minimize the viscoelastic and/or viscoplastic effects.

Outliers were defined as values higher than 1.5 times the interquartile range above the third quartile and below the first quartile Crawley (2005). Distribution of the indentation moduli were checked using a Shapiro-Wilk normality test Crawley (2005). Welch two tailed t-test was used for means comparison.

2.4 Results

The investigated mineralized turkey leg tendons (MTLT) showed two types of morphology, as visualized by light microscopy and qBEI (Fig. 2.2 and 2.3). A circumferential region around large pores (blood vessels), with collagen fibers densely packed and smaller in diameter, in contrast to an interstitial region in between the large pores with more loosely arranged fibers of larger diameter (Fig. 2.2 a, b). The microscopical views of the transverse and longitudinal section of MTLT together with linearly polarized light images (Fig. 2.2 a,b,c,d) confirmed the uniaxial alignment of the collagen fibers in

these samples. In the circumferential region a high concentration of elongated lacunae could be observed in the mineralized fiber matrix (Fig. 2.2 c,d and Fig.2.3 f). In the longitudinal section of qBEI images also cuboidally shaped cell lacunae (possibly originating from the endotendon connective tissue cells) are visible in the interstitial region (Fig. 2.3 e, f). The Goldner's trichrome stained section displayed non-mineralized collagenous tissue around large channels (e.g. blood vessels) and at the peripheries of the tendon stained red, while the mineralized tissue was stained green (Fig. 2.2 e, f). These regions could also be distinguished in the qBEI images as an intermediate grey-level between the pores and the mineralized tissue (Fig. 2.3 c, white arrows).

Considering the arrangement of the interstitial and circumferential regions, the samples from regions closer to the mineralization front showed no or only a low fraction of circumferential morphology and the macro pores were directly in contact to these zones (Fig. 2.3 a). With more distance from the mineralization front most of the interstitial regions were closely attachted to circumferential structures and only very few areas which were directly in contact with macro pores were observed (Fig. 2.3 b,c,d). The qBEI images gave the impression, that the circumferential structures were formed later upon a preexisting interstitial structure.

Some features resembling resorption sites were observed (Fig. 2.3 c), although no histology showing cells or fluorochrome labels were used. In absence of those, the modeling and remodeling sites are indistinguishable.

The average volume fraction of collagen was higher in the circumferential zone (${}^{col,fb}\phi_{cir} = 0.50 \pm 0.02$), than in the interstitial one (${}^{col,fb}\phi_{int} = 0.28 \pm 0.02$, with one sample discarded as an outlier in the demineralization procedure), see Tab. 4.1. The average tissue mineral density (TMD) of MTLT measured with μCT was 898 mg/cm^3.

Mineral mass fraction in the interstitial zone was higher (${}^{mi,fb}\psi = 0.65$), than in the circumferential one (${}^{mi,fb}\psi = 0.54$). One specimen was damaged and discarded from qBEI analyzes. No additional outliers were discarded from qBEI analyzes of the images means. Porosity had no influence on mineral mass fractions, but when the nano- and microporosities were included in the calculation of mineral volume fractions in the fiber array (${}^{mi,fb}\phi$, see Eq. 2.2), the overall mineralization was higher in the circumferential zone - the one with lower micropores volume fraction, see Tab. 4.1.

The average volume fractions of micropores (${}^{p(micro),fb}\phi$) estimated from light microscopy images of thin cross-sections of MTLT (prepared according to point 3 in section 2.3.1) were 0.18 ($\pm$0.07) and 0.37 ($\pm$0.14) for circumferential and interstitial zones, respectively. Deviation of this measurements is high, as there is a wide distribution in porosity in MTLT seen by light microscopy, especially in the interstitial zone. No outliers were considered in microporosity evaluation.

Average density of organics in the ashed samples (1.83 $\pm$ 0.32 g/cm^3)

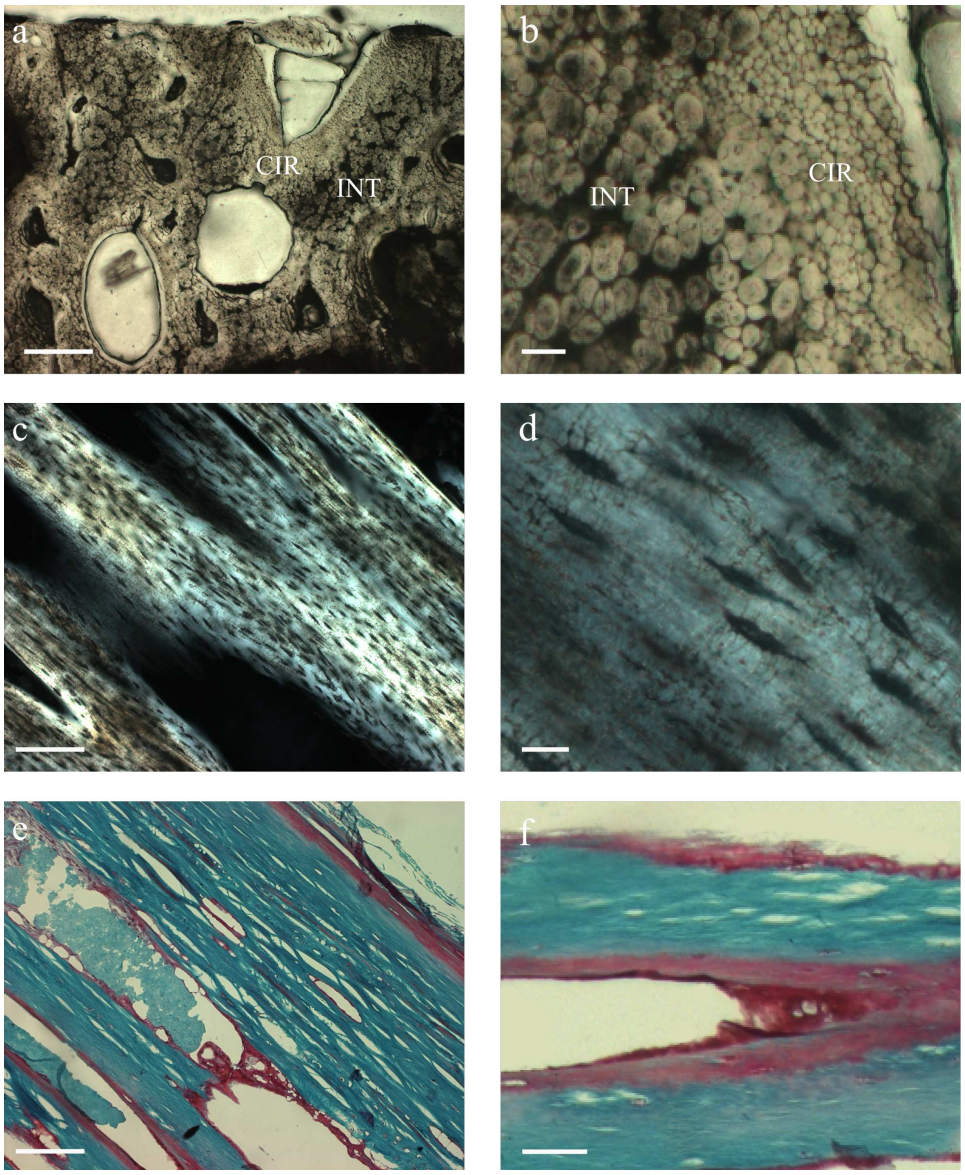

Figure 2.2: Light microscopy images of transverse and longitudinal sections of MTLT: a) a cross-section of MTLT showing different organization of the mineralized collagen fibers in the two morphology zones. Bar - 100μm. b) ciraumferential zone with smaller average fiber diameter and denser packing (on the right), interstitial zone with larger, more loosely packed fibers (on the left). Bar - 10μm. c) Tenocytes placed along the collagenous fibers in ciraumferential zone. Bar - 40μm. d) The tenocytes show high similarity to osteocytes. The lacuno-canalicular system is present. Bar - 10μm. e) Nonmineralized tissue is observed at the peripheries of the tendon and in the vicinity of blood vessels (stained red with the Goldner's trichrome stain). Bar - 100μm. f) Non-mineralized collagen fringes around a vascular canal (ciraumferential zone) resemble a bone matrix at a forming site of bone (osteoid). Bar - 25μm

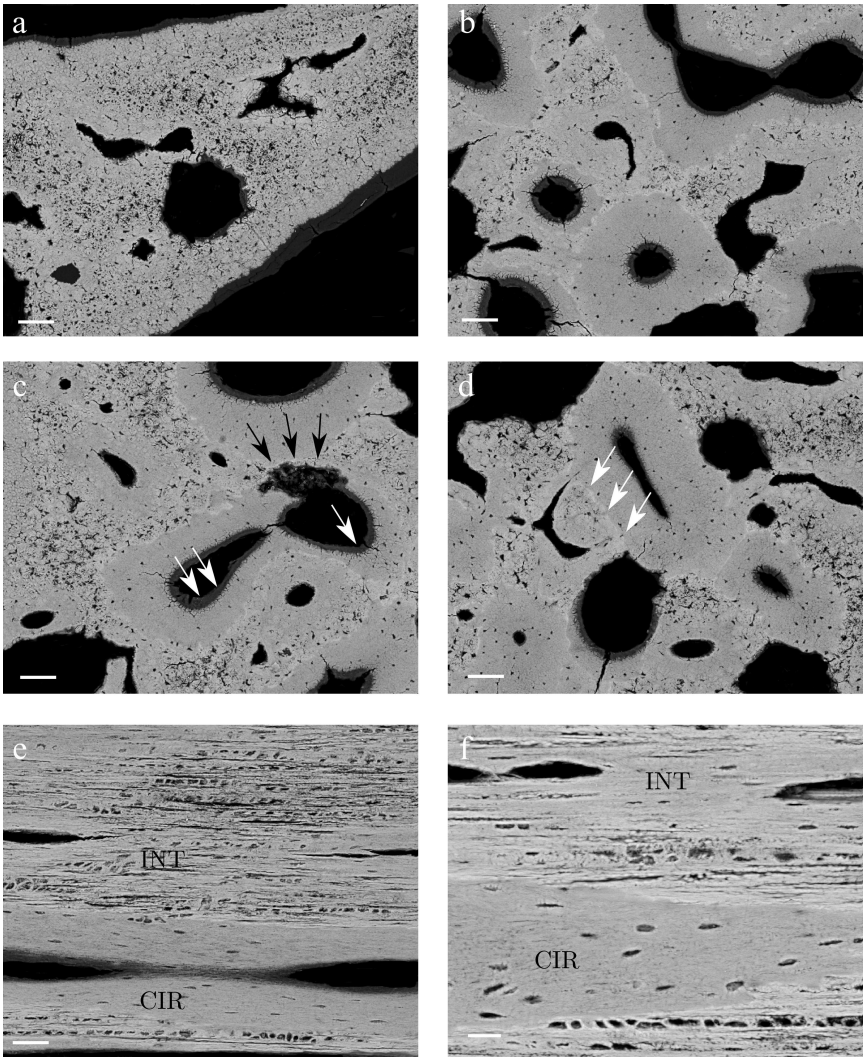

Figure 2.3: Quantitative backscattered electron images of transverse and longitudinal sections of MTLT. a) Transverse section taken from a proximal part. Uniformly mineralized, large fibers are present, no remodeling sites or ciraumferential zones are present. Bar - 50μm. b) More distal part of a mineralized tendon (older mineral deposits present there). Two types of morphologies can be observed: the ciraumferential region - around the large pores - showing lower mineralization and the interstitial zone with larger, more spread fibers and higher mineralization - resembling the type of morphology seen in vicinity to the mineralization front. Highly mineralized lines resembling the cement lines are visible at the borders between the morphology types. Bar - 50μm. c) A structure resembling a resorption cavity. Bar - 50μm. d) Interstitial zone with distinguishable mineralized collagen fibers. Bar - 15μm. e) Longitudinal section of MTLT showing the two types of the tissue (interstitial on the top and the ciraumferential on the bottom). Bar - 50μm. f) Longitudinal section of MTLT. Cells of different geometries are observed in the two morphology zones. Cuboidal tenocytes are present in the interstitial part of tendon (bottom), while in the ciraumferential regions, the cells resemble osteocytes. Bar - 25μm

Zone	${}^{mi,fi}\psi$	${}^{mi,fi}\phi$	${}^{mi,fb}\phi$	${}^{col,fb}\phi$	${}^{p(micro),fb}\phi$	α	${}^{ind}E_{fb(com)}$	${}^{ind}E_{fb(exp)}$ (STD)
Circumferential	0.54	0.35	0.21	0.50	0.18	0.7	13.64	13.68 (0.83)
Interstitial	0.65	0.46	0.18	0.28	0.37	0.3	12.36	12.19 (1.05)

Table 2.2: Morphological parameters of the fibril and fiber arrays in the two zones of MTLT. ${}^{mi,fi}\psi$ - mass fraction of mineral in the solid constituents of MTLT - no porosity considered, ${}^{mi,fi}\phi$ - volume fraction of mineral in the solid constituents of MTLT - no porosity considered, ${}^{col,fb}\phi$ - volume fraction of the collagen in the fiber array, ${}^{fl,fb}\phi$ - volume fraction of the fibrils in the fiber array, ${}^{ind}E(exp)$ - average indentation modulus in axial direction with standard deviation (STD), ${}^{ind}E_{fb}(com)$ indentation modulus in axial predicted with the mean field model and α - mineral distribution parameter between fibrils and extrafibrillar matrix. Indentation moduli are given in GPa, mass and volume fractions, as well as α are dimensionless

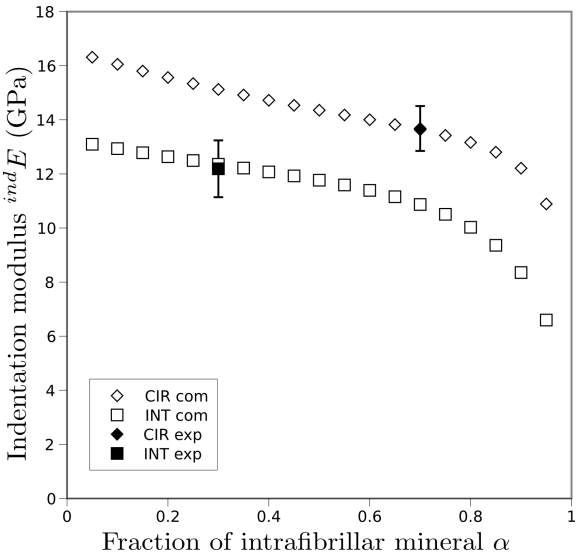

Figure 2.4: Indentation moduli predicted with the fiber array model (dependend on mineralization, porosity and mineral distribution parameter α) as a function of α for the ciraumferential (CIR com) and interstitial (INT com) zones of MTLT. Additionally the experimentally obtained indentation moduli in the two zones (CIR exp, INT exp) with one standard deviation is plotted

was higher than the one cited in the literature for dry collagen fibrils (1.29 g/cm^3 Gautieri et al. (2011) to 1.47 g/cm^3 Manjubala et al. (2009)).

Over 2300 indentations were performed in MTLT in the dried conditions, separately in the circumferential and interstitial zones of which 188 indents were discarded as outliers (defined as described in section 2.3.4). Distribution of the sum of indents in circumferential and interstitial zones showed significant departures from normality with p-value 0.002. When two groups were separated the distribution showed no departures from normality in both zones (p-value higher than 0.05). Indentation modulus in the circumferential zone measured dry was significantly higher (mean 13.68 GPa $\pm$ 0.83 GPa) than indentation modulus of the interstitial zone (mean 12.19 GPa $\pm$ 1.05 GPa; Welch two tailed t-test, Crawley (2005); $p < 0.0001$).

Indentation moduli measured in two orthogonal directions of the two morphological zones of MTLT ragning in the anisotropy ratios of the zones are described in Chapter 4, along with the re-hydration effects on the indentation modulus.

Indentation moduli predicted with fiber array model $^{ind}E_{fb(com)}$ were compared to indentation moduli obtained with indentation in the two morphological zones. The predicted indentation moduli as a function of mineral

distribution parameter, as well as the experimentally obtained indentation moduli for the two zones are presented in Figure 2.4. Results of microindentation in the circumferential zone were within one standard deviation with the modulus predicted with the mean field model with the mineral distribution parameter 0.55-0.90. The same holds in the interstitial zones, with average experimental indentation moduli and predicted average indentation modulus with α lower than 0.55.

2.5 Discussion

The combined experimental and numerical study on stiffness of MTLT revealed good agreement of the experimental data obtained by microindentation with values predicted with a numerical model based on the mean field method, with input data of mineral and collagen content and porosity obtained by qBEI, ashing/demineralization and light microscopy. The study reveals two morphological regions in MTLT. The interstitial zone with the large in diameter, rather poorly organized and loosely packed fibers, on which the circumferential zone of smaller, but well organized and tightly packed fibers is apposed (Fig. 2.2 a, b). Hence, the interstitial zone seems to be the primary structure on which the circumferential is formed. This concept is supported by the fact that near the mineralization front of MTLT only tissue of interstitial character is found, while in the more mature region (closer to mid-region of the MTLT) higher fraction of the circumferential tissue is present (Fig 2.3 a,b). Further features similar to eroded surfaces and cement lines in bone seen in qBEI images (Fig 2.3 c - black arrows and d - white arrows, respectively) are suggesting, that in MTLT a process of (re)modeling is potentially occurring. Moreover, Knott at. al. Knott et al. (1997) have shown, based on a collagen cross-linking patterns (high level of hydroxylation of specific triple-helical lysines), that the proximal tendons are predestined to mineralize. Thermal properties of the collagenous matrix in the proximal and mid sections of a tendon showed that different types of matrix are formed at each site [40]. This would be consistent with the finding that the circumferential zone (with new collagen matrix and mineral deposits) is a product of tissue (re)modeling. However, the evidence of such a (re)modeling process in MTLT needs to be confirmed by demonstrating histologically the presence of cells absorbing fiber material and cells producing new fiber material with the fluorescent bands of fluorochrome labeling.

When considering the mineralized collagen fibers orientation as seen by the histological analysis, it is interesting that in both zones, interstitial and circumferential, the fibers are strongly aligned to the longitudinal axis of the tendon (Fig. 2.2 c, e, f). This could be caused by the fact that the tendon is mostly loaded in tension, in contrast to lamellar bone, where the loading conditions are much more complicated, what is reflected in a complex

arrangement of the mineralized collagen fibrils in this tissue.

In the interstitial zone the estimated volume fraction of the fibrils in the fiber array is lower than in the circumferential zone. Volume fraction of the extrafibrillar matrix is lower in the circumferential zone. The mineralization process in this possibly newly build tissue may start in the collagen fibrils. After filling the intra-fibrillar spaces, the mineralization may progress to the matrix, depending on the space available. The space inside a collagen fibril available for mineralization was theoretically calculated by Jaeger and Fratzl Jaeger and Fratzl (2000). The upper possible limit of mineral volume fraction fitting in the gap and overlap regions of collagen fibril was ${}^{mi,fi}\phi_{max}$ = 0.56. The Hodge-Petruska longitudinal staggered model of a 2D collagen arrangement in a fibril Hodge and Petruska (1963) was extended to 3D and used for calculations. Recently a newer model of lateral packing arrangement in collagen fibrils was proposed by Burger et al. Burger et al. (2008). They found that the lateral packing of mineral crystals in collagen fibrils can be represented as an irregular stacks of platelet-shaped crystals, intercalated with layers of collagen molecules. The maximal volume fraction of mineral fitting into a collagen fibril in such a model was not reported. The amount of extra-fibrillar mineral in the circumferential zone does not reach the limit calculated by Jaeger et al. Jaeger and Fratzl (2000), before spreading into the extracellular matrix, which may suggest that the mineralization may take place in both locations, inside and on the surfaces of a collagen fibril Landis et al. (1996). This is possible since the nucleation events were shown to be spatially independent during the onset and progression of mineralization Glimcher (2006).

Lees et. al showed that the mineral in MTLT is mostly placed in the extra-fibrillar matrix (70-75%) Lees and Page (1992); Lees et al. (1994, 1996). Our micromechanical modeling approach also suggests that the mineral in the interstitial zone is mostly extrafibrillar (α below 0.55 meaning 55% or less of the total mineral is infiltrating the fibrils). This may be caused by the fact that the penetration of mineral into the large collagenous fibers may be limited in this zone, as there are the large collagen fibers of a tendon already existing at the onset of mineralization.

The average weight fraction of mineral in the tissue obtained by qBEI is about 0.58, somewhat higher than average in trabecular bone (about 0.55 Roschger et al. (1998)) and MTLT of younger, 24 weeks old birds (about 0.51 Gupta et al. (2004)). The mineralization in circumferential zone (average weight fraction of mineral 0.54) is similar to the trabecular bone mineralization. As the two zones show different average volume fractions of collagen (${}^{col,fb}\psi_{cir} = 0.50$ and ${}^{col,fb}\psi_{int} = 0.28$), as well as different microporosities (${}^{p(micro),fb}\phi_{cir} = 0.18$ and ${}^{p(micro),fb}\phi_{int} = 0.37$), the trend of higher mineralization in interstitial zone is reversed when looking at the volume fraction on mineral at the hierarchical level of the fiber array.

The density of organics measured in MTLT was higher than the average

value cited in the literature Gautieri et al. (2011); Manjubala et al. (2009); Evans et al. (2001); Lees and Page (1992). The reason might be the way of accounting for the collagen fibril volume in the case when it is infiltrated with mineral. The volume assigned to collagen might be shared by mineral and collagen resulting in a lower volumes sum than the sum of the volumes when the two phases are separated. The mass is preserved, so the resulting density must increase.

In the mean field model, the estimated volume fraction of the fibrils is next to the overall tissue mineralization a highly influential parameter determining the tissue stiffness, as showed by Reisinger et al. Reisinger et al. (2010). This parameter together with the mineral distribution (α) was shown to have a high sensitivity in the tissue stiffness determination. The extrafibrillar mineralization (dependent on α and ${}^{mi,fi}\phi$) was shown to considerably enhance the overall stiffness of a fiber Nikolov and Raabe (2008). In the absence of validated techniques to assess for example the mineral distribution parameter α, the mean field model can help in describing trends. In this study, α and the collagenous phase stiffness were the only two parameters not assessed experimentally, that were shown to have a high or moderate sensitivity on stiffness of the fibril array (Reisinger et al. 2010). The values of collagen stiffness reported in the literature range from 0.3 - 9 GPa (Gautieri et al., 2011), with the average stiffness of collagen molecule based on 10 publications using a variety of experimental and modeling methods of 4.8 (0.2) GPa. The average stiffness of collagen microfibril in dried state based on AFM testing and atomistic modeling was 3.26 GPa and in the wet state 0.6 (0.2) GPa (Gautieri et al., 2011). The value of 5 GPa was chosen in order to describe the dried collagen properties, based also on previous study by Reisinger et al. (2010), where this value was used as operating point for dried bone. Collagen stiffness could be seen as a scaling factor, but its sensitivity on axial stiffness is limited Reisinger et al. (2010). Fixing the collagen stiffness (equal for both circumferential and interstitial zone), α was the only unknown.

Comparing the experimental indentation moduli results with the ones predicted with the model with a range of α, we were able to estimate the possible mineral distribution parameter for the two zones (as shown in Fig. 2.4 by the two experimental points). This is a rough estimation, but in the absence of clear experimental evidence, the mean field model could be a helpful tool in speculating the mineral distribution in the two zones of MTLT.

The suggested highly mineralized extrafibrillar matrix in the interstitial zone of MTLT may be a reasonable mean to overcome the high microporosity in this zone (${}^{p(micro),fb}\phi$=0.37) in order to enhance the stiffness. The circumferential zone, with lower weight fraction of mineral, shows higher mechanical properties possibly due to the mineral distribution and its volume fraction (as opposed to the mass fraction seen on qBEI images), volume

fractions of organic phase and micropores. According to the model predictions more mineral is placed within the collagen fibrils in this zone ($\alpha \sim 0.7$), which is disadvantageous in terms of stiffness, but this seems to be compensated with higher volume fractions of the fibrils in a fiber and microporosity much lower than in the interstitial zone.

The mean field modeling gives some insights into the possible phases arrangement in MTLT. The downside of such a multiscale micromechanical models is the fact that a given final stiffness result can be achieved with many possible configurations of input parameters. In this sense the results obtained here should be treated with caution until the experimental techniques that can confirm the phases relationships (for example the mineral distribution parameter α) at the nano and micro levels are developed. Meanwhile some trends can be described.

Drying artifacts were noticed in qBEI images. Especially in the cross-sections of the circumferential zone some radial cracks originating from the large pores are present. Both qBEI and light microscopy measurements were performed in dried state, which is one of the limitations of the study. Shrinking on drying may change the packing density of the mineralized collagen fibrils and fibers. The extent of swelling may be larger in vitro than in vivo, as the fibers in physiological conditions are constrained with one another. Different amount of swelling may also be expected in the two zones of morphology. The circumferential zone is more densely packed, leaving less space for dimension changes in aqueous environments. Interstitial zone shows higher microporosity, which in vivo is likely filled with fluid. More space for swelling is available there. On the other hand, the extrafibrillar mineral may limit the potential swelling.

It is known that the mechanical properties of a mineralized tissue are dependent on structural and organizational interactions of mineral and collagen at many hierarchical levels. Although the overall mineralization has been extensively used as the main (and often only) factor predicting the mechanical properties of bone, it is becoming clear that there are other important contributions that have to be considered. This work shows the importance of morphological arrangement of phases and microporosity in mineralized tissues on local elastic properties. Different morphology types were shown in mineralized turkey leg tendon, which suggests remodeling of the tissue. Differences in the tissue organization in these zones on their stiffness were assessed experimentally. Mean field models of the mineralized fibers in the two zones provided a possible explanation of the stiffness differences. Especially mineral distribution between the collagen fibrils and extrafibrillar matrix and the tissue density were shown to have an impact on stiffness.

2.6 Acknowledgements

This research was supported by grant no P19009-N20 of the Austrian Science Foundation (FWF). Authors would like to thank Peter Varga for providing the samples and help with image processing, Andreas Reisinger for advice in modeling, Phaedra Messmer for technical assistance with qBEI measurements, Gerda Dinst and Kamilla Nawrot-Wawrzyniak for sample processing.

Chapter 3

Quantitative polarized light microscopy

This Chapter describes a calibration study of the polarized light microscopy technique for the assessment of collagen put-of-plane angle in bone sections.
Based on manuscript:
"A quantitative collagen fibers orientation assessment using birefringence measurements: calibration and application to human osteons."
By Ewa M. Spiesz, Werner Kaminsky and Philippe K. Zysset.
Published in Journal of Structural Biology (2011), doi:10.1016/j.jsb.2011.09.009.

3.1 Abstract

Even though mechanical properties depend strongly on the arrangement of collagen fibers in mineralized tissues, it is not yet well resolved. Only a few semi-quantitative evaluations of the fiber arrangement in bone, like spectroscopic techniques or circularly polarized light microscopy methods are available. In this study the out-of-plane collagen arrangement angle was calibrated to the linear birefringence of a longitudinally fibered mineralized turkey leg tendon cut at variety of angles to the main axis. The calibration curve was applied to human cortical bone osteons to quantify the out-of-plane collagen fibers arrangement. The proposed calibration curve is normalized to sample thickness and wavelength of the probing light to enable a universally applicable quantitative assessment. This approach may improve our understanding of the fibrillar structure of bone and its implications on mechanical properties.

3.2 Introduction

Composites with fibers reinforcement are a very frequent motives in the design of natural materials (Fratzl and Weinkamer, 2007). A complex design is required as fibers are usually strong in tension, but rather weak in compression, as they tend to buckle easily. Tissue mineralization is widely used as a predictor of mechanical performance of mineralized tissues, but as the correlation between the mineral content and stiffness measured for example with nanoindentation technique is rather moderate (Boivin et al., 2008; Follet et al., 2004; Zebaze et al., 2011), the attempts of including other factors like morphology of the organic matrix are gaining attention Siegmund et al. (2008); Willems et al. (2011). Not only volume fraction of organic matter (Reisinger et al., 2010), but also spatial arrangements are of interest for understanding the exceptional elastic properties of bone. The question of how the mineralized collagen fibers are arranged in the extracellular matrix of bone was investigated for over a century, but there is no full agreement on its details. A first model of arrangement of collagen in lamellae was proposed by Gebhard in 1906 (Gebhardt, 1906). The model assumed an unidirectional arrangement of the fibers with an abrupt change of 90^o between neighboring lamellae. The next model by Ascenzi et. al. (Ascenzi and Bonucci, 1967, 1968) assumed osteons with mainly longitudinal, transverse or alternating fibril orientation. More recent works present a view that the arrangement of fibers in a lamella follows a certain orientation pattern. The most popular models are the orthogonal plywood pattern similar to the model of Gebhard and that of twisted plywood, characterized by a continuous fibril rotation. A more refined model was proposed by Weiner et al. (1997, 1999), where a single lamella is divided into 5 sublayers with consecutive rotation of the fibers of 30^o. A simulation study by Reisinger et al. (2010) showed that different collagen orientation patterns lead to diffrent elastic properties and anisotropy of a lamella. The models fitting the experimental nanoindentation results best were those by Weiner (Weiner et al., 1999; Wagermaier et al., 2006).

Some methods of direct measurement of collagen out-of-plane orientation (the angle that collagen fibers make with the normal to the specimen surface) are available, like for example scanning small angle X-ray scattering (SAXS) and wide angle X-ray diffraction (WAXD) (Wagermaier et al., 2006). Polarized light measurements were applied to assess the collagen arrangement, but not in a fully quantitative way by Martin and Ishida (1989); Boyde and Riggs (1990); Hengsberger et al. (2002b); Bromage et al. (2003) and Skedros et al. (2009), even though birefringence measurement techniques are frequently used as a standard tool in studying anisotropic properties of materials for nearly 200 years (Pajdzik and M., 2006).

Quantitative birefringence assessment requires additional components for the optical set-up (like optical retarders, for the full filters arrangement

see Kaminsky et al. (2007)). Some methods allow quantitative measurements of two dimensional linear birefringence (Geday et al., 2000). An addition of a sample tilting stage provides three dimensional maps of birefringence and eigen rays (Pajdzik and M., 2006). Recently, a technique allowing a simultaneous imaging of birefringence from four quadrants of a single image at camera speed was developed by Kaminsky et al. (2007). This method, previously applied to some examples from the fields of biology and materials sciences, was here calibrated for the use on mineralized tissues (mineralized turkey leg tendon - MTLT and osteonal bone).

In previous implementations of polarized light methods, the assumption was made that osteons appear completely bright or dark when they are composed of mostly transversely or longitudinally oriented fibers (Boyde and Riggs, 1990; Martin et al., 1996). In between, a brightness ratio was used as indicator of the fraction of longitudinal versus transverse fibers in a sample (Boyde and Riggs, 1990; Ramasamy and Akkus, 2007). This allowed for a comparative evaluation of collagen arrangement in distinct parts of bone (Kalmey and Lovejoy, 2002; Goldman et al., 2003), but did not provide fully quantitative information on the out-of-plane collagen arrangement angle. Additionally the thickness of samples used in the studies was not included in transformation of the birefringence information to the preferred collagen arrangement angle and therefore had to be normalized (Boyde and Riggs, 1990). Alternatively a scale describing six secondary osteons morphotypes was proposed by Martin et al. (1996) and than updated by Skedros et al. (2009). The scale describes different osteons types based on birefringence patterns and assigns scores to each. Averaging over large fields of view results in an average score that is correlated to the average collagen arrangement in a bone section. No quantitative data on the actual out-of-plane collagen angle is provided, but the trends describing mostly transversely or mostly longitudinally arranged fibers are well represented.

As the anisotropy of bone structure reflects its organization, some acoustic microscopy studies could provide information about bone ultrastructure. Turner et al. (1995) measured the average out-of-plane collagen angle of 30^o in demineralized osteonal bone.

Some attempts of understanding the arrangement of collagen fibers in osteons was made using Raman microspectroscopic imaging (Kazanci et al., 2006, 2007; Gamsjaeger et al., 2010) providing insight into the organization of bone at the ultrastructural level. This technique requires critical data analysis due to a dependency of the mineral to matrix ratios on materials composition and/or orientation. Measurements of $\nu_1 PO_4$/amide I ratios as a function of light polarization angle showed trends that are promising for evaluation of collagen arrangement in bone (Gamsjaeger et al., 2010).

Another method of evaluation of collagen alignment in mineralized tissues is the second harmonic generation microscopy (SHG) that utilizes nonlinear scattering of photons from collagen fibers. Maps trends of collagen

being aligned more within or transverse to the measurement plane are created (Cox et al., 2003; Burket et al., 2011), but no quantitative information is available.

In this study we extended the idea of calibration of the circularly polarized light microscopy technique on an uniaxial mineralized collagenous tissue previously proposed by Bromage et al. (2003). To achieve quantitative information about the birefringence, a model tissue of mineralized turkey leg tendon containing longitudinally arranged mineralized collagen fibers was cut at five angles with respect to its main axis and imaged with polarized light. A calibration curve, taking into account sample thickness, wavelength of the light and non-linear relationship of birefringence and out-of-plane fiber angle, was proposed based on the readings on MTLT. The calibration curve was than used on human femur secondary osteons.

3.3 Methods

3.3.1 Samples

MTLT was used as a model for calibration of the birefringence. This tissue is composed of mineralized collagen fibers - similar in constitution to bone, but with much simpler, uniform arrangement, approximately parallel to the main axis of the tendon. MTLT shows two different morphologies, one highly mineralized and very porous and one with low porosity, densely packed collagen fibers and mineralization similar to that of human cortex. The phase more similar to bone in composition and morphology was chosen for the calibration purposes, as the volume fraction of collagen fibrils, as well as, nanoporosity might affect the observed birefringence (Bromage et al., 2003).

For the calibration, 35 fully mineralized MTLT samples were embedded in epoxy resin. Each sample was cut at five different angles to the tendons main axis 0, 30, 45, 60 and 90 $(\pm 5)^o$ (Fig. 3.1) and mounted to glass slides to obtain an uniform section thickness. All sections were polished to the thickness of approximately 30-60 (± 5) μm and thickness was recorded with a microscope with a calibrated precision stage in the z direction. Normalization of the the readings for sample thickness was necessary to make the calibration universally applicable, while other investigators had to ensure an uniform sample thicknesses in order to make inter-specimen comparisons (Bromage et al., 2003).

Additionally, thin slices of seven mid-shaft human femur samples were prepared with the same protocol as the MTLT samples. Birefringence was measured in about 200 regions of interest. The obtained calibration curve was applied to transform the $|\sin(\delta)|$ readings into the out of plane collagen angle. The collagen arrangement in about 300 osteons was quantitatively assessed.

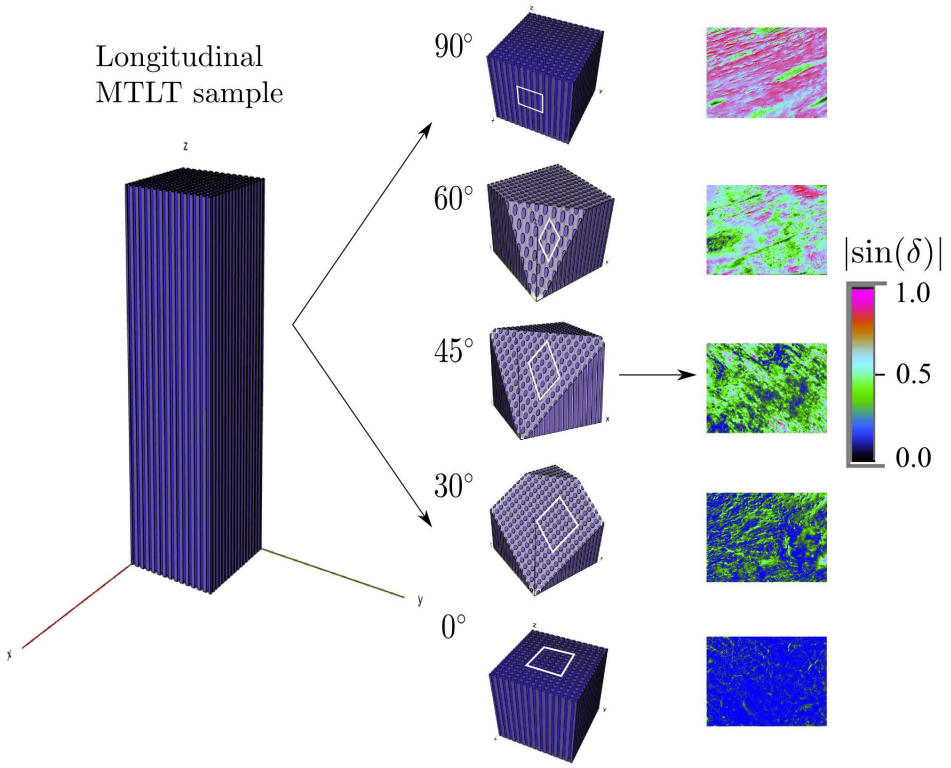

Figure 3.1: Samples extraction scheme and the resulting $|\sin(\delta)|$ false-colored images.

3.3.2 Birefringence measurements

An automated technique was applied, based on the rotating polarizer method to unfold quantitatively birefringence, eigenmodes and absorption, where an object is simultaneously imaged at four different polarizer angles in a single image implementing an image multiplexer (Quadview, MAG Biosystems)(Kaminsky et al., 2007). In this way the noise contributions coming from camera drifts, fluctuations of light source and mechanical instabilities of the optical system set-up are minimized (Kaminsky et al., 2007). The system used consisted of a microscope for polarized light, interference filter and broadband quarter-wave retarder to produce incident circular polarized light, as well as the image multiplexer and a CCD camera. Background correction was performed to ensure uniform illumination of the whole field of view in the microscope. The image multiplexer used here contained four polarizers placed at 0, 45, 90, 135^o with respect to a horizontal reference, allowing the incident circularly polarized light to go through a sample to the four polarizers simultaneously. The birefringence is measured as a sinusoidal

function:

$$\Delta \mathrm{n_s} \approx (\mathrm{n_e} - \mathrm{n_o}) \sin^2\theta, \tag{3.1}$$

where Δn_s is the birefringence, n_e and n_o are the refractive indices in the direction of extraordinary and ordinary rays, respectively, and θ is the angle which the wave normal **s** makes with the z-axis, which is related to the MTLT fibers and defines the out-of-plane angle of the z-axis (see the Appendix for the derivation of the formula).

The phase difference δ between the two light paths (two rays travelling with different velocities - subject to different refractive indices n_o, n_e), after the recombination of the rays is a measure of the optical anisotropy of the material (Pajdzik and M., 2006). The phase difference is given by:

$$\delta = \frac{2\pi \Delta \mathrm{n_s} \mathrm{L}}{\lambda}, \tag{3.2}$$

with L - sample thickness, λ - wavelength of the light. Replacing Δn_s with equation 3.16 we obtain:

$$\delta = \frac{2\pi(\mathrm{n_e} - \mathrm{n_o})\mathrm{L}}{\lambda} \sin^2\theta. \tag{3.3}$$

In the false colored images the red pixel readings correlate linearly to $|\sin(\delta)|$. The two morphology zones of MTLT were segmented based on the intensity images. The zone more similar to cortical bone was used for the calibration purposes quantifying the average birefringence of this zone within each image. Pores were also segmented based on the intensity images (Goldman et al., 2003). The fringe-order of the sinusoidal function in Eq. 3.3 is ambiguous (unless relatively low birefringence is observed), but can be resolved with multiwavelength measurement (Geday et al., 2000). In this study measurements of the $|\sin(\delta)|$ were performed at 550nm and 600nm and the ambiguity elimination procedure described in Geday et al. (2000) was applied.

Solving Eq. 3.3 for the angle which the wave normal **s** makes with the optical axis θ introduced into the uniaxial MTLT samples by special angled cuts (see Fig. 3.1) leads to:

$$\theta = \arcsin\sqrt{\mathrm{c}\frac{\delta}{\mathrm{L}}}, \tag{3.4}$$

with the calibration factor c:

$$\mathrm{c} = \frac{\mathrm{L}}{\delta}\sin^2\theta = \frac{\lambda}{2\pi(\mathrm{n_e} - \mathrm{n_o})}. \tag{3.5}$$

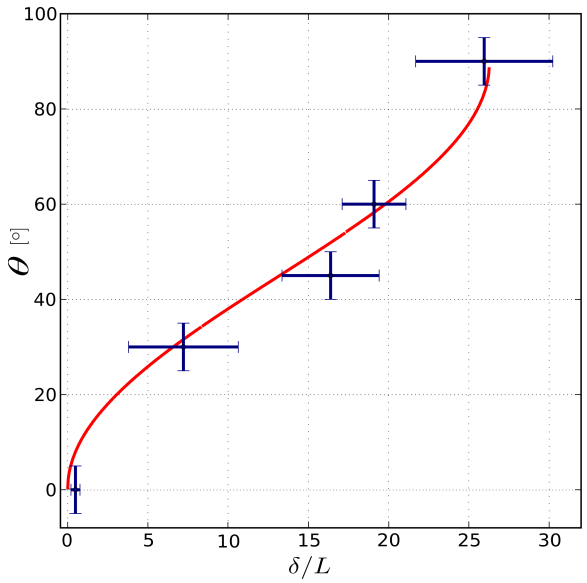

Figure 3.2: Calibration curve describing relationship between the collagen out-of-plane fibers angle θ and the measured phase factor δ. Errorbars in the δ/L represent one standard deviation. Sample cut angles θ were accurate within about 5^o.

3.4 Results

Mean values of thickness normalized $|\sin(\delta)|$ readings were calculated for each region of interest in an acquired image. The ambiguity in the phase measurements was solved using two wavelength measurements. Pixels showing $|\sin(\delta)|$ from other than the first fringe were discarded in the calibration procedure (Pajdzik and M., 2006). The calibration factor c was determined from Eq. 3.5 to 0.038. The resulting calibration curve is shown in Fig. 3.2.

Application to human midshaft osteons The dependency between $|\sin(\delta)|$ and out-of-plane collagen arrangement angle θ calibrated on MTLT was applied in osteonal bone (see Fig. 3.3).

The average out-of-plane collagen angle measured on the midshaft sections of human femurs was 25.8^o with standard deviation of 1.3^o.

Exemplary results are shown in Figure 3.3. Different types of osteons were visible, for example osteons with frequently changing collagen arrangement angle between adjacent lamellae (Fig. 3.3a), called the distributed osteons by Martin et al. (1996). On the other hand, in some osteons the changes were not so frequent (Fig. 3.3d), with groups of a few lamellae arranged in similar directions next to a few with another one (called hoop

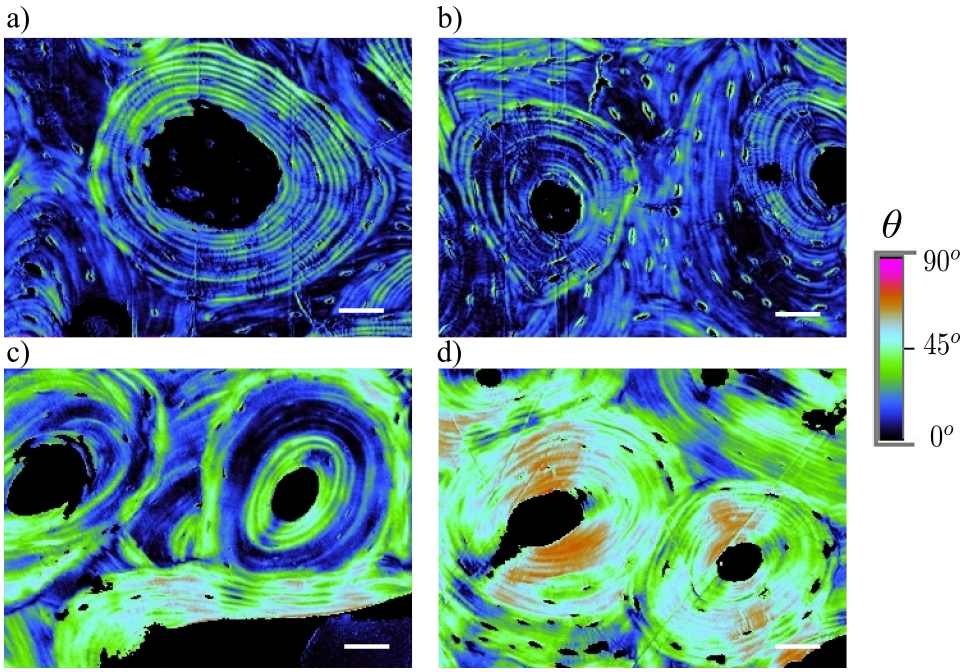

Figure 3.3: Collagen out-of-plane angles θ evaluated using the calibration curve on a mid-shaft of human femur. Bar 100μm.

osteons in Martin's scale). Some osteons showed very little changes in collagen arrangement (Fig. 3.3b), alternatively dark osteons.

An additionally altered collagen arrangement was observed in vicinity of osteocytes (Fig. 3.3b), exhibiting more of the circumferential type of tissue (Fig. 3.3c), where the collagen fibers, showing higher birefringence, were arranged longitudinally.

3.5 Discussion

In this study a technique allowing for quantitative assessment of birefringence was calibrated for universal use in mineralized tissues. We believe this is a promising attempt for quantification of collagen fiber arrangement in cortical bone, which is a curtail parameter in many models and can improve our general understanding of the principles underlying the exceptional mechanical properties of bone.

The average collagen orientation observed on seven samples of human femur was about 26^o, which is in good agreement with the observations made by Turner et al. (1995) from acoustic microscopy showing a "principal orientation" of collagen at $\sim 30^o$ to the long axis of bone. The acoustic microscope used for the study allowed for a depth resolution of 60μm. The

output of the quantitative light microscopy technique we are introducing here gives the average over the sample thickness seen in transmission at sample thickness of 30-60μm (resolution in the z direction) which allows for a direct comparison to the acoustic microscopic study, but is in general a limitation of the spatial resolution that can be obtained with the technique. Additionally the study by Turner et al. (1995) showed a misalignment of mineral (that was on average oriented along the long axis of bone) and collagen. The result was interpreted as the contribution of the extrafibrillar mineral, as the interfibrillar mineral is rather well aligned with the collagen fibrils (Gupta et al., 2005; Olszta et al., 2007; Balooch et al., 2008).

According to Weiner et al. (1999) each lamella is composed of 5 sublayers with collagen fibers rotating progressively about 30^o in each. For the sublayers thicknesses presented in that work, the maximum stiffness of such a lamella was predicted in the direction of 12.6^o out of plane by Reisinger et al. (2010). Osteons containing lamellae with a similar average collagen arrangement were observed frequently (example in Figure 3.3b).

Wagermaier et al. (2006) resolved a local crystallite orientation of several osteons of human midshaft femur using scanning x-ray diffraction with a micron-sized synchrotron beam (SAXS/WAXD). The variation of the out-of-plane arrangement of mineral crystallites was 10-60^o to the osteon axis and was decreasing with the distance from the Haversian channel. If the arrangement of collagen fibers is assumed to be compliant with the arrangement of the c axis of the mineral platelets (Gupta et al., 2005), this could be compared to our results, with the caveat of a potential dependency on the mineral distribution between collagen fibrils and extrafibrillar matrix, as mentioned above (Turner et al., 1995). The average orientation measured with the x-ray diffraction was 30^o, similar to what was measured by Turner (Turner et al., 1995) and our results. Wagermaier et al. suggested a 3D helicoidal arrangement of the fibrils around the Haversial channel, since the angles measured were varying within one quadrant. The main advantage of such structures is their higher extensibility in tension and compression, compared to an orthogonal plywood structures (Wagermaier et al., 2006). Anisotropy of a structure with this arrangement is in agreement with the anisotropy predicted by Reisinger et al. (2010) to be about 1.13 ($\pm$ 0.07) for an osteon composed as described by Wagermaier et al. (2006). This fits reasonably to the measured ratio of 1.25 ($\pm$ 0.18) (Franzoso and Zysset, 2009), supporting the helicoidal structure hypothesis in its mechanical implications.

The advantage of using the technique proposed here, over for example SAXS/WAXS techniques, is the possibility of obtaining quantitative information about the collagen fibers arrangement of relatively large regions of the tissue in short experiment time. The limitations of the technique are: the need of thin samples preparation (and control of the thickness) and the fact that volume fraction of the tissue and its degree of mineralization might

influence the results. Multiwavelength measurements are required to resolve periodicity ambiguity of the $|\sin(\delta)|$ function. Additionally, slight artifacts were observed in some of the osteon images that manifested in asymmetry of the birefringence readings (as for example in Fig. 3 d). Because there is no overall preferred direction common to all images we can conclude that the set-up of polarizing components did not introduce any such artifacts but that they are typical for the samples measured and may indicate background effects from the sample preparation which involved polymers. The effect was taken care in the data analysis by averaging over many samples.

As a validation of the accuracy of the collagen arrangement measurements, spectroscopic (IR and Raman) studies on the angled MTLT samples are planned. Our approach could be extended to other (bio-)materials with birefringent fibers. Further investigations of the collagen out-of-plane angle dependent on physiological location, age, gender and other factors are planned on secondary and primary osteons, as well as, on trabecular bone. Additionally, a combination of the out-of-plane collagen arrangement with the in-plane arrangement assessment that can be as well resolved with polarized light is planned.

3.6 Acknowledgments

This research was supported by grant no P19009-N20 of the Austrian Science Foundation (FWF). Authors would like to thank Andreas Reisinger for programing the fibril visualization script used for producing Fig. 3.1 and Thomas Tangl for help with samples preparation.

3.7 Appendix: Derivation of the calibration formula

The propagation of energy in crystals is described in detail in for example Born and Wolf (1999). The theory of optical anisotropy will be shortly sketched in this section. In a crystal, the energy density U of a wave front is expressed in terms of the electric field $\mathbf{E}$ of the wave and the dielectric displacement $\mathbf{D} = \varepsilon\mathbf{E}$:

$$\mathrm{U} = \frac{1}{2}\mathbf{E} \cdot \mathbf{D}, \tag{3.6}$$

where the dielectric tensor ε is of second rank and can be diagonalized. When choosing the orthogonal eigenvectors of ε as reference, with eigenvalues ε_x, ε_y, ε_z and denoting with ε the effective dielectric constant with which the light wave propagates along unit vector $\mathbf{s}$ through the sample, than Eq. 3.6 can be written as:

$$\frac{D^2}{\varepsilon} = 2\mathrm{U} = \frac{D_x^2}{\varepsilon_x} + \frac{D_y^2}{\varepsilon_y} + \frac{D_z^2}{\varepsilon_z}. \tag{3.7}$$

With $\mathrm{D}^2 = D^2(s_x^2 + s_y^2 + s_z^2)$ follows

$$\frac{s_x^2}{\varepsilon - \varepsilon_x} + \frac{s_y^2}{\varepsilon - \varepsilon_y} + \frac{s_z^2}{\varepsilon - \varepsilon_z} = 0. \tag{3.8}$$

In this study we assume the uniaxial fiber structure of MTLT is also an optically uniaxial crystal with the optic axis in the z direction, so $\varepsilon_x = \varepsilon_y$. Further we take notation: $\varepsilon_x = \varepsilon_y = \varepsilon_o$, $\varepsilon_z = \varepsilon_e$, where suffixes o and e stand for ordinary and extraordinary. With this notation, the Eq. 3.8 reduces to:

$$(\varepsilon - \varepsilon_\mathrm{o})[(\mathrm{s_x^2} + \mathrm{s_y^2})(\varepsilon - \varepsilon_\mathrm{e}) + \mathrm{s_z^2}(\varepsilon - \varepsilon_\mathrm{o})] = 0. \tag{3.9}$$

Let θ denote the angle which the wave normal $\mathbf{s}$ makes with the z-axis, than:

$$\mathrm{s_x^2} + \mathrm{s_y^2} = \sin^2\theta, \tag{3.10}$$

$$\mathrm{s_z^2} = \cos^2\theta. \tag{3.11}$$

Substituting $(s_x^2 + s_y^2)$ and s_z^2 in equation 3.9 we obtain:

$$(\varepsilon - \varepsilon_\mathrm{o})[(\varepsilon - \varepsilon_\mathrm{e})\sin^2\theta + (\varepsilon - \varepsilon_\mathrm{o})\cos^2\theta] = 0. \tag{3.12}$$

This equation has two roots defining the two possible effective dielectric constants $\varepsilon^{'}, \varepsilon^{''}$ for a given propagation direction to:

$$\begin{cases} \varepsilon^{'} = \varepsilon_o \\ \varepsilon^{''} = \varepsilon_o^2 cos\theta + \varepsilon_e sin^2\theta. \end{cases} \tag{3.13}$$

With the relation $n^2 = \varepsilon$, with n - average refractive index we derive:

$$\varepsilon^{''} - \varepsilon^{'} = (\varepsilon_\mathrm{e} - \varepsilon_\mathrm{o})\sin^2\theta = \mathrm{n}^{''2} - \mathrm{n}^{'2}. \tag{3.14}$$

For small quantities of n we could write:

$$\mathrm{n}^{''2} - \mathrm{n}^{'2} \approx \frac{1}{2\mathrm{n}}(\mathrm{n}^{''} - \mathrm{n}^{'}), n_e^2 - n_o^2 \approx \frac{1}{2n}(n_e - n_o), \tag{3.15}$$

to derive the birefringence $\Delta n_s = (n^{''} - n^{'})$ approximately as:

$$\Delta\mathrm{n_s} \approx (\mathrm{n_e} - \mathrm{n_o})\sin^2\theta. \tag{3.16}$$

Chapter 4

Indentation

Based on manuscript:
"Elastic anisotropy of uniaxial mineralized collagen fibers measured using two-directional indentation. Effects of hydration state and indentation depth."
By Ewa M. Spiesz, Paul Roschger and Philippe K. Zysset
Submitted to Journal of the Mechanical Behavior of Biomedical Materials, 2011.

4.1 Abstract

Mineralized turkey leg tendon (MTLT) is an attractive model of mineralized collagen fibers, which are also present in bone. Its longitudinal structure is advantageous for the relative simplicity in modeling, but its anisotropic elastic properties remain unknown. The aim of this study was to quantify the extent of elastic anisotropy of mineralized collagen fibers using nano- and microindentation in two orthogonal directions of the same MTLT samples. Large number of measurement points allow for quantification of the extent of anisotropy, depending on the final indentation depth and on the hydration state of the sample. Anisotropy was increasing with the sample re-hydration process. In fact, artifacts of indentation in the transverse direction to the main axis of the mineralized tendons in re-hydrated condition were observed. The indentation size effect - increase of the measured elastic properties with decreasing sampling volume, reported previously on variety of materials, was also observed in MTLT. Indentation work was quantified for both directions of indentation in dried and re-hydrated conditions. As hypothesized, MTLT showed a higher extent of anisotropy compared to cortical and trabecular bone, presumably due to the alignment of mineralized collagen fibers in this tissue.

4.2 Introduction

The mineralized turkey leg tendon is a tissue containing longitudinally arranged collagen fibers that normally mineralize over time, which makes them attractive models to study mechanisms of mineralization (Landis et al., 1996; Landis and Silver, 2002). The tendons undergo a gradual mineralization from a point mid-way along the tendon in the proximal direction, giving possibilities to study different stages of the process, depending on the distance from the mineralization front. Constituents of MTLT are similar to those of bone, being mainly collagen, of which 90% is the type I (Landis and Silver, 2002; Fritsch and Hellmich, 2007), hydroxyapatite and water. Mineral content of tendons of 24 weeks old animals was reported to be slightly lower than this of human bone (Gupta et al., 2004) and within bone mineralization level for tendons extracted from older turkeys (Spiesz et al., 2011b).

Two distinct morphologies of MTLT are shown in Fig. 4.1. One consists of densely packed mineralized collagen fibers and is placed around large pores of the tendon (blood vessels) and was called circumferential zone. The other, present in between of the large pores, with more sparse structure and higher microporosity was called the interstitial zone (Spiesz et al., 2011b). The zones were shown to have slightly different composition on top of the different morphology and were therefore treated separately in this study.

Indentation is a technique used for quantifying the elastic properties of inhomogeneous materials at the micro- and nanolevel. Indentation could be considered as a non-destructive technique that often does not require complicated sample preparation or mounting and can be performed multiple times on the same sample. In this technique indentation modulus of rate-independent, elasto-plastic materials can be evaluated based on elastic contact theory (Oliver and Pharr, 1992; Fischer-Cripps, 2002; Oyen, 2011). For bulk isotropic materials, the indentation modulus is directly related to elastic modulus and Poisson's ratio (Oliver and Pharr, 1992; Rho et al., 1999; Ebenstein and Pruitt, 2006). For anisotropic and/or more complex material systems, like bone or MTLT, indentation modulus is related to the stiffness tensor with a more complex function (Swadener and Pharr, 2001), but can be estimated using iterative schemes (Franzoso and Zysset, 2009). Many nano- and microindentation results of mineralized tissues available so far, were obtained in dried state. Due to the important role of hydration in collagen properties, nanoindentation in physiological conditions is gaining acceptance (Hengsberger et al., 2002b; Wolfram et al., 2010b). This is important in order to simulate conditions closer to the in vivo state, as hydrated tissues swell, changing the elastic properties. In trabecular bone, the stiffness anisotropy is changing with re-hydration (Wolfram et al., 2010b), which suggests the volume changes are anisotropic, which was also seen macroscopically on MTLT (Lees and Page, 1992).

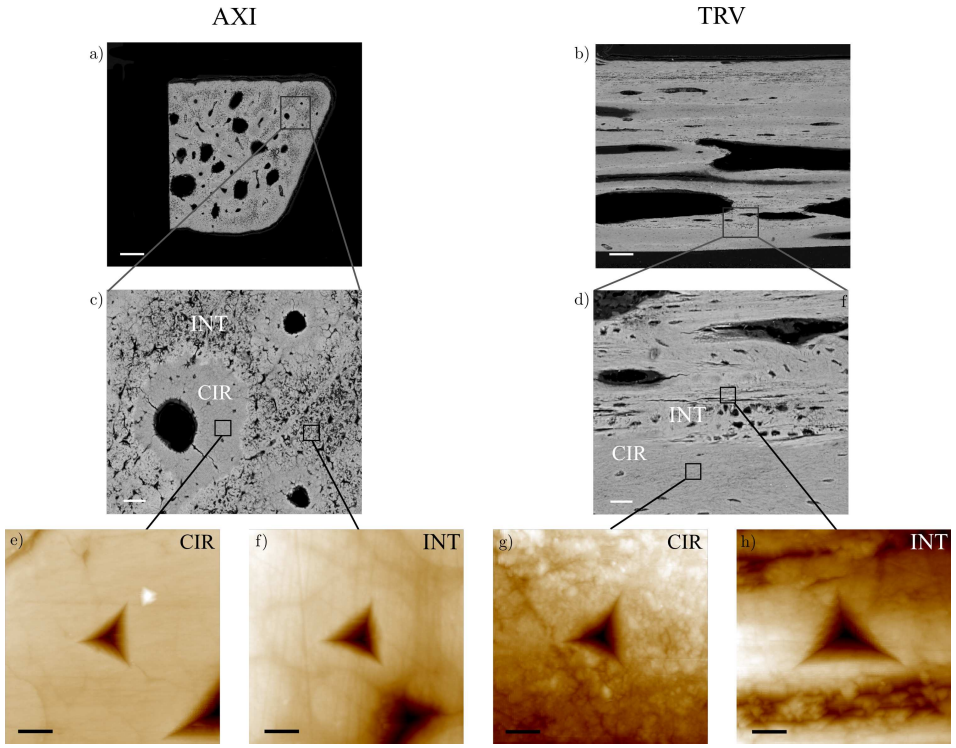

Figure 4.1: Circumferential (CIR) and interstitial (INT) zones of MTLT in two orthogonaldirections (axial - AXI and transverse - TRV) as seen by backscattered electron imaging (a-d) and scanning probe microscopy (e-f). a, b) Bar - 50 μm; c, d) Bar - 25 μm; e, f) Bar - 5 μm.

The measurement of indentation modulus should, according to the conventional plasticity theory, be independent of indentation depth, but the so called indentation size effect, which describes the increase of indentation modulus with decreasing sampling volume, was reported before (Swadener and Pharr, 2001; Zhang et al., 2008; Voyiadjis and Peters, 2010). This issue is not yet resolved quantitatively, even though some modeling attempts were done (Begley and Hutchinson, 1998; Shu and Fleck, 1998).

The aim of the study was to measure elastic properties of mineralized turkey leg tendons in two orthogonal directions. Availability of such a set of data is limited in the literature, to the authors knowledge, but is very useful for the attempts to understand mechanical behavior of uniaxial mineralized collagen fibril arrays (Reisinger et al., 2010). Effects of sample re-hydration on the measured indentation modulus in the two directions were also investigated. Two hierarchical levels of the tissue organization were investigated using nano- and microindentation, contributing to the knowledge about the indentation size effects observed in mineralized tissues.

4.3 Materials and Methods

4.3.1 Samples

Highly mineralized parts of ten digital flexor tendons of domestic turkeys (Bigi et al., 1996; Lees et al., 1994; Gupta et al., 2004) older than 24 weeks were used in this study. ∼10 mm long specimens (about 40-60% of the hard, highly mineralized part of a tendon), extracted from 8 legs, were used. Sections of the two orthogonal directions of each sample, involving one transverse sample of approximately 10 mm in length and four axial samples taken from the vicinity of the longitudinal one, were prepared as shown in Figure 4.2. A total of 49 tendon sections (one axial section was destroyed during processing) were embedded in epoxy resin (EpoFix, Struers, Ballerup, Denmark) without dehydration of the sample or resin infiltration, which allows subsequent rehydration for indentation. The specimens were mounted to glass slides and polished using silicon carbide papers series and a 1μm diamond suspension on a polishing cloth with a semi-automatic polishing machine (PM5, Logitech, UK). Similar procedure was successfully used for bone sections preparation for indentation (Wolfram et al., 2010a,b). Two morphological zones present in MTLT (Spiesz et al., 2011b), the circumferential and the interstitial were separated in the identification of regions of interest for indentation. Mineralization within a morphology zone resulting from quantitative backscattered electron imaging was homogenous. Interstitial zone showed higer porosity than the circumferential one (Spiesz et al., 2011b).

4.3.2 Morphological analyzes

Morphology was observed using two imaging techniques: quantitative backscattered electron imaging (qBEI) and scanning probe microscopy mode of the indenter. qBEI images were captured using digital scanning electron microscope with a fourquadrant semiconductor backscattered electron detector (DSM 962, Zeiss), at a working distance of 15 mm. Probe current was adjusted to 110 ± 0,4 pA and electron beam energy used was 20 keV (Roschger et al., 1998). Images with magnification of 50 and 400x were captured which resulted in imaged areas of approximately 2.0×2.5mm and 250×315μm, respectively (see Fig.4.1). The regions were chosen randomly making sure that both types of morphology are visible in each image. Additionally, topography scans were obtained using the Hysitron Triboindenter with a Berkovich tip, the same as the one used for indentation (see 4.3.3) with a scan rate of 0.3 Hz.

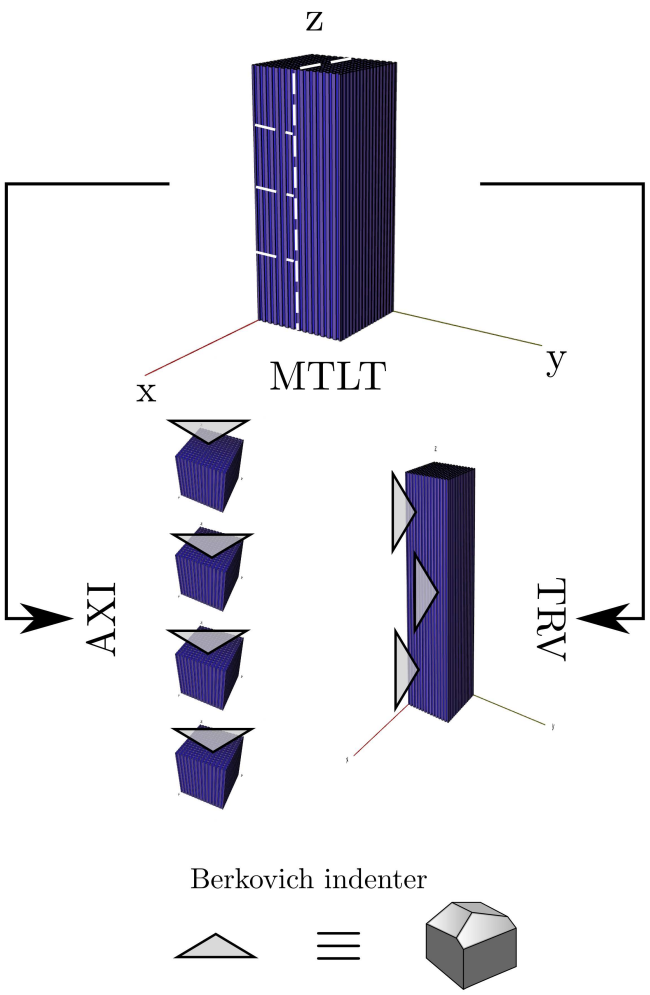

Figure 4.2: MTLT two-directional sample extraction scheme resulting in axial (AXI) and transverse samples (TRV). MTLT is schematically represented as mineralized collagen fibers arranged longitudinally along the tendons main axis (z).

4.3.3 Indentation

Selection of regions of interest

Regions of interest for indentation were selected within the tissue previously imaged with qBEI. In each section of a tendon 6-10 400x qBEI images containing both circumferential and interstitial zone were taken, defining the regions of interest for indentation. In each of those 30-60 single indents were placed using a light microscope of the indenter to avoid lacunae, micropores or surface preparation defects. Over 3000 indentations with 2500nm (dried

and physiological conditions of indentation) and over 2000 of indents of approximately 900-1000nm in depth (dried conditions) were performed in site matched zones of the 49 specimens.

Indentation protocol

MTLT was considered a linear viscoelastic material in small strain, based on previous macroscopic tensile tests (unpublished data) and the similarity of mineralization to bone. Indentations were performed in both dried and physiological conditions to evaluate re-hydration effects on MTLT's stiffness. Two machines were used: the Nano-Hardness Tester, CSM Instruments, Peseux, Switzerland (for microindentation) and the TriboIndenter, Hysitron, USA (for nanoindentation). In this study MTLT samples were indented in two orthogonal directions (axial and transverse) to the main axis of a tendon. Microindentation in physiological conditions was performed in specially designed fluid cell, using Hank's Balanced Salts Solution (HBSS; VWR, Vienna, Austria) as re-hydration medium. Samples were re-hydrated for at least 1 hour before indentation. Berkovich indenter was used and measurements were conducted in a load control. Time dependence was not in focus of this study, so a homogeneous loading rate was used in all indentations. MTLT was considered to have a no more rate-dependent behavior than other mineralized tissues on which nano- and microindentations were successfully performed (Ebenstein and Pruitt, 2006; Oyen, 2006). Indentation protocol involved trapezoidal loading/unloading with constant rate of 120mN/s with 60 seconds holding time at maximum load to minimize the viscoelastic and/or viscoplastic effects. In microindentation this load controlled protocol was performed until the displacement limit of 2500nm and in nanoindentation until the load limit of 9000μN. Indentation moduli were calculated according to Oliver and Pharr (1992).

Statistical analyzes

All indents close to scratches or other surface defects (including pores) were discarded. Earlier studies on mineralization of the two zones of morphology proved low heterogeneity of mineralization within a zone (Spiesz et al., 2011b), which allowed for defining additional statistical outliers as values higher than 1.5 times the interquartile range above the third quartile and below the first quartile (Crawley, 2005). Welch two tailed t-test (Crawley, 2005) was used for comparison of the groups and the differences were shown using the box and whisker plots that represent the sample medians (horizontal bar) and the top/bottom border of the box represents the interquartile range. Whiskers represent maximum/minimum value (after removal of the outliers). This representation of the data has the advantage of showing the nature of variation in the results and skewness of the distribution (Crawley,

2005), rather than showing the means and standard deviations. Significance level of $\alpha = 0.05$ was used in this study.

Indentation work

The work of indentation was calculated for the microindentation experiments. Application of the force to the indenter and the resulting displacement represents the work done on the system and is manifested as plastic and elastic strains in the specimen (Fischer-Cripps, 2002). During unloading, energy is released by the material. The area enclosed by the loading and unloading curve represents the energy lost in plastic deformation (plastic work). The elastic energy stored was evaluated by integration of the area under the unloading curve, until the end of the holding phase (elastic work).

Stiffness tensors estimation

An iterative scheme proposed by Franzoso and Zysset (2009) was used to estimate a stiffness tensor based on indentation moduli in two orthogonal directions. The scheme is based on a procedure inverse to the one proposed by Swadener and Pharr (2001), which allows calculation of the indentation moduli in a given direction knowing the material's stiffness tensor.

4.4 Results

4.4.1 Microindentation in dried and physiological conditions

A higher indentation modulus was measured in circumferential zone, as compared to interstitial one, using microindentation in axial and transverse directions (see Tab. 4.1).

Higher anisotropy extent (${}^{ind}E_{axi}/{}^{ind}E_{trv}$) was measured in the circumferential zone, than in the interstitial one, see Table. 4.1.

Significant differences of indentation moduli in dried and physiological conditions, in both axial and transverse directions were found when the circumferential and interstitial zones were treated separately, (p-values below 0.005, see Fig. 4.3). Similarly as for trabecular bone (Wolfram et al., 2010a), re-hydration of the MTLT diminishes the indentation modulus in two orthogonal directions and in both morphology zones.

On average the indentation modulus decreased by 5.4% in physiological conditions with respect to the dried ones, when measured in axial direction. In transverse direction the avaraged measured stiffness decrease was 55.6%, but is likely overestimated due to swelling artefacts.

Total work, as well as, the plastic and elastic work of microindentation, were calculated for measurements in dried and physiological conditions and showed similar trends as indentation moduli for the same cases. Plastic work is shown in Fig. 4.4 a, as an example.

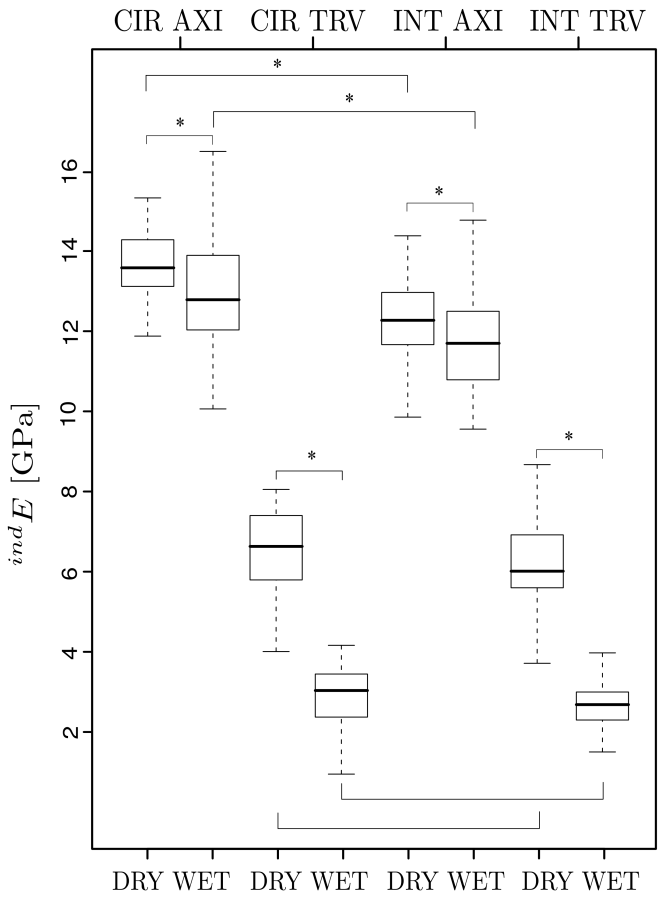

Figure 4.3: Re-hydration effects on microindentation moduli evaluated separately in the two morphology zones circumferential (CIR) and interstitial (INT). Indentation moduli were measured in dried (DRY) and re-hydrated conditions (WET), in the two orthogonal directions (AXI, TRV). The level of significance noted in the figure (*) is $p < 0.05$. The horizontal solid bars represent medians, the top/bottom border of the box represents the interquartile range. Whiskers represent maximum/minimum value.

Ratios of the elastic over plastic work (W_{el}/Wpl) representing the fraction of elastic and dissipated energy were calculated to ensure the work is independent of the maximal load used in indentation, see Fig. 4.4 b. Higher ratios were observed in the transverse direction of indentation (0.40 and 0.53 in dried and re-hydrated conditions, respectively), than in the axial one (0.23 and 0.18 in dried and re-hydrated conditions).

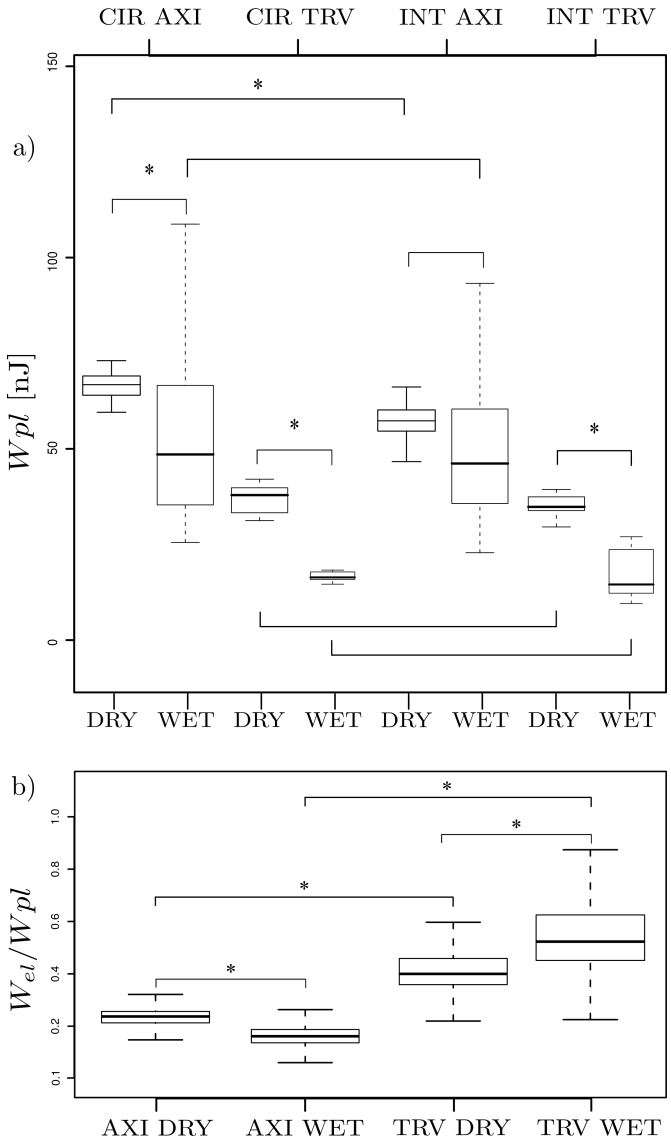

Figure 4.4: a) Microindentation plastic work (W_{pl}) measured in dried (DRY) and re-hydrated (WET) conditions, in the two orthogonal directions (AXI, TRV), in the two morphology zones (CIR, INT), b) ratio of elastic to plastic work (W_{el}/Wpl). The level of significance noted in the figure (*) is $p < 0.05$. The horizontal solid bars represent medians, the top/bottom border of the box represents the interquartile range. Whiskers represent maximum/minimum value.

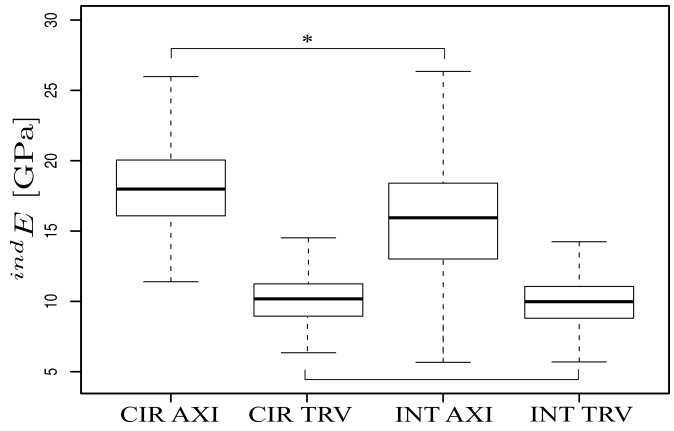

Figure 4.5: Nanoindentation results in the two morphology zones (CIR, INT), dry indentation in two directions (AXI, TRV). The level of significance noted in the figure (*) is $p < 10^{-6}$. The horizontal solid bars represent medians, the top/bottom border of the box represents the interquartile range. Whiskers represent maximum/minimum value.

4.4.2 Nanoindentation in dried conditions

Indents with the final depth of 900-1000 nm were performed on the same samples and in the same regions of interest, for comparison with the results of microindentation in dried conditions. In nanoindentation, similarly to the microindentation, circumferential zone was stiffer in axial and transverse direction, than the interstitial zone, see Tab. 4.1. The stiffness of the two zones is significantly different in the axial direction of indentation ($p < 10^{-6}$). The differences are not significant in the transverse direction (see Fig. 4.5).

The indentations were performed in load control, and were resulting in different final indentation depths (depending on the local stiffness of the tested area). The average final indentation depth (h_{max}) in axial direction of indentation was higher for the interstitial zone (990 ± 138 nm), than in the circumferential one (916 ± 64 nm). The final indentation depths were higher in the transverse direction of the indentation as compared to the axial directions. The final depth in the interstitial zone was again higher (1205 ± 155 nm), than in the circumferential one (1109 ± 79 nm).

4.4.3 Comparison between nano- and microindentation results

Indentation moduli measured with nanoindentation are higher than the ones measured with microindentation (see Table 4.1). The anisotropy extent measured with nanoindentation was lower compared to the one measured

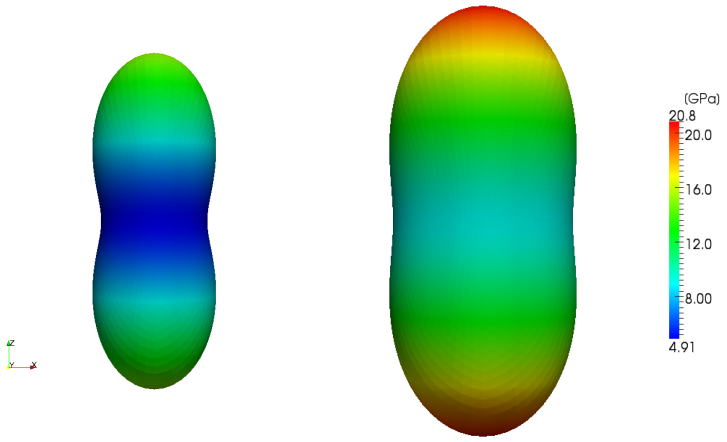

Figure 4.6: Transverse-isotropic stiffness tensors estimated from the average indentation moduli in two orthogonal directions for the dried conditions micro- and nanoindentation in MTLT (fibers arranged along the z-axis, vertically).

with microindentation in the same regions of interest as mentioned before, see Tab. 4.1. Circumferential zone of MTLT showed higher anisotropy compared to the interstitial one, both in nano- and microindentation, as well as, in dried and re-hydrated conditions of microindentation.

Stiffness tensors of MTLT were computed from micro- and nanoindentation results in dried state, taking the average of all indents in the given indentation direction (see Figure 4.6). The following transverse-isotropic stiffness tensors were estimated for MTLT from:
a) microindentation in two directions:

$$[\mathbb{S}] = \begin{bmatrix} 7.02 & 3.30 & 5.87 & 0 & 0 & 0 \\ 3.30 & 7.02 & 5.87 & 0 & 0 & 0 \\ 5.87 & 5.87 & 22.17 & 0 & 0 & 0 \\ 0 & 0 & 0 & 6.60 & 0 & 0 \\ 0 & 0 & 0 & 0 & 6.60 & 0 \\ 0 & 0 & 0 & 0 & 0 & 3.72 \end{bmatrix}$$

Anisotropy extent $\frac{^{ind}E_{axi}}{^{ind}E_{trv}}$	Microindentation		Nanoindentation
	WET	DRY	DRY
CIR	$\frac{12.85(\pm1.57)}{2.85(\pm0.93)} = 4.50$	$\frac{13.68(\pm0.83)}{6.51(\pm1.03)} = 2.10$	$\frac{18.09(\pm2.86)}{10.16(\pm1.81)} = 1.78$
INT	$\frac{11.60(\pm1.22)}{2.76(\pm0.77)} = 4.20$	$\frac{12.18(\pm1.05)}{6.14(\pm1.08)} = 1.99$	$\frac{15.68(\pm3.86)}{9.92(\pm1.59)} = 1.60$

Table 4.1: Extent of anisotropy measured with nano- and microindentation in two orthogonal directions, in dried (DRY) and re-hydrated (WET) conditions. Average indentation moduli in axial ($^{ind}E_{axi}$) and transverse direction ($^{ind}E_{trv}$), as well as standard deviations (in brackets), are given in GPa. CIR stands for the circumferential and INT for the interstitial zone.

b) nanoindentation in two directions:

$$[\mathbb{S}] = \begin{bmatrix} 12.91 & 6.08 & 9.23 & 0 & 0 & 0 \\ 6.08 & 12.91 & 9.23 & 0 & 0 & 0 \\ 9.23 & 9.23 & 29.82 & 0 & 0 & 0 \\ 0 & 0 & 0 & 10.39 & 0 & 0 \\ 0 & 0 & 0 & 0 & 10.39 & 0 \\ 0 & 0 & 0 & 0 & 0 & 6.84 \end{bmatrix}$$

4.5 Discussion

The goal of the study was to quantify the extent of elastic anisotropy in MTLT using two-directional indentation. It was assumed that the anisotropy in this tissue would be higher than the one measured in bone, because of the simple, uniaxial arrangement of the mineralized collagen fibers. In cortical and trabecular bone the fibers arrangement is much more complex ranging on average anisotropy extent lower than the one seen in MTLT. Franzoso and Zysset (2009) measured the extent of anisotropy of human cortical bone using nanoindentation in dried state, which resulted in an average $^{ind}E_{axi}/^{ind}E_{trv} = 1.43$. Wolfram et al. (2010b) found lower anisotropy in trabecular bone (1.40 measured with microindentation in re-hydrated and 1.19 in dried state). The anisotropy in MTLT was the highest among those mineralized tissues (see Tab. 4.1). Similarly the elasticity anisotropy ratio obtained with acoustic microscopy Lees and Page (1992) was 1.96 - higher than the anisotropy in bone and within the range measured in this study for dried specimens.

The elastic anisotropy extent of a mineralized collagen fibril array was also predicted with a mean field micromechanical homogenization scheme

by Reisinger et al. (2010). The mineralized collagen fibrils were aligned in an uniaxial manner in arrays, similar to MTLT. The extent of anisotropy quantified by a ratio of indentation moduli in axial and transverse directions was in the range of 1.5 - 2.0, depending on the overall mineralization of the array and stiffness of collagen used in the simulation. This fits with the range measured using indentation in dried conditions (see Tab. 4.1).

The anisotropy ratio measured in re-hydrated conditions was outside of the range predicted by the simulations (4.20 - 4.50), which may be caused by the highly reduced values of indentation modulus measured in the transverse direction. The stiffness changes in physiological conditions in this direction of indentation are larger than the expected changes in vivo, and may be caused by excessive bulging of the sample surface in this direction. The swelling in MTLT was reported to be highly anisotropic in the macroscopic level (Lees and Page, 1992), which is confirmed here in the microscopic scale. Microindentation moduli in transverse direction of MTLT in re-hydrated state are on average 55.6% lower than the results obtained in dried state. This appears to be due to an artifact coming from swelling of the cut tissue sufraces where the fibers are not constrained. In this study a swell of about 15-20 μm in the transverse samples under HBSS rehydration was seen. The physiological process of swelling in the wet state is rather less pronounced in vivo, as the fibers are constrained with one another. The indentation moduli was shown to decrease of about 29% when going from dried to wet state in trabecular bone (Wolfram et al., 2010a). This is more than what we have measured in the axial direction of MTLT (average 5.4%). The fibers in MTLT are aligned in a parallel manner along the long axis of the tendon. The swelling in the axial and transverse directions of MTLT are likely the two extermes. The complex lamellar arrangement of mineralized collagen fibers in bone restricts the swelling, and the avarage amount of decrease in the indentation moduli with re-hydration process falls somewhat in the middle between the two extremes seen in MTLT.

Circumferential zone of MTLT showed higher anisotropy in both micro and nanoindentation than the interstitial zone. This could be caused by slightly different composition of the two types of morphology. In the fibril-array model by Reisinger et al. (2010) elastic anisotropy was proportional to volume fraction of the mineralized collagen fibrils in a fibril-array, so indirectly also to volume fraction of collagen in the array. This would suggest a higher volume fraction of collagen in the circumferential zone, as a factor contributing to the higher anisotropy of this zone. Additionally, the volume fraction of fibers observed with light microscopy is also higher in this zone (Spiesz et al., 2011b).

Higher anisotropy of the indentation moduli was resulting from the microindentation than from nanoindentation (see Table 4.1). This may be caused by the higher impact of microporosity on the indentation modulus obtained in the microindentation in the transverse direction of MTLT. Ad-

ditional compliance coming from bending of the mineralized collagen fibers of MTLT could be expected, if the obscured longitudinal micropores are present close to or within the indentation deformation zone. This is less likely the case in nanoindentation where the deformed volume is smaller. Also the final indentation depth in nanoindentation in transverse direction is higher than the one in axial direction, so due to the assumed indentation depth effects, the indentation moduli values may be underestimated. This would cause the overestimation of the stiffness anisotropy ratio of nanoindentation measurements in MTLT. Additionally damage accumulation (reduction of stiffness) under the tip may be dependent on the indentation depth.

The differences in the total indentation work measured in axial or transverse directions seem to be mainly influenced by the changing plastic work (see Fig. 4.4 a). Interestingly the elastic work is comparable in both indentation directions and for both dried and physiological conditions.

The ratios of elastic and plastic work (W_{el}/Wpl) suggest that more energy is dissipated in the indentation in axial direction than in the transverse one. This may be caused by an anisotropic post-yield behavior of MTLT. More energy is dissipated during indentation in axial direction, as more fibers slippage is likely to occur there. Also shear strain between the fibers is likely to be higher there, than in transverse direction. Similar results were observed by Hengsberger et al. (2002b) in indentation of human osteons. Dark (thick) lamellae (Ascenzi and Lomovtsev, 2006), where the fibers are arranged mostly in the direction along the osteon main axis showed more dissipation, which could be a similar situation to indentation of MTLT in axial direction of the fibers. Less dissipation was measured in bright (thin) lamellae, similar to transverse direction of indentation in MTLT.

The measurements performed here are indentations in a porous media and in this sense fulfill the conditions of the halfspace indentation in a homogenized sense and nano- and microindentation are valid methods of evaluating the average elastic properties of mineralized tissues (Hengsberger et al., 2002b; Oyen, 2006; Donnelly et al., 2006; Lewis and Nyman, 2008; Wolfram et al., 2010a,b), as well as other nature's and engineering materials (Berke et al., 2009; Jaeger et al., 2011).

4.6 Acknowledgments

This research was supported by grant no P19009-N20 of the Austrian Science Foundation (FWF). Authors would like to thank Paul Roschger and Phaedra Messmer for help with scanning electron microscopy images, as well as, Enrico Dall'Ara and Uwe Wolfram for fruitful discussions and advice.

Chapter 5

Homogenization

Based on manuscript:
"Experimental validation of a mean filed model of mineralized collagen fiber arrays at two levels of hierarchy."
By Ewa M. Spiesz, Andreas G. Reisinger, Paul Roschger and Philippe K. Zysset
In preparation, 2011.

5.1 Abstract

In the course of this study, stiffness of a fibril array of mineralized collagen fibrils modeled with a mean field method was validated experimentally at two levels of tissue hierarchy using mineralized turkey leg tendons (MTLT). The applied modeling approaches allowed to model the properties of this unidirectional tissue from nanoscale (mineralized collagen fibrils) to macroscale (mineralized tendon). At the microlevel, the indentation moduli obtained with a mean field homogenization scheme were compared to the experimental ones obtained with microindentation. At the macrolevel, the macroscopic stiffness predicted with micro finite element (μFE) models was compared to the experimental one measured with uniaxial tensile tests. Elastic properties of the elements in μFE models were injected from the mean field model or two directional microindentations.

Quantitatively, the indentation moduli can be properly predicted with the mean-field models. Local stiffness trends within specific tissue morphologies are very weak, suggesting additional factors responsible for the stiffness variations. At macrolevel, the μFE models underestimate the macroscopic stiffness, as compared to tensile tests, but the correlations are strong.

Keywords fiber array model, μFE model, mineralized turkey leg tendon (MTLT), experimental validation

5.2 Introduction

Mineralized tissues, as bone or mineralized turkey leg tendon (MTLT), and many other biological tissues are known to have hierarchical structures (Fratzl and Weinkamer, 2007). This complex design is optimized at many hierarchical levels, which is resulting in exceptional mechanical properties. Understanding the principles of this design could help creating synthetic biomaterials more compatible with the tissues to act as for example scaffolds for vascularized bone growth (Wu et al., 2011). On the other hand, it could provide input for material properties used in micro finite elements models, making them more specific.

Mineralized turkey leg tendon is a model tissue used frequently to study the structures of mineralized tissues, as well as, their mineralization process (Landis et al., 1996; Landis and Silver, 2002; Lees et al., 1994). Its advantage, next to similar composition and hierarchical structure, is the fact that the mineralized collagen fibers are arranged in an uniaxial manner, parallel to the main axis of the tendon, which strongly reduces the complexity of the structure compared to bone.

Some methods approaching the hierarchical modeling of mineralized tissues have been proposed (Fritsch and Hellmich, 2007; Nikolov and Raabe, 2008; Ghanbari and Naghdabadi, 2009). Results of such models are often compared to the literature values of e.g stiffness of different bones obtained experimentally, assuming the universal behavior of those tissues, based on mineralization mainly. Direct experimental validation at multiple hierarchical levels is missing. This type of validation brings some experimental challenges, as often testing the same samples at different length scales is very demanding or simply impossible.

Recently a mean field homogenization model of mineralized collagen fibril array was proposed by Reisinger et al. (2010). In this model, mineralized fibrils, the extra-fibrillar matrix and the resulting fibril-arrays are modelled as a function of the degree of mineralization, mineral distribution between fibrils and the extra-fibrillar matrix, collagen stiffness and the fibril volume fraction. This model may be of great help in understanding mechanical properties of the fibril arrays present in bone and MTLT, but requires validation. In this scope, the current study was an attempt of experimental validation of the model adapted to predict the stiffness of a mineralized collagen fiber at two hierarchical levels.

5.3 Materials and Methods

5.3.1 Design of the study

A scheme of experimental and modelling validation is shown in Fig. 5.1.

The design of the study involved, on one hand, experimental validation

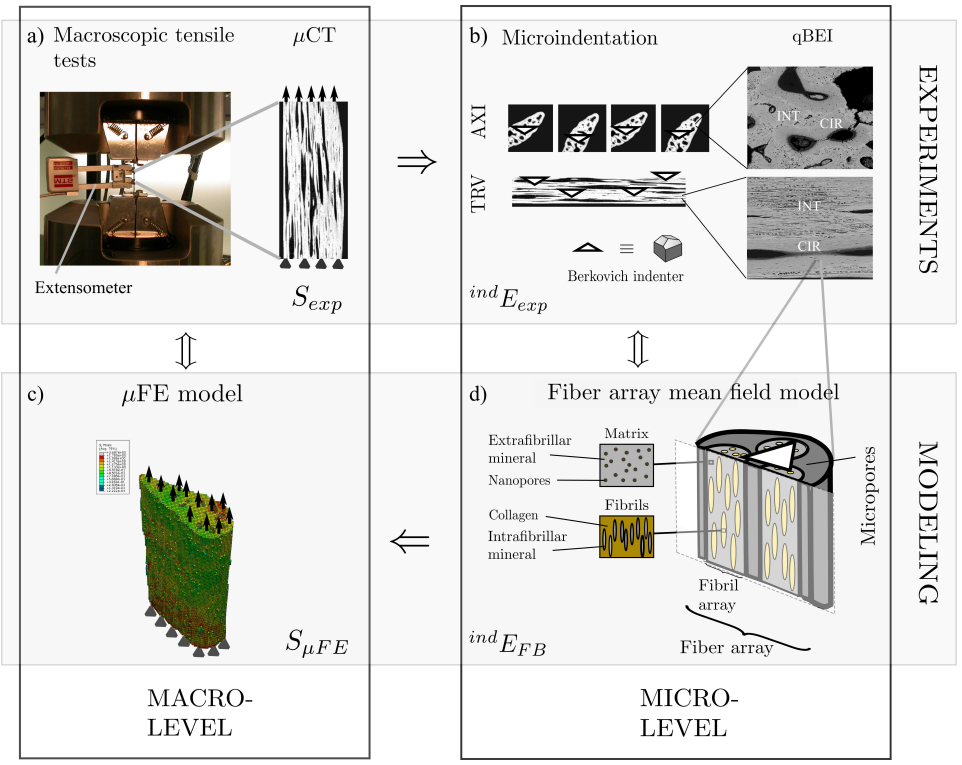

Figure 5.1: Design of the study: the macrolevel validation scheme involved macroscopic tensile tests (a) and μFE modeling (c). Experimental (S_{exp}) and predicted ($S_{\mu FE}$) macroscopic stiffness were compared. At the microlevel, the indentation modulus measured with microindentation ($^{ind}E_{exp}$, b) was compared to the indentation modulus predicted with the mean field fiber array model ($^{ind}E_{FB}$, d).

of the mean field homogenization approach to predict elastic properties of mineralized collagen fibers at the microscopic level (Fig. 5.1 d), where microindentation experiments were compared to indentation moduli predicted with the mean field models (Fig. 5.1 b). On the other hand, the elastic properties of the fibers obtained with the homogenization method were used as material properties in μFE models of MTLT (Fig. 5.1 c). Stiffness of such modelled structure was compared to the stiffness of the same structure tested experimentally in tension (Fig. 5.1 a), allowing validation of the model at the macroscale. Further, similar μFE models were prepared with material properties obtained with the microindentation in two orthogonal directions. Stiffness of such structures was also compared to experimental tensile tests.

5.3.2 Samples

Ten fresh, frozen mineralized flexor leg tendons (Bigi et al., 1996; Lees et al., 1994; Gupta et al., 2004; Spiesz et al., 2011b) were extracted from adult domestic turkeys (age over 24 weeks). The stiff mineralized part was divided from soft collagenous part. The outer soft tissue envelope was removed and the tendons were kept frozen ($-18°$C) until the day of tensile testing. Such prepared samples were tested macroscopically in tension (details in 5.3.5). After the tensile tests samples were cut into three pieces of approximately 10 mm of length: one from a region tested in tension (approximately 40-60% of the hard mineralized tendon length, see Fig. 5.1a) plus additionally one proximal (approximatelly 30-40% of the tendon tested in tension) and one distal specimen of the same length (approximatelly 60-70% of the tendon tested in tension).

5.3.3 Geometry, mineral and collagen content determination

All samples were scanned with μCT40 (Scanco Medical) with 12 μm spatial resolution, in dried state using an X-ray tube potential of 20 - 50 keV (160 ÂĬA) in order to obtain total volume of a sample ${}^{tot}V$ and the geometry for μFE simulations.

After μCT and mechanical tests in tension (see 5.3.5), the samples were embedded in epoxy resin (EpoFix, Struers, Ballerup, Denmark) without dehydration or resin infiltration and divided into 5 specimens (4 axial and one transverse, see Fig. 5.1b) each to obtain possibly most appropriate volume representation of the local properties. Such prepared specimens were glued to microscopy glass-slides and polished using a semi-automatic polishing machine (PM5, Logitech, UK) with silicon carbide papers series and a 1μm diamond suspension on a polishing cloth, until obtaining of a mirror surface (Wolfram et al., 2010a,b). Volume fraction of mineral was assessed using quantitative backscattered electron imaging (qBEI) with digital scanning electron microscope with a fourquadrant semiconductor backscattered electron detector (DSM 962, Zeiss), at working distance 15 mm (Roschger et al., 1995, 1998). Probe current was adjusted to 110 ± 0,4 pA and electron beam energy used was 20 keV. Images with 50x and 400x magnification were captured resulting in scanned area of approximately 2.0×2.5mm and 250×315μm, respectively. The images served as maps allowing recognition of the zones where mineralization was assessed for indentation. Both meso- and visible microporosity were thresholded. Concentration of calcium (wt.% calcium, ${}^{Ca,fi}\psi$) was determined (Roschger et al., 1998). Even though the biological apatites are non-stoichiometric with presence of foreign ions (Bigi et al., 1996), the inorganic phase consisting of calcuim phosphate was idealized as hydroxyapatite $Ca_{10}(PO_4)_6(OH)_2$. The calcium wt.% (${}^{Ca,fi}\psi$) were converted to hydroxyapatite mass fractions (${}^{mi,fi}\psi$ - mass fraction of the

mineral in the solid constituents of MTLT - no porosity considered) using stechiometric relationships (Roschger et al., 1998; Manjubala et al., 2009). Volume fraction of the mineral in fibers accounting for nano- and microporosity, (${}^{mi,fb}\phi$) was calculated according to Spiesz et al. (2011b). 526 regions of interest were selected for qBEI observations.

Within each region two types of morphology were distinguished: circumferential - around large vascular pores, with characteristic low microporosity and smaller fiber diameter and interstitial - between the large pores with higher microporosity and large fiber bundles (Spiesz et al., 2011b).

Volume fraction of collagen in the specimens was assessed with ashing in a laboratory furnace at 650°C for 24 hours (Ohman et al., 2007) and demineralization in EDTA solution for 20 days using the samples of approximately 30-40% and 60-70% of the mineralized parts of the tendons tested in tension was performed (Spiesz et al., 2011b).

Volume fraction of the fibrills in the fiber array (${}^{\mathrm{fl,fb}}\phi$) was estimated as the sum of the volume fraction of collagen and intrafibrillar mineral in the fiber array.

5.3.4 Evaluation of elastic properties of the tissue at microlevel

Two-directional microindentation

After qBEI analyzes the five slices of each sample: four axial and one transverse were indented. Nano-Hardness Tester (CSM Instruments, Peseux, Switzerland) with a Berkovich tip was used and measurements were conducted in a load control until the displacement limit of 2500nm. Indentations were performed in dried state. The resulting deformation region was approximately 17μm in diameter, which allowed for characterization of the tissue at the fiber array hierarchical level (including the mineralized collagen fibers and micropores). Indentation protocol involved trapezoidal loading/unloading with a constant rate of 120mN/s with 60 seconds holding time at maximum load to minimize the viscoelastic and/or viscoplastic effects. The two zones of morphology were treated separately in microindentation experiments.

Indentation curves showing abnormal shapes were discarded from further evaluation. The mineralization of the two zones of morphology proved low heterogeneity within a zone (Spiesz et al., 2011b), which allowed for defining outliers as values higher than 1.5 times the interquartile range above the third quartile and below the first quartile (Crawley, 2005).

Sample averages were calculated using the indentation moduli of a zone (circumferential or interstitial) weighted with a volume fraction of the zone (approximated as an average of the 4 axial slices of each sample from segmented qBEI images). Additionally, an average of the 10 samples was cal-

culated.

A procedure that approximates a transverse-isotropic stiffness tensor from indentation moduli in two orthogonal directions (Franzoso and Zysset, 2009; Swadener and Pharr, 2001) was used to estimate the elastic constants of samples and served as an input material propersties for the μFE models.

Mean-field homogenization scheme

Mean field methods were applied to model mineralized fibrils, the extrafibrillar matrix and the resulting fibril array (Reisinger et al., 2010) of MTLT. According to Reisinger et al. (2010), mineralized collagen fibrils were modeled as continuous collagen matrix with spheroidal mineral inclusions. Extrafibrillar matrix was modeled as continuous mineral matrix with spherical voids (a mineral foam). Mineralized collagen fibers were modelled as long spheroidal fibrils in the extracellular matrix. As the hierarchical level of MTLT tested with microindentation involved some microporosity, the original model of the fibril array presented by Reisinger et al. (2010) was enriched with the micropores to predict the stiffness of a fiber array (see Fig. 5.1). Microporosity was accounted for in the volume fractions of mineral and collagen before entering into the main homogenization scheme described by Reisinger et al. (2010). Stiffness tensors were computed as a function of degree of mineralization ($^{mi,fb}\phi$), mineral distribution between fibrils and extra-fibrillar matrix (α) and fibril volume fraction ($^{fl,fb}\phi$), as well as stiffness of hydroxyapatite - 110.15 GPa (Yao et al., 2007) and collagen - 5.0 GPa to simulate dried collagen (Buehler, 2007; van der Rijt et al., 2006; Akkus, 2005).

The range of input parameters of the mean field model for the ten samples tested are shown in Tab. 5.1. Circumferential and interstitial zones were modelled separately. Parameters like Young's moduli and Poisson's ratios of mineral and collagen phase, as well as, the geometry of the phases were taken from literature (sources listed in the Tab. 5.1). Volume fraction of mineral in the fibrils $^{\mathrm{mi,fi}}\phi$, in the fiber array $^{\mathrm{mi,fb}}\phi$ and volume fraction of collagen (and the resulting volume fraction of fibrils in the fibril array $^{\mathrm{fl,fb}}\phi$) were determined experimentally as explained in Section 5.3.3.

Mineral distribution between collagen fibrills and the extrafibrillar matrix is widely discussed in the literature (Fratzl, 2008), but some contradictory views are presented, starting with mineral placed in the collagen fibrils mostly (Weiner et al., 1999; Jaeger and Fratzl, 2000; Gao et al., 2003), going through about 25% of mineral in the fibrils (Lees et al., 1994; Sasaki et al., 2002), down to mineral placed mostly outside of the fibrills (Hellmich and Ulm, 2002). In the above literature, the methods of direct visualisation suggest that much of the mineral is within the collagen fibrils, while the simulations suggest the other case: in order to obtain stiffness measured experimentally, more mineral needs to be put in the extrafibrillar matrix

(Nikolov and Raabe, 2008; Fratzl, 2008). Previous study by Spiesz et al. (2011b) suggested more mineral placed in the fibrils in the circumferential zone than in the interstitial one (∼0.7 and 0.3, respectively). This configuration of mineral distribution parameter was used and resulted in an average α for the 10 samples of 0.56. Additionally, the α parameter was varied from 0.2 - 0.9 (see Tab. 5.2).

5.3.5 Evaluation of elastic properties of the structures at macrolevel

Tensile tests

The ten MTLT samples (approximately 30-40% of the hard mineralized part of the tendon) were tested with a servo-hydraulic testing machine (MTS 858 mini Bionix, USA). The tests involved quasistatic cyclic tensile loading in elastic region (0-0.03 % strain), controlled in displacement measured with an extensometer (Mini-Bionix MTS system, Milwaukee, MN, USA) with 10mm gage range, with the amplitude of 0.1 Hz. After ten pre-conditioning cycles with the same protocol, three cycles of measurement were performed. The experimental set-up of macroscopic mechanical tests in tension is shown in Fig. 5.1a. Stiffness $S[N/mm]$ in the tensile tests was defined as force over displacement.

μFE analyzes

The meshes used in μFE models were obtained from segmented μCT scans. The segmentation was performed using a single level threshold (Wolfram et al., 2010b). The tissue voxels were converted to the model elements and rescalled 3 times (to 36μm) to reduce the computing time. The linear elastic elements were assigned elastic properties obtained with fiber array model (subsection 5.3.4) on one hand and with elastic constants estimated from microindentation in two directions (subsection 5.3.4), on the other. The simulation of the experimental tension test in elastic region with boundary conditions as shown in 5.1c were performed. As the input parameters of the mean field model were evaluated separately for circumferential and interstitial zone of MTLT a homogenized values of those were calculated for a sample. A weighted average (with volume fraction of a zone evaluated from segmented qBEI images of 4 axial slices of each sample, as weight) of the predicted properties was used as a sample-wise input to the model resulting in a homogenized stiffness tensors of a sample. Those were used as material properties assigned to the elements of the μFE meshes.

Additionally, the elastic properties obtained from indentation in two directions and the procedure inverse to the Swadener and Pharr, as described in 5.3.4 were used in similar μFE models for comparison.

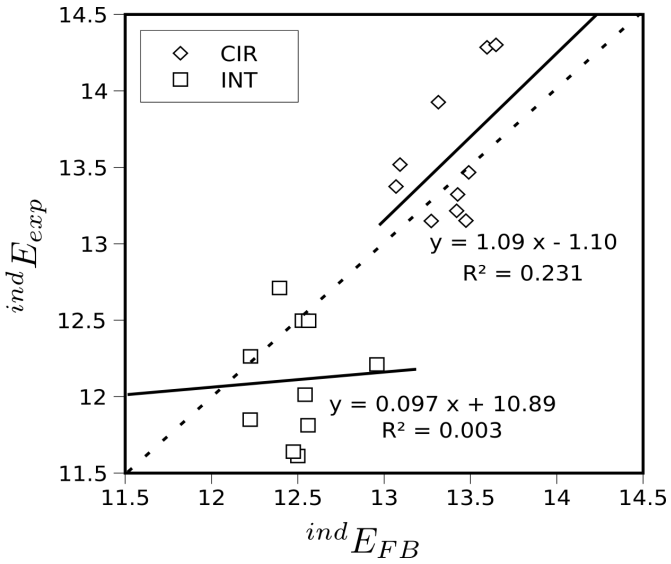

Figure 5.2: Comparison of indentation moduli obtained experimentally $^{ind}E_{exp}$ with microindentation and predicted with the fiber array model $^{ind}E_{FB}$ for circumferential (CIR) and interstitial (INT) zone.

Statistics

The Williams's formula and the procedure proposed by Steiger (1980) were used to compare the correlation coefficients with different input parameters at significance level of p=0.05 (Dall'Ara et al., 2011).

5.4 Results

5.4.1 Validation at microscale

Validation at the microscale involved comparing the indentation moduli obtained in microindentation $^{ind}E_{exp}$, with those predicted with mean field homogenization models $^{ind}E_{FB}$, which input parameter such as mineralization and volume fraction of collagen were measured on the samples indented (summary of results in Table 5.1). An average moduli for circumferential and interstitial zone of each of the 10 samples was calculated. The resulting correlation between the experiments and modeling is shown in Figure 5.2. Averages of the axial indentation moduli of all of the samples samples (no zone distinction), both measured and predicted (for different α values) are shown in Tab. 5.2.

The differences between the two morphology zones are well represented by the fibril array model (see Fig. 5.2). Within one morphology zone the trends are very weak, which suggests additional factors contributing to a lo-

Input parameter	(Average ± STD) value	Source	Variation
Collagen Young's modulus	$Ecl = 5$ [GPa]	van der Rijt et al. (2006)	-
Collagen Poisson ratio	${}^{\mathrm{cl}}\nu = 0.3$ [-]	Reisinger et al. (2010)	-
Mineral Young's modulus	$Emi = 110.15[GPa]$	Yao et al. (2007)	-
Mineral Poisson ratio	${}^{\mathrm{mi}}\nu = 0.28$ [-]	Yao et al. (2007)	-
Mineral platelet aspect ratio in fibril	${}^{\mathrm{fl}}a = 14$ [-]	Akkus (2005)	-
Void aspect ratio in extra-fibrillar matrix	${}^{\mathrm{ma}}a = 1$ [-]	Reisinger et al. (2010)	-
Fibril aspect ratio in fiber-array	${}^{\mathrm{fa}}a = 100$ [-]	Birk et al. (1997)	-
Mineral distribution parameter	$\alpha = 0.25$ - 0.77 [-]	Lees et al. (1994) Sasaki et al. (2002)	0.2 - 0.9
Fibril vol. fraction in fiber-array	${}^{\mathrm{fl,fb}}\phi = 0.50$ (0.06) [-]	-	0.36 - 0.63
Mineral vol. fraction in fiber-array	${}^{\mathrm{mi,fb}}\phi = 0.20$ (0.01) [-]	-	0.19 - 0.21

Table 5.1: Summary of the input paramaters in the fiber array model. The top part of the table shows the parameters, which were taken from literature. The bottom part shows results obtained in this study and used as input for the mean field fiber array models.

Experiments - Microindentation	Modeling - Fiber array model	
${}^{ind}E_{exp}$ [GPa] (STD)	${}^{ind}E_{FB}$ [GPa] (STD)	α
12.85 (1.24)	14.14 (0.54)	0.2
	13.13 (0.26)	0.5
	10.35 (0.69)	0.9

Table 5.2: Validation of the fiber array model at the microlevel. ${}^{ind}E_{exp}$ - indentation modulus measured in axial direction with standard deviation in brackets (STD), ${}^{ind}E_{FB}$ - indentation modulus in axial direction predicted with the mean field model, α - mineral distribution parameter showing the fraction of mineral placed within collagen fibrils.

cal stiffness that are not accounted for in the current model (e.g. nanoporosity that was not assessed experimentally for the MTLT samples).

5.4.2 Validation at macroscale

Validation at macroscale involved comparison of the stiffness of MTLT structure measured experimentally in tension, to the stiffness of the same structure simulated with μFE, which material properties were evaluated with mean field homogenization models or indentation. Comparison between the stiffness of the simulated structures, plotted against the stiffness of the structures measured experimentally is presented in the Fig. 5.3.

The coefficients of determination for the correlations observed between the experimentally acquired macroscopic stiffness (S_{exp}) and μFE simulations (with elastic properties of the elements obtained with the fiber array homogenization approach, $S_{\mu FE}$) are shown in Tab. 5.3. The highest correlation was obtained with the highest α of 0.9 - most mineral placed outside of the collagen fibrils ($R^2 = 0.962$), but the differences of the correlations were statistically not significant (p=0.073 for comparison of the two extreme cases: α=0.2 and α=0.9 using the Steiger's formula (Steiger, 1980; Dall'Ara et al., 2011)). The macroscopic stiffness predicted with the models is lower than the experimental one for all of the cases.

Additional step involved comparison of the experimentally assessed structure stiffness (S_{exp}) with the stiffness predicted with the μFE with two-directional indentation used for evaluation of material properties of the elements. This method is commonly used and was validated before for bone (Chevalier et al., 2007; Wolfram et al., 2010a). Results of this comparison are shown in Figure 5.2. The average macroscopic stiffness predicted with the μFE simulations with microindentation in two directions is also somewhat lower than the experimental average (see Tab. 5.3), but is highly correlated to the experimental results of the 10 samples ($R^2 = 0.950$), see

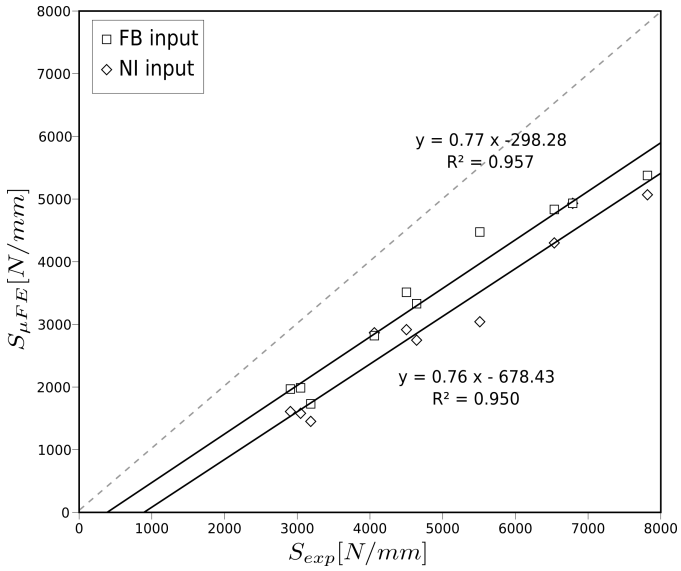

Figure 5.3: Comparison of stiffness obtained with microscopical tension tests and predicted with μFE simulation with elastic properties of the elements obtained from the fiber array model (FB input) and indentation (NI input).

Experiments - Macroscopic tensile tests	Modeling - μFE (fiber array input)		
S [N/mm] (STD)	S [N/mm] (STD)	α	R^2
4899 (1712)	3407 (1323)	0.2	0.946
	3496 (1356)	0.5	0.957
	3813 (1473)	0.9	0.962
	μFE (microindentation input)		
	3051 (1337)	-	0.950

Table 5.3: Comparison of the macroscopic stiffness S with standard deviation in brackets (STD) obtained with the tensile tests and μFE simulations with the elements stiffness obtained with the mean filed models for a given α - mineral distribution parameters.

Fig. 5.3.

5.5 Discussion

An attractive model of mineralized collagen fibril array proposed by Reisinger et al. (2010) was adapted to predict the stiffness of the uniaxial mineralized collagen fibers of MTLT and checked for relevance at micro and macrolevel.

This model has a potential to improve our understanding of mechanical behavior of mineralized tissues at different hierarchical levels, but was not validated experimentally before.

Here we show that it could appropriately predict indentation stiffness of the fibers based on their morphological parameters (mineralization, collagen content etc.). This prediction correlates overall well with experimental microindentation results (the sum of circumferential and interstitial data points falls approximately along the 1:1 line). This suggests that mineralization is an overall good predictor of the stiffness for larger ranges of mineral volume fractions (as mineralization is the strongest stiffness predictor in the model used), but locally other factors are playing a significant role. The stiffness trends within a morphology zone can not be properly predicted with the current model and input parameters set ($R^2 = 0.232$ for circumferential and $R^2 = 0.003$ for the interstitial zone). In bone, one of the factors responsible for the lack of correlation could be the arrangement of the fibers (Spiesz et al., 2011a), but this factor is excluded in MTLT, which shows an uniaxial arrangement. Also the chemistry of the collagenous phase, as well as, the non-collagenous proteins may play a role in the variability of mechanical properties of mineralized tissues. A other factor could be nanoporosity, which is poorly assessed for both bone and MTLT.

Mineral distribution inside or outside of collagen fibrills was shown by Reisinger et al. (2010) and Nikolov and Raabe (2008) to have influence of fibril array stiffness. In this study, at microlevel the α best fitting experimental indentation moduli (in axial direction) was 0.5 - half of the mineral inside collagen fibers and half in the extrafibrillar matrix. As MTLT is a dynamic tissue undergoing calcification and possibly remodelling, there would be a distribution of the α parameter expected. Depending on the fact if the large collagen fibers already present in the tendon are undergoing calcification, or if there is new collagen matrix laid down and is calcifying, the distribution of mineral may be different. It could be proposed that more mineral would be able to penetrate inside collagen fibrils in the newly remodeled tissue, than to the well developed fibers of the one older in tissue age.

The contribution of mineral distribution parameter to the macroscopic stiffness of MTLT was minimal. By changing the mineralization from mostly extrafibrillar ($\alpha = 0.2$) to mostly intrafibrillar ($\alpha = 0.9$) the changes in determination coefficient R^2 for the comparison of μFE results with the experiments was negligible (p=0.073) changing from 0.946 to 0.962, respectively. This parameter is important in micromechanical analysis of the tissue, but other factors (mainly tissue geometry and micro- and macroporosity) have more impact on the overall macroscopic elasticity of the tissue. Similar conclusions were drawn by Granke et al. (2011) from ultrasound tests of bone at mesoscopic level.

The macroscopic stiffness S is underestimated with the μFE models with both types of input parameters (indentation or mean-field models). This

could be an artifact coming from the resolution of the μCT scans (12μm). Microporosity (pores between the mineralized collagen fibers of MTLT) is partially invisible in those scans, which enlarges the average cross-sectional area of the samples, resulting in lower stiffness values. This problem is excluded at the microlevel, as there the microporosity is accounted for properly.

The approach used in this study shows that the mean-field model could be used to generate elastic properties of a material for the use in μFE simulations. This could be an alternative to the indentation technique commonly used for this purpose (Chevalier et al., 2007; Wolfram et al., 2010a).

The mean field methods were used here to model the uniaxial structure of MTLT. Modifications of the models, that would include the orientation of the mineralized collagen fibers, could help in understanding lamellar structure of bone and its extraordinary mechanical performance (Reisinger et al., 2011). This type of models, after validation, are extremely valuable because the experimental possibilities of determination of features like for example mineral distribution between collagen fibrils and extrafibrillar matrix at nano- and microlevels are very challenging. Here, based on the microscopical response of the whole structure we could draw conclusions about the underlying mechanisms of the tissue performance. This approach could be used in understanding for example the tissue properties in the case of bone metabolic diseases and possibly help improving treatments.

We believe that this study provides an unique dataset obtained from the same specimens at different levels of structural hierarchy, that allows for validation of models at multiple length scales.

5.6 Acknowledgments

This research was supported by grant no P19009-N20 of the Austrian Science Foundation (FWF). Authors would like to thank Peter Varga for organizing the samples and help with image processing, Enrico Dall'Ara for help with macroscopic mechanical tests and statistics and Phaedra Messmer for assistance with qBEI measurements.

Chapter 6

Lamellar bone

Based on manuscript:
"Variability of Indentation Modulus in Human Lamellar Bone Cannot be Explained by Mean Fibril Orientation and Mineral Mass Fraction."
By Andreas G. Reisinger*, Ewa M. Spiesz*, Paul Roschger, Werner Kaminsky, Dieter H. Pahr and Philippe K. Zysset
Submitted to Bone, 2011.
* - the two authors contributed equally to the work of this manuscript.

6.1 Abstract

This study attempts to reveal a site-matched correlation between mineralization and mean collagen orientation with indentation stiffness.

For this purpose osteons from the mid-shaft of a human femur were investigated in order to quantify the extent of mineralization (by quantitative backscattered electron imaging), the arrangement of mineralized collagen fibrils (by quantitative polarized light microscopy) and indentation stiffness (by nanoindentation). A fibril array mean field homogenization model incorporating the measured morphological parameters was employed to predict the indentation stiffness. The correlation between the measured and predicted indentation moduli was established.

The correlation between the measured and the predicted indentation modulus that accounts for tissue mineralization only was surprisingly low ($r^2 = 0.014$). Against the expectations, incorporating the information of the out-of-plane collagen fibril angle into the model did not improve the stiffness prediction substantially ($r^2 = 0.026$), although the improvement was statistically significant ($p = 0.007$).

Other factors influencing the stiffness, like nanoporosity, chemistry of the phases building bone structural units and others might need to be included in order to properly understand the variability of indentation modulus.

6.2 Introduction

The influence of the constituents and their arrangement in bone on the mechanical properties of this tissue was widely investigated in the past decades (Fratzl and Weinkamer, 2007; Fratzl, 2008; Weiner et al., 1999; Olszta et al., 2007). The sensitivity of some of the factors on stiffness of a uniaxial mineralized collagen fibril array was investigated by Reisinger et al. (2010).

The factor considered as the one mostly influencing the stiffness of this tissue was the extent of mineralization. Unfortunately, the amount of hydroxyapatite - the stiffest of the phases constituting the hierarchical structure of bone - was proved to have limited influence on the stiffness (Raum et al., 2006; Hengsberger et al., 2002a; Boivin et al., 2008; Follet et al., 2004; Zebaze et al., 2011) as well as strength (Martin and Ishida, 1989), what resulted in intensive research of other factors of possible influence. Martin and Ishida (1989) found the collagen fibril orientation to be the most important determinant that is supposed to follow three different alignment patterns in osteonal bone. According to the either dark, bright or intermediate appearance of osteons in polarized light microscopy (PLM), they are expected to own an either longitudinal, transverse or alternating collagen orientation (Ascenzi and Bonucci, 1967, 1968). The collagenous structure appears even more complex when considering the fibrous arrangement in a single osteonal lamella, that is supposed to follow distinct patterns (Giraud-Guille, 1998; Weiner et al., 1999; Wagermaier et al., 2006).

Beside mineralization and collagen orientation other governing factors for bone stiffness were investigated: the amount and chemistry of the organic phase (volume fraction of collagen, cross-linking patterns of the collagen molecules, non-collagenous proteins), distribution of the mineral between collagen fibrils and extrafibrillar matrix (Reisinger et al., 2010; Nikolov and Raabe, 2008; Lees et al., 1994; Sasaki et al., 2002), arrangement of collagenous matrix (Reisinger et al., 2011; Spiesz et al., 2011a; Boyde and Riggs, 1990; Hengsberger et al., 2002a; Bromage et al., 2003; Skedros et al., 2009), nano- and microporosity (Granke et al., 2011; Spiesz et al., 2011b) and others.

However, the analyzed structure-function relationships were not investigated on a very local, or even site-matched basis.

In this scope, the following hypothesis is stated and tested on a site-matched basis in the study: *Lamellar bone stiffness as measured by nanoindentation, can be expressed by local mineral mass fraction and local collagen orientation.*

The hypothesis is tested by first individually correlating the site-matched mineralization and collagen fibril angle with experimentally measured indentation stiffness. To assess the simultaneous influence of mineralization and collagen orientation, these two factors are used as input parameters in a bone material model to predict a corresponding numerical indentation mod-

uli that could be compared to the measured one.

6.3 Materials and Methods

6.3.1 Sample Preparation

Human femurs from two donors (a male of 68 and a female of 89 years old) were dissected and kept frozen in $-20°$ until the day of sample preparation. The donors were free from bone related pathologies and the samples were obtained via an informed consent. Slices of approximately 10 mm were cut from the midshaft of the femurs using a low-speed precision diamond band saw (Exakt Vertriebs GMBH, Norderstedt, Germany) under constant water irrigation. Out of those two samples slices of approximately 1mm were cut using the same machine. Four different cut angles (0°, 30°, 45°, 60° to the shaft main axis) were introduced as shown in Fig. 6.1. Such prepared slices were washed in a soap solution in de-ionized water for 7 minutes in an ultrasonic bath, fallowed by a 7 minutes bath in a 2% bleach solution and than washed under running de-ionized water (Franzoso and Zysset, 2009). After the cleaning procedure the samples were dried in room temperature for 12h. Parallel slices of $\sim$ 1mm thickness were glued to glass slides using Loctite 420 glue (Henkel Loctite Adhesives Ltd, UK) and polished with a semi-automatic polishing machine Exakt 400CS (Exakt Vertriebs GMBH, Norderstedt, Germany) until obtaining $30 - 60\mu m$ sample thickness.

6.3.2 Quantitative backscattered electron imaging (qBEI)

Quantitative backscattered electron images (qBEI) were captured using digital scanning electron microscope with a fourquadrant semiconductor backscattered electron detector (DSM 962, Zeiss), at working distance 15 mm (Roschger et al., 1995, 1998). Probe current was adjusted to 110 ± 0,4 pA and electron beam energy used was 20 keV. Images with 50x and 400x magnification were captured resulting in a scanned area of approximately 2.0×2.5mm and 250×315μm, respectively. The images served as maps allowing recognition of the zones where mineralization was assessed for subsequent indentation. Concentration of calcium (weight % calcium, ${}^{ca,fa}\psi$) was determined (Roschger et al., 1998). Both meso- and visible microporosity were thresholded. The inorganic phase consisting of calcium phosphate was idealized as hydroxyapatite $Ca_{10}(PO_4)_6(OH)_2$. The calcium wt.% (${}^{ca,fa}\psi$) was converted to hydroxyapatite mass fraction (${}^{mi,fa}\psi$ - mass fraction of the mineral in the fibril) using stoichiometric relationships and the assumption of no porosity in the tissue as in Roschger et al. (1998); Manjubala et al. (2009). The volume fraction of the mineral in the fibril array ${}^{mi,fa}\varphi$ accounting for nanoporosity was calculated using an empirically obtained relationship between ${}^{mi,fa}\varphi$ and the ultrastructural mass density from Fritsch and Hellmich

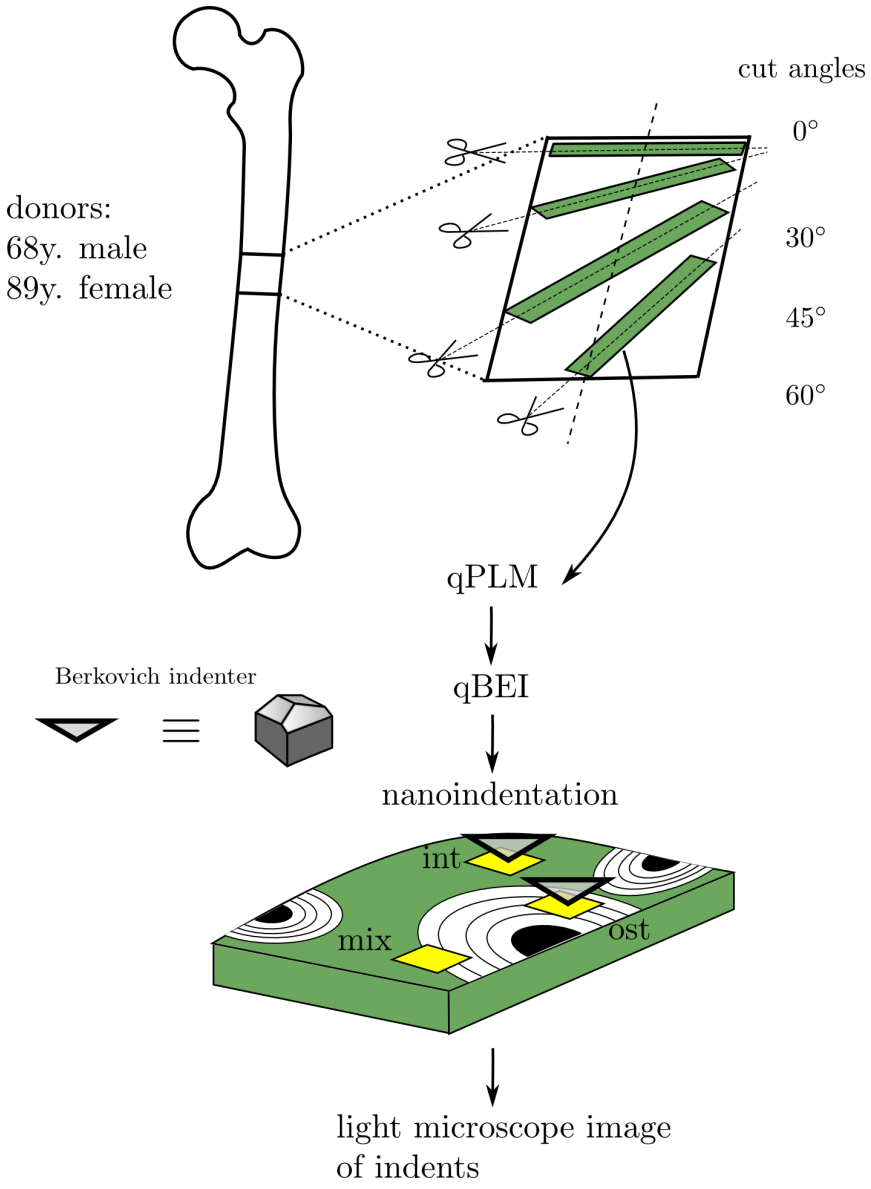

Figure 6.1: Study design and sample preparation. Seven femoral bone slices were obtained from two different donors at 4 cut angles (0°, 30°, 45°, 60°) relative to the shaft axis. The slices were imaged by qBEI and qPLM and then indented in three regions (OSTeonal, INTerstitial, MIXed). Light microscope images of the indented sites were taken.

(2007).

$$^{\mathrm{mi,fa}}\varphi = \frac{B\ ^{\mathrm{mi,fa}}\psi}{^{\mathrm{mi,fa}}\psi - A\ \rho_{\mathrm{HA}}} \tag{6.1}$$

with $A = 0.59$ ml/g and $B = -0.75$. The density of hydroxyapatite ρ_{HA} is set to 3.16 g/cm^3 (de With et al., 1981). As a result, images of osteonal bone, showing the local degree of mineralization $^{\mathrm{mi,fa}}\varphi(x, y)$ as volume fraction were obtained Fig. 6.2c.

6.3.3 Quantitative polarized light microscopy (qPLM)

A non-quantitative polarized light microscopy used before by Martin and Ishida (1989); Boyde and Riggs (1990); Bromage et al. (2003); Skedros et al. (2009), was recently calibrated for the quantitative use on bone by Spiesz et al. (2011a). The out-of-plane collagen arrangement angle θ (the angle that collagen fibrils make with the normal to the specimen surface) in a parallel fibered mineralized turkey leg tendon (MTLT) was calibrated to the linear birefringence of MTLT cut at variety of angles to the main axis. The calibration curve was normalized to sample thickness and wavelength of the probing light to enable a universally applicable quantitative assessment (Spiesz et al., 2011a). The angle θ for bone sections represents the average out-of-plane collagen fibril arrangement angle. The system used consisted of a microscope for polarized light, interference filter and broadband quarter-wave retarder to produce incident circular polarized light, as well as an image multiplexer (Quadview, MAG Biosystems) and a CCD camera (Kaminsky et al., 2007; Spiesz et al., 2011a). The qPLM observations result in images with gray-scale coded fibril angle (or collagen angle) $\theta(x, y)$ given for a pixel Fig. 6.2d.

6.3.4 Nanoindentation

The acquired qBEI images served as maps for the selection of regions of interest for indentation. In each sample section 5-30 qBEI images were taken at 400x, defining the regions of interest for indentation. Indentations were performed in dried conditions using the TriboIndenter, Hysitron, USA. A Berkovich indenter was used and measurements were conducted in a displacement control until 500nm depth using a loading/unloading rate of 40nm/s and holding time of 30sec. Patterns of 33 indents were placed within the regions of interest Fig. 6.2a. The pattern size was approximately 60x60 μm.

Three types of regions of interest were defined: (ost)eonal - within an osteon, (int)erstitial - in the interstitial tissue, (mix)ed - partially within an osteon and partially within the interstitial tissue, as shown in Fig. 6.1b.

The patterns were scanned with the Berkovich tip after indentation in the scanning probe microscopy mode of the TriboIndenter (Hysitron, USA)

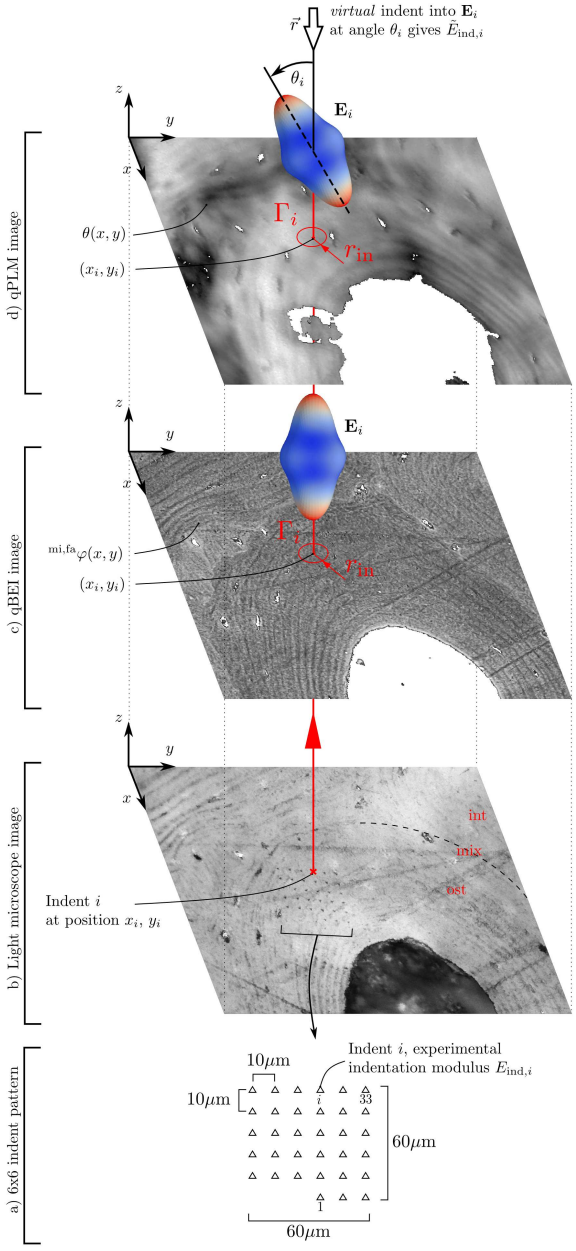

Figure 6.2: Site-matched image analysis. (a) 57 indent patterns are distributed on osteons (ost), the interstitial zones (int) and in not clearly identifiable regions (mix). (b) The position (x_i, y_i) of each indent i is assessed by light microscope images. (c) Calibrated qBEI images of the indentation zone, displaying the tissue mineral volume fraction $^{\mathrm{mi,fa}}\varphi(x,y)$, are registered to the light microscope images. The average $^{\mathrm{mi,fa}}\varphi$ in the indent-surface interaction zone Γ_i is used to model the local bone tissue stiffness tensor $\mathbf{E}_i$. (d) Calibrated qPLM images of the indentation zone, displaying the local fibril angle $\theta(x,y)$ relative to the sample surface normal, are registered to the qBEI- and light microscope images. The average fibril angle in the indent-surface interaction zone Γ_i is used to model an appropriately oriented indent into the material $\mathbf{E}_i$ yielding $\tilde{E}_{\mathrm{ind},i}$.

in order to detect any abnormalities in the surface nearby the indents or problems with surface detection resulting in a corrupt indent size. Additionally, each pattern was imaged with light microscopy in order to match the indentation sites with the sites where mineralization and collagen arrangement were measured.

The following 2-step indent filtering procedure was applied in order to remove the corrupt indents:

1. Indents that could not be clearly identified on surface images or that were placed in or nearby pores or cracks were excluded.

2. Indents, which load-displacement curve contained irregularities from the regular shape were removed manually.

6.3.5 Site-matched assessment of E_{ind}, ${}^{\mathrm{mi,fa}}\varphi$ and θ

To allow a site-matched assessment of measured indentation modulus E_{ind}, degree of mineralization ${}^{\mathrm{mi,fa}}\varphi$ and fibril orientation θ, the obtained light microscopy images, qBEI images and qPLM images were registered Fig. 6.2. For an indentation modulus $E_{\mathrm{ind},i}$ at position (x_i, y_i) on the light microscope image, a corresponding mineral volume fraction ${}^{\mathrm{mi,fa}}\varphi_i$ and fibril orientation angle θ_i can then be extracted from the images via

$$ {}^{\mathrm{mi,fa}}\varphi_i = \frac{1}{A_{\mathrm{in}}} \int_{\Gamma_i} {}^{\mathrm{mi,fa}}\varphi(x,y)\mathrm{d}\Gamma \qquad \theta_i = \frac{1}{A_{\mathrm{in}}} \int_{\Gamma_i} \theta(x,y)\mathrm{d}\Gamma \tag{6.2} $$

The field data ${}^{\mathrm{mi,fa}}\varphi(x,y)$ and $\theta(x,y)$ are averaged on a circular area Γ_i with the radius r_{in}, centered at the respective indent location (x_i, y_i) Fig. 6.2cd. This circle represents the interaction zone between indenter tip and sample surface and holds a diameter of seven times the indentation depth $2r_{\mathrm{in}} = 7{\times}500nm = 3500nm$ (Hengsberger et al., 2002b). Its area is therefore $A_{\mathrm{in}} = r_{\mathrm{in}}^2\pi$.

6.3.6 The modeled indentation modulus $\tilde{E}_{\mathrm{ind}}$

For each measured indentation modulus $E_{\mathrm{ind},i}$, a corresponding *virtual* indentation modulus $\tilde{E}_{\mathrm{ind},i}$ is now estimated that is based on the local mineral volume fraction ${}^{\mathrm{mi,fa}}\varphi_i$ and fibril angle θ_i. This is achieved by the following two-step procedure.

Fibril-array model

First, the local degree of mineralization ${}^{\mathrm{mi,fa}}\varphi_i$ is used in a micromechanical material model of the fibril-array to calculate the stiffness tensor $\mathbf{E}_i$ of the local bone matter Fig. 6.2c.

Table 6.1: Set of input parameters for the fibril-array model of Reisinger et al. (2010).

Input parameter	Value	Reference
Collagen Young's modulus	5 GPa	Cusack and Miller (1979)
Collagen Poisson ratio	0.3	-
Mineral Young's modulus	110.5 GPa	Yao et al. (2007)
Mineral Poisson ratio	0.28	Yao et al. (2007)
Mineral platelet aspect ratio in fibril	14	Akkus (2005)
Void aspect ratio in extra-fibrillar matrix	1	-
Fibril aspect ratio in fibril-array	100	-
Fibril volume fraction in fibril-array	0.53	Fritsch and Hellmich (2007)
Mineral quota of total mineral in fibril	0.25	Lees et al. (1994)

When modeling the tissue elastic properties at an individual indentation location, the model has to reflect the bone microstructure at the lengthscale of the indentation influence zone Γ_i. The zone's diameter of $2 \times r_{\text{in}} = 3.5\mu$m is around half the width of an average osteonal lamella in human bone which is approximately 5-7μm (Rho et al., 1998). On this sublamellar lengthscale, the fibril organization is assumed to be rather unidirectional, array-like. Parallel mineralized collagen fibrils are embedded in a mineralized extra-fibrillar matrix (Lees et al., 1994).

In this context, the multiscale micromechanical fibril-array model of Reisinger et al. (2010) may be used. It applies mean field methods to model mineralized fibrils, the extra-fibrillar matrix and the resulting fibril-array Fig. 6.3. The transverse isotropic elastic properties of the fibril-array are computed as a function of degree of mineralization, mineral distribution between fibrils and extra-fibrillar matrix, collagen stiffness and fibril volume fraction.

In this work, all input parameters except the degree of mineralization are set to constant values listed in Tab. 6.1 that are supposed to conform average human lamellar bone. The local transverse isotropic stiffness tensor $\mathbf{E}_i$ of the bone tissue within the deformed zone of an indent i is then calculated as a function of local mineralization ${}^{\text{mi,fa}}\varphi_i$ only.

$$\mathbf{E}_i = f({}^{\text{mi,fa}}\varphi_i) \tag{6.3}$$

Virtual indentation

In a second step, the indentation modulus $\tilde{E}_{\text{ind},i}$ for a virtual indent into the modeled material is estimated using the theory of Swadener and Pharr (2001). The appropriate direction for this virtual indent is defined by θ_i, the angle between the fibril- and the experimental indentation direction Fig. 6.2d.

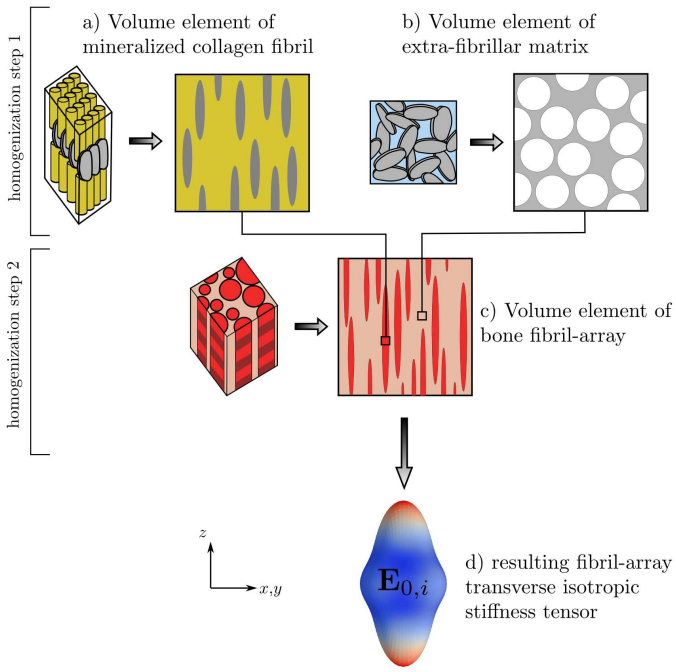

Figure 6.3: Mean field model representations of bone micro- and nanostructures and multiscale workflow: (a) fibril structure is modeled as a composite with prolate isotropic mineral spheroids unidirectionally embedded in an isotropic collagenmatrix; (b) extra-fibrillar mineral-protein network is modeled as a mineral foam with spherical voids; (c) fibril-array is built of highly elongated prolate spheroids of fibril material, embedded in extra-fibrillar matrix material; (d) output is the transverse isotropic stiffness tensor of the fibril-array

$$\tilde{E}_{\mathrm{ind},i} = \mathrm{Sw}(\mathbf{r}_i, \mathbf{E}_i) \quad \text{with} \quad \mathbf{r}_i = \begin{bmatrix} 0 \\ \sin(\theta_i) \\ \cos(\theta_i) \end{bmatrix} \tag{6.4}$$

with Sw being a function returning the indentation modulus of a virtual indent into a material $\mathbf{E}_i$ in arbitrary direction defined by the vector $\mathbf{r}$ described in the material coordinate system.

An indentation modulus $\tilde{E}^{\theta=0}_{\mathrm{ind},i}$ that neglects the influence of the fibril orientation and that is just based on the local mineralization is gained by holding θ_i constant at 0° (indentation in the axial direction of the fibrils).

6.3.7 Statistics

Fifty-seven indentation patterns, each with up to 33 valid indents were distributed on several samples. For further evaluation, the means of the n valid indentation modules, mineralization and fibril angle values of each indentation pattern are calculated Fig. 6.2a. Each indentation pattern holds then a single value of $\bar{E}_{\mathrm{ind}}$, $\bar{\tilde{E}}_{\mathrm{ind}}$, $\bar{\tilde{E}}^{\theta=0}_{\mathrm{ind}}$, ${}^{\mathrm{mi,fa}}\bar{\varphi}$, $\bar{\theta}$.

The correlation between the measured and the modeled indentation modules was determined by calculating the squared Pearson product-moment correlation coefficient r^2 of a linear dependence.

To investigate any significant differences of the measured indentation modulus, mineralization and fibril angle among the 2 donors, 4 cut angles or 3 morphological regions, a two-sided multifactor univariate variance analysis (ANOVA) is performed (Crawley, 2007).

6.4 Results

6.4.1 qBEI results

For 1707 measurement sites Γ_i, the local mineral volume fraction ${}^{\mathrm{mi,fa}}\varphi_i$ was evaluated. The distribution of the results can be seen in Fig. 6.4a. The mean value was 0.37±0.03 with a minimum of 0.32 and a maximum of 0.47. In terms of calcium weight fraction, the mean value was ${}^{\mathrm{ca,fa}}\psi_{\mathrm{mean}} = 0.25{\pm}0.02$.

6.4.2 qPLM results

At the same sites, the local fibril- or collagen angle θ_i relative to the sample surface was measured. The overall mean of 1701 values was $38.96° \pm 16.0°$ with angles between 0° and 77°. From this amount, 883 measurements were obtained from samples that were cut at 0° and contained therefore transversely sectioned osteons. The mean θ of this sub-population was $33.6° \pm 15.6°$ with a range of 0° to 73.3°. The histogram of this sub-population is shown in Fig. 6.4b.

6.4.3 Indentation and model results

After applying the filter procedure described in section (sec. 6.3.4), 1707 out of the originally 1881 indents were considered valid. The indentation modulus as a function of mineralization and the average collagen out-of-plane angle are shown in Fig. 6.5 and 6.6.

The obtained indentation moduli were averaged according to the procedure in (sec. 6.3.7), yielding a single value $\bar{\bar{E}}_{\mathrm{ind}}$ for each of the 57 indentation patterns. The same was performed for the local mineral volume fractions and fibril angles as well as the modeled indentation moduli resulting in 57 corresponding values (${}^{\mathrm{mi,fa}}\bar{\varphi}$, $\bar{\theta}$, $\bar{\bar{\tilde{E}}}_{\mathrm{ind}}$, $\bar{\bar{\tilde{E}}}^{\theta=0}_{\mathrm{ind}}$). The overall

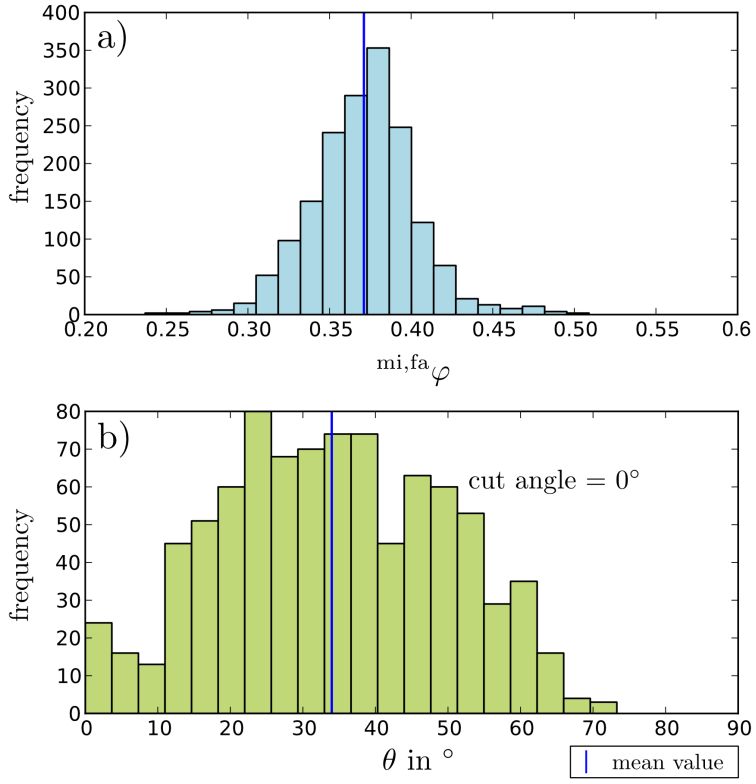

Figure 6.4: (a) Histogram of the measured local mineral volume fraction ${}^{\text{mi,fa}}\varphi_i$ (n=1707). (b) Histogram of the measured local fibril- or collagen angle θ_i relative to the sample surface for the samples that were cut at 0° to the femoral shaft (n=883).

means of this result variables are presented in Tab. 6.2. The means of the measured $\bar{E}_{\text{ind}}$ and the modeled indentation modules $\bar{\tilde{E}}_{\text{ind}}$, 22.6±4.02 GPa vs. 23.2±2.6 GPa, respectively were not significantly different with p=0.9 (Wilcoxon test), p=0.42 (paired t-test). The modeled indentation module with a fixed fibril angle at $\theta = 0°$ is higher at 26.5±2.05 GPa as this indent is aligned parallel to the stiff fibril direction.

6.4.4 Correlation

Four correlation analyses were performed between the measured indentation modules $\bar{E}_{\text{ind}}$ and their modeled counterparts $\bar{\tilde{E}}_{\text{ind}}$, $\bar{\tilde{E}}^{\theta=0}_{\text{ind}}$, the mineralization ${}^{\text{mi,fa}}\bar{\varphi}$ and the fibril angle $\bar{\theta}$ Tab. 6.2. The squared correlation coefficients r^2 were weak (<0.03), indicating no correlation between the variable pairs.

However, the correlation between the indentation measurements and the

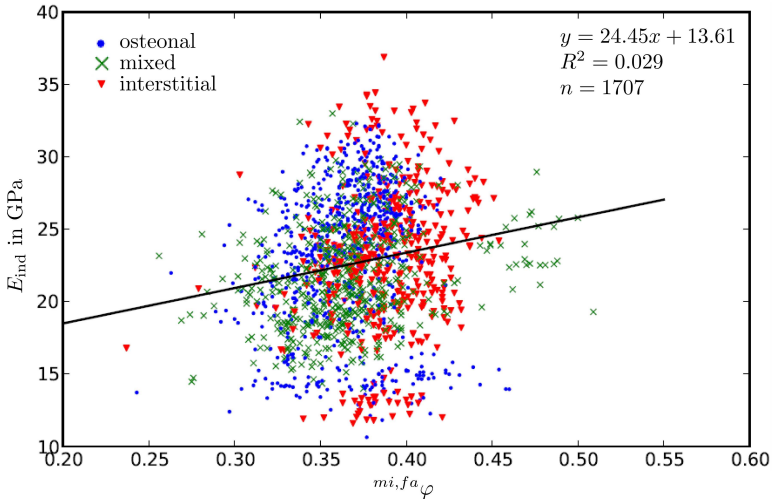

Figure 6.5: Indentation moduli (E_{ind}) as a function of mineral volume fraction ($^{\mathrm{mi,fa}}\varphi$) for the osteonal, mixed and interstitial regions.

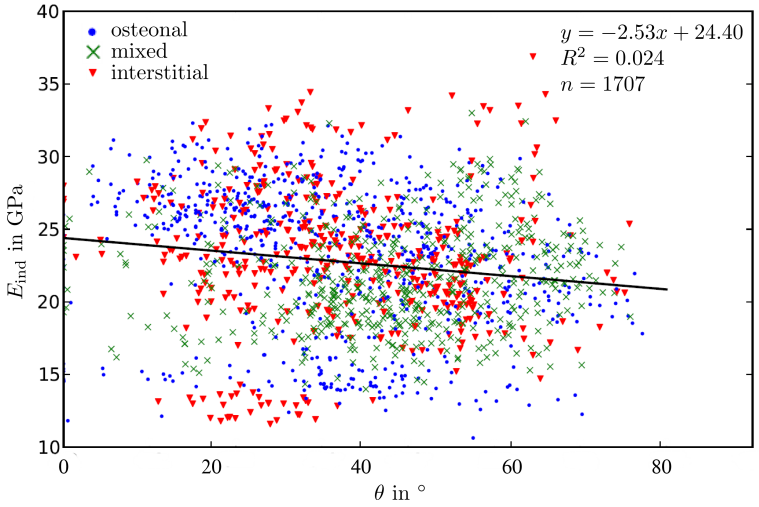

Figure 6.6: Indentation moduli (E_{ind}) as a function of the collagen out-of-plane angle (θ) for the osteonal, mixed and interstitial regions.

Var 1	Mean	Var 2	Mean	r^2 value
$\bar{E}_{\text{ind}}$	22.57±4.02 GPa	${}^{\text{mi,fa}}\bar{\varphi}$	0.37±0.02	0.016
$\bar{E}_{\text{ind}}$	22.57±4.02 GPa	$\bar{\theta}$	38.96°±12.03	0.026
$\bar{E}_{\text{ind}}$	22.57±4.02 GPa	$\bar{\tilde{E}}_{\text{ind}}^{\theta=0}$	26.53±2.05 GPa	0.014
$\bar{E}_{\text{ind}}$	22.57±4.02 GPa	$\bar{\tilde{E}}_{\text{ind}}$	23.23±2.55 GPa	0.026

Table 6.2: Squared Pearson correlation coefficient r^2 for the dependency of the measured indentation modules $\bar{E}_{\text{ind}}$ on: (1) the modeled indentation modulus $\bar{\tilde{E}}_{\text{ind}}$ including the local fibril orientation; (2) the modeled indentation modulus $\bar{\tilde{E}}_{\text{ind}}^{\theta=0}$ disregarding the fibril orientation; (3) the mineralization ${}^{\text{mi,fa}}\bar{\varphi}$; (4) the fibril angle $\bar{\theta}$. Additionally the respective means and standard deviations are listed.

model predictions increases from r^2 =0.014 to 0.026 when accounting for the local fibril orientation in the model. This increase in correlation is indeed significant with $p = 0.007$, as tested via a Wilcoxon rank test (corresponds to a paired t-test for not normally distributed samples).

Fig. 6.7 shows the comparison of $\bar{E}_{\text{ind}}$ and $\bar{\tilde{E}}_{\text{ind}}$ with a differentiation of the regions and cut angles. In none of the different regions or cut angles a clear correlation can be identified.

6.4.5 ANOVA results

Three two-way ANOVA analyses were executed with the cut angle and regions as factors and $\bar{E}_{\text{ind}}$, ${}^{\text{mi,fa}}\bar{\varphi}$ and $\bar{\theta}$ as response variables Tab. 6.3. Preliminary three-way ANOVA analyses identified the donor as non-significant factor. Thus the donor was not included as factor in the final statistics and two-way analyses were performed. Moreover, response values obtained from the *mixed* regions were excluded so that just the osteonal and interstitial values remained. In that way, statistical differences between these two regions could be examined more clearly.

The requirements on the data are fulfilled: the variances in the groups are similar, the response values are approximately normally distributed and independent. Only the ANOVA with the factor $\bar{E}_{\text{ind}}$ has groups with significantly different variances. Therefore this specific result has to be interpreted with care. The level of significance is set to $\alpha = 0.05$.

As seen in Tab. 6.3, the measured indentation modulus $\bar{E}_{\text{ind}}$ shows a slightly significant difference with the cut angle.

A post-hoc Tukey test reveals the differences to occur between the 0° and 45° as well as between the 0° and 60° cut angles. As expected, the fibril angle $\bar{\theta}$ is significantly different among the cut angles ($p = 0.0068$). Surprisingly, the mineralization ${}^{\text{mi,fa}}\bar{\varphi}$ is also significantly different between the different cut angles ($p = 6.08e - 06$).

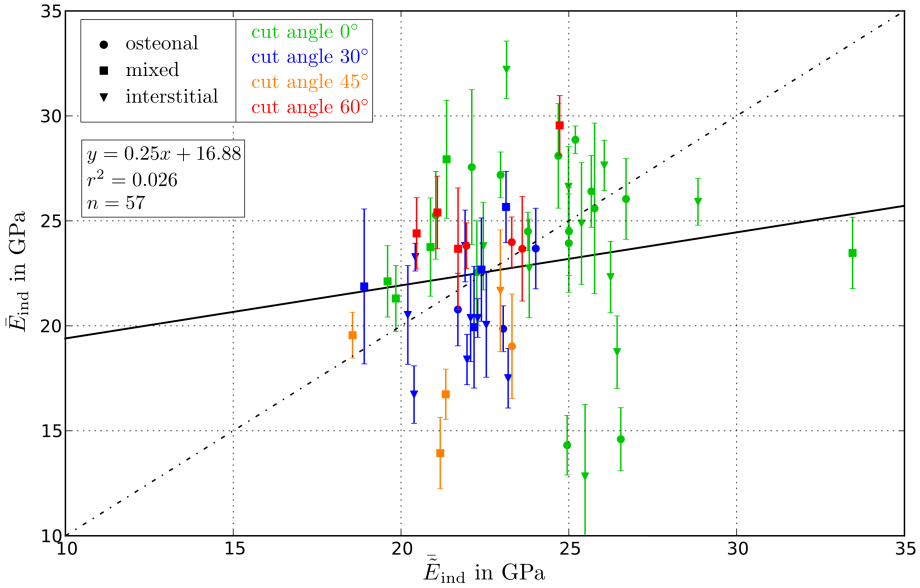

Figure 6.7: Correlation between the measured indentation modulus $\bar{E}_{\mathrm{ind}}$ and the prediction $\bar{\tilde{E}}_{\mathrm{ind}}$, that is based on the local tissue mineralization as well as on the local fibril orientation. The symbols indicate different regions where the indent patterns were placed. The colors display the angles at which the femoral samples were cut. The errorbars indicate the intra-pattern standard deviations of $\bar{E}_{\mathrm{ind}}$. The intra-pattern standard deviation of the predicted indentation moduli $\bar{\tilde{E}}_{\mathrm{ind}}$ was 3.17 GPa.

In neither ANOVA any significant coupling between the cut angles and the regions were found.

6.5 Discussion

This work involved testing the hypothesis that lamellar bone stiffness as measured by nanoindentation, can be expressed by local mineral mass fraction and local collagen orientation. Multiple experimental as well as numerical means were utilized in this study. Before approving or rejecting the hypothesis, the absolute measurement results are discussed.

The average measured mineral volume fraction of 0.37 ± 0.03 of the tested samples is slightly lower than the average in the literature. In Roschger et al. (2003) the normally mineralized bone showed a mineral volume fraction of about 0.43, similar to the results obtained by Ruffoni et al. (2007) with a mineral volume fraction of 0.45.

As the mineralization was shown not to be the absolute predictor of tissue

Response: $\bar{E}_{\mathrm{ind}}$	Df	Sum Sq	Mean Sq	F value	p value
cut angle	3	161.6	53.9	3.02	0.044*
region	1	0.11	0.1	0.0064	0.93
cut angle↔region	2	21.5	10.7	0.60	0.55
residuals	32	570.8	17.8		
Response: ${}^{\mathrm{mi,fa}}\bar{\varphi}$	Df	Sum Sq	Mean Sq	F value	p value
cut angle	3	0.0088	0.0029	13.79	6.08e-06*
region	1	0.0025	0.0025	11.90	0.0016*
cut angle↔region	2	0.00039	0.0002	0.93	0.41
residuals	32	0.0068	0.00021		
Response: $\bar{\theta}$	Df	Sum Sq	Mean Sq	F value	p value
cut angle	3	0.48	0.16	4.86	0.0068*
region	1	0.00068	0.00067	0.021	0.89
cut angle↔region	2	0.037	0.018	0.56	0.58
residuals	32	1.05	0.033		

Table 6.3: ANOVA results for $\bar{E}_{\mathrm{ind}}$, ${}^{\mathrm{mi,fa}}\bar{\varphi}$ and $\bar{\theta}$ depending on the cut angle (groups: 0°, 30°, 45°, 60°) and region (groups: osteonal, interstitial). Abbreviations: Degree of Freedoms (Df), Sum of Squares (Sum Sq), Mean Squares (Mean Sq). Significant relations are marked by a *, according to a level of significance of $\alpha = 0.05$

stiffness (especially for local trends), some work was done on evaluation of the effects of the average arrangement of the mineralized collagen fibrils on the stiffness (Ramasamy and Akkus, 2007; Bakbak et al., 2011). The average out-of-plane collagen angle θ measured in this study (on the 0° cut samples) was $33.6° \pm 15.6°$, which is in agreement with the literature. An acoustic microscopy study performed by Turner et al. (1995) showed the principle direction of collagen averaged over an approximately $60\mu m$ thick bone sections to be about 30°. Similar average arrangement of the fibrils was indirectly measured by Wagermaier et al. (2006) with a micro-beam x-ray diffraction method, with the difference that the arrangement of the mineral crystallites, not collagen fibrils, was measured. This result can be compared to the present study with the assumption that the mineral follows the collagenous matrix in the average arrangement. This is likely the case for the mineral placed within the collagenous fibrils, but the arrangement of the hydroxyapatite crystallites may be more random within the extrafibrillar spaces.

When looking on the distribution of θ measured on the 0°-samples in Fig. 6.4b it is striking that some few values reach 73° but no transversely oriented fibrils at $\sim 90°$ were observed at this resolution. This fact is not in line with the investigations of Ascenzi and Bonucci (1967, 1968) who proposed a class of *transverse* osteons with a main fibril orientation of $\theta = 90°$. However the θ-distribution of the current study is consistent with the investigations of Ascenzi et al. (2003) who reported two classes of osteons - a *dark* class with

a mainly axial fibril alignment and a *bright* class containing mainly fibrils aligned at $\sim 45°$.

In (Reisinger et al., 2011) the average fibril angle relative to the osteon axis, as evaluated by nanoindentation was reported to be around 10° - a value that was measured only at a few spots in the current study.

The average indentation modulus $\bar{E}_{\text{ind}}$ measured here was 22.6±4.02 GPa, which can be considered within the range of moduli measured by nanoindentation with similar final indentation depth seen in the literature. Franzoso and Zysset (2009) measured the average of 22.31±2.16 GPa with nanoindentation of osteons extracted from similar physiological location. Reisinger et al. (2011) measured 20.5 - 27.6 GPa, depending on the angular cut of an osteon (from transverse to axial direction of indentation with respect to the osteon main axis). Lower indentation moduli were measured with microindentation to final indentation depth of 2.5 μm by Wolfram et al. (2010a,b) ranging in indentation moduli 10.65±0.16GPa till 15.00±0.14GPa depending on the origin and direction in which the trabecular bone was indented. A certain indentation depth effect - a decrease of the measured indentation modulus with increasing indentation sampling volume, was observed in a variety of materials, also mineralized tissues (Swadener and Pharr, 2001; Zhang et al., 2008; Voyiadjis and Peters, 2010).

The average indentation modulus estimated with the fibril array model ($\bar{\bar{E}}_{\text{ind}}$ = 23.2±2.6 GPa) was not significantly different from the measured values (p=0.9), which suggests that the level of lamellar bone stiffness is predicted.

The correlation of mineralization to the measured indentation stiffness was weak with $r^2 = 0.016$, see Tab. 6.2, even weaker than the ones previously shown in the literature (Raum et al., 2006; Boivin et al., 2008; Follet et al., 2004; Zebaze et al., 2011). Hengsberger et al. (2002a) reported a r^2 of 0.42 for a 86 year old donor and, interestingly, a r^2 of 0.0 for a 30 year old donor suggesting an age dependence. Some encouraging results on the dependence of tissue mechanical properties on the collagen phase arrangement were presented (Ramasamy and Akkus, 2007), mixed with some discouraging ones (Bakbak et al., 2011).

Unfortunately, the expected improvement of correlation after considering the collagen arrangement was not very strong with r^2 increasing from 0.014 to 0.026. However the increase was statistically significant ($p = 0.007$). This suggests that there are other factors influencing the local tissue stiffness fluctuation. The hypothesis that lamellar bone stiffness, measured by nanoindentation, can be expressed by local mineral mass fraction and local collagen orientation, was *rejected*. Possible limitations that may influence the obtained correlation are now to be discussed.

In the present study, a part of the fibril-array model input parameters were kept constant during the analysis. In an auxiliary test, it was investi-

gated, if reasonable changes in the input parameters of Tab. 6.1 are able to explain the high variability of the measured indentation modulus for a specific mineralization. The highest span was observed at ${}^{\mathrm{mi,fa}}\varphi = 0.34$, where indentation modules E_{ind} between 10GPa and 35GPa were measured (difference of 25GPa). In the course of this check, the more argueable parameters, the mineral quota of total mineral in the fibrils and the fibril volume fraction in the fibril-array, were both varied between 0.25 and 0.75. The fibril orientation angle θ was varied between 0° and 90°. The variation was performed randomly using a Monte Carlo method. The resulting predicted indentation modulus $\tilde{E}_{\mathrm{ind}}$ ranged from 5GPa to 21GPa (difference of 16GPa), indicating, that the high local fluctuation of measured stiffness cannot be explained satisfactory by neither of the three investigated parameters.

An other reason for the low correlation might be the fact that the method of mineral content evaluation used here is non volumetric. The used qBEI technique correlates the mass fraction of calcium to the gray scale of the image acquired with the secondary electron imaging (Roschger et al., 1998). Depending on the architecture of the tissue and its porosity, possibly different volumes are tested pixel by pixel. If the nanoporosity (not resolved by the technique) varies within an image, this introduces errors in the mineral volume fraction estimation which are than transmitted to computation of the mechanical properties.

Besides the mineral quantification issues, undefined nanoporosity can influence the nanoindentation measurements. Pores in the indent-surface interaction zone soften the structure and lead to lower indentation modules. A site-mateched nanoporosity evaluation technique would be needed in order to overcome this problem.

In a study by Hengsberger et al. (2002a), samples from an elderly donor show a significantly lower indentation modulus than younger tissue. This fact might also be attributed to local microdamage concentrations that increase the variability of the measured stiffness values (Dall'Ara et al., 2010b). The donors in the present study were also quite elderly, so the used samples are prone to own inherent damage.

As qBEI and nanoindentation operate on the tissue surface, the surface related alterations due to the tissue preparation have to be considered. As shown in (Roschger et al., 1993), repeated wetting and drying introduces ultracracks in the tissue. This increase of porosity might lead also to local softening.

As shown in the ANOVA-analyses in Tab. 6.3, the fibril angle and the measured indentation modulus depend significantly on the angle of the sample surface relative to the femoral shaft, as expected. This fits to several other studies in which nanoindentation was performed in multiple directions, (Reisinger et al., 2011; Franzoso and Zysset, 2009; Fan et al., 2002; Ziv et al., 1996), and in which the osteonal fibril orientation was investigated (Weiner et al., 1997, 1999; Wagermaier et al., 2006; Ascenzi et al., 2003). The unfore-

seen dependence of the mineralization on the cut angle (p=6.08e-06) cannot be explained, though.

The significant difference in mineralization between the osteonal and interstitial regions (p=0.0016) is attributed to the local age of the tissue. In the ongoing mineralization process, the younger osteons are lower mineralized compared to the older interstitial regions (Boivin and Meunier, 2002).

The out-of-plane collagen angle evaluated here is an average over the specimen thickness (approximately $30 - 60\mu$m). This means that possibly different lamellae or also osteons are averaged, depending on the sample cut. In contrast, the indentation moduli describe the stiffness of the top surface of a sample (depth of approximately 500nm). So the discrepancies between the measured and predicted indentation moduli may be coming from variability of stiffness within the $30 - 60\mu$m sample thickness. Additionally, a periodic variation of the stiffness and/or collagen orientation between the adjacent lamellae might be contributing to the low correlations observed.

The uniaxial structure considered in the model could be seen as another limitation, as the material within a single lamella may not be uniaxially oriented and also the indentation deformation zones may fall in between of the lamellae. Although in some models like for example the one by Weiner et al. (1999) a lamella is formed by 5 layers of sublamellae of which each is an uniaxially oriented structure and a certain rotation angle between the sublamellae was measured. Approximately 80% of the lamella showed the out-of-plane collagen angle within 0° and 30°, which on average could be compared to the model presented here.

6.6 Conclusion

In this study, a method for a site-matched relation of the indentation modulus of bone to its local mineralization and fibril orientation is proposed. Results show that the variation of indentation modulus of human lamellar bone can not be explained by mineralization and orientation only, which points towards other factors such as nanoporosity or microdamage that are of possible influence. Beside this, there was no evidence for the class of transverse osteons in the obtained fibril angle distribution.

6.7 Acknowledgments

The authors thank the Austrian Science Fund (FWF) for grant support (Grant No. P19009-N20) and the Hochschuljubiläumsstiftung of Vienna for sponsoring a part of the used computational resources (Grant No. H-1906/2010). Additionally, the authors would like to thank Thomas Tangl for providing assistance with the sample preparation and Phaedra Messmer for assistance with the qBEI measurements.

Chapter 7

Conclusions

7.1 Summary of original contributions

Two zones of morphology in MTLT

In this thesis, a special focus was on mineralized turkey leg tendon, as this uniaxial tissue was used as a simplified structural model of mineralized collagen fibers. The tissue was widely studied as a model for collagen mineralization (Landis et al., 1996; Silver et al., 2001, 2000), as well as a mechanical model of the fibers (Gupta et al., 2004). Tendons of younger animals (age below 24 weeks) showed separated unmineralized and mineralized fibers (or fiber bundles) as visualized with quantitative electron microscopy (qBEI).

In the course of this thesis, two different types of morphology of MTLT were noted and described (details in Chapter 2). One of the zones, called the circumferential zone, showed smaller fiber diameters and more dense fiber packing. The other - the interstitial one, showed more sparse fibers packing, implying more microporosity. Mineralization, fraction of organic phase and microporosity were different for the two zones. The mean field homogenization models proved to be useful in predicting the stiffness in the two phases based on their morphological features. The distribution of the mineral between the collagen fibrils and extrafibrillar matrix predicted with this model is different for the two zones, as well. According to these predictions, more mineral is placed within the fibrils in the circumferential zone: 55-90%. In the interstitial zone, a fraction below 55% is predicted.

Quantification of the extent of elastic anisotropy in MTLT

Much indentation (both nano- and microindentation) work has been done on mineralized tissues so far (Hengsberger et al., 2002b; Oyen, 2006; Ebenstein and Pruitt, 2006; Donnelly et al., 2006; Lewis and Nyman, 2008; Franzoso and Zysset, 2009; Wolfram et al., 2010a; Zhang et al., 2010; Reisinger et al., 2011) and it has become a state of the art technique in evaluation of elastic

properties of these materials. Some works addressed the degree of elastic anisotropy of bone (Wolfram et al., 2010a; Reisinger et al., 2011). The arrangement of mineralized collagen fibers in bone is known to be complex and there is still some dispute of the details of this arrangement. One of the things agreed for is that bone is built up by mineralized collagen fibers. Those are also present in MTLT, with the advantage of the uniaxial arrangement. In the course of this thesis the degree of anisotropy of such fibers was quantified in dried and re-hydrated conditions, ranging the maximal degree of anisotropy among the mineralized tissues (1.60-2.10 in dried and 4.20-4.50 in re-hydrated state). This could be expected based on the uniaxial arrangement of the fibers in MTLT.

Transverse swelling of MTLT An important issue has to be emphasized that was noted during the quantification of the elastic anisotropy extent in MTLT. The sample surfaces preparation (two-orthogonal surfaces of a sample) involves sample cutting and polishing. This may introduce artifacts, as the fibers are embedded fresh (without dehydration and infiltration with the embedding resin). The free fibers, no more constrained in one of the directions (normal to the cut surface) may swell when subjected to diffusion of water. The microindentation experiments presented in this work were performed in dried and also re-hydrated conditions. An intensive sample swelling was noted in the transverse direction of indentation (the case of the longitudinal fibers laying in the plane of sample surface). The indentation results in this directions are likely underestimated due to sample surface detection problems during the indentation experiments and also the volume fraction of the swollen sample tested, which is likely much lower than the one tested in the dried state.

Factors determining macroscopic elastic properties of MTLT

A study validating macroscopic tensile testing of MTLT samples and μFE modeling of the same loading case was conducted (see Chapter 5). Different methods of obtaining the elastic properties of MTLT assigned to the elements were used. Nevertheless, the major factor influencing the macroscopic response of MTLT was porosity, explaining over 90% of the variability between the samples.

Calibration of quantitative polarized light microscopy

The polarized light technique, used before for assessment of the organization of collagen fibers in mineralized tissues in a non-quantitative way (Boyde and Riggs, 1990; Martin et al., 1996; Kalmey and Lovejoy, 2002; Goldman et al., 2003; Ramasamy and Akkus, 2007) was brought to a level of a quantitative technique in the frame of this thesis. A calibration on the uniaxial mineral-

ized tendon samples cut at a variety of angles allowed for formulation of a calibration equation relating the phase factor (dependent on birefringence) to the fiber out-of-plane angle. This relationship was applied to evaluation of average collagen arrangement in osteonal bone thin sections, see Chapter 3. The system used in the technique does not require any complicated set-up and has therefore the potential of becoming a accessible tool of quantification of collagen arrangement in mineralized tissues.

Site-matched qBEI, qPLM, NI, modeling of mineralized collagen fibers

A site matched assessment of mineralization, collagen arrangement and indentation stiffness measured experimentally and predicted with a mean field homogenization model was performed on osteons from human mid-shaft. An attempt of combining those in order to understand the structure-function relationships in bone was not performed before.

7.2 General discussion

MTLT as a model for bone: pro & contra

MTLT was used throughout the study, as a model of mineralized collagen fibers, also present in bone. No specific claims stating that MTLT is a proper model for bone tissue were made. Nevertheless the tissue was used as a simple mineralized tissue on which some procedures can be validated (as for example the calibration of quantitative polarized light microscopy). Considering the advantages of MTLT as a model of mineralized collagen fibers we have to stress the similarity of the overall composition being mineral, collagen type I and water (pores). Of course the minor constituents of the two tissues and their relative fractions may differ strongly. For example some of the non-collagenous proteins (eg. proteoglycans) may be different. Additionally the collagen cross-linking patterns may be different, between bone and MTLT, as well as between the two phases of morphology in MTLT.

The main advantage of MTLT over bone is its simple uniaxial arrangement of the fibers. The arrangement of the fibers in bone is much more complex, and not fully understood. In this sense MTLT is a good mechanical model for testing different hypothesis and validation of models (eg. FE models), with one less factor influencing for example stiffness (no orientation effects need to be taken into account).

The fibrillar structure of MTLT is likely very similar to this of bone. The tripe-helical collagen molecules are assembled in a similar manner (Freeman and Silver, 2004; Knott et al., 1997), stabilized by cross-links and later infiltrated to some extent by mineral platelets and also embedded in the extrafibrillar mineral. Actually many of the works describing the relation-

ships of mineral and collagen in the fibrils were done on MTLT and than the results were used in interpretation of the situation in bone tissue (Lees et al., 1994).

An additional aspect is the mineralization pattern which is likely different in bone and MTLT. Especially the interstitial zone of MTLT, where the already existing large collagen fibers are being mineralized with time. It is likely that less mineral can penetrate into the fibrillar structures and possibly higher fraction of extrafibrillar mineralization is accumulated there. In bone the mineralization process begins directly after the new collagenous matrix is laid down. This could result in a higher fraction of mineral interpenetrating the fibrils. The fact of the circumferential zone being a result of modeling (remodeling) of the tissue was suggested in Chapter 2. This fact needs to be verified using biochemical/histochemical evidence showing cell or fluorochrome labels depicting sequential timepoints.

As widely discussed throughout this thesis, the mineral distribution parameter may be different in MTLT as compared to bone. An interesting fact noticed during the ashing experiments may be mentioned here. Six MTLT samples were ashed in the course of the study in order to quantify the fraction of organic matter. Interestingly, the samples after ashing (without the organics content) sustained their integrity, could be handled, preserved their shape and volume. This is not the case in bone samples, which tend to disintegrate after ashing. As the approximate composition of the two examples is similar, it is likely that the arrangement of the phases is responsible for this behavior. MTLT with its uniaxial fibers arrangement would be expected to be less integrated than for example lamellar bone, where the fibers are oriented in multiple directions. It is nevertheless MTLT that keeps the integrity. The reason may be one level of the hierarchy lower - at the level of mineralized fibrils. The structure is likely more stable to ashing if more mineral is outside of the fibrils, creating a sort of a porous scaffold of the extrafibrillar mineral in which the (intrafibrilar) mineralized collagen fibrils are placed. This would suggest also that more mineral is placed within the collagen fibrils in bone than in MTLT.

Also another sample preparation artifact suggested a morphological feature in MTLT, namely the “tearing” artifacts present in microtoming of thin sections of longitudinal samples of MTLT (see Fig. 2.2 e, f). This type of preparation of undecalcified tissue is challenging for bone and no completely non-torn sections could be achieved in MTLT. This suggests that the binding of the fibers in this tissue is weaker than in bone. Here, also the fiber arrangement may be a factor.

Anisotropy of MTLT vs bone

The hypothesis of the indentation part of this study was that the elastic anisotropy ratio in MTLT is the highest among mineralized tissues. This

hypothesis was proved with nano- and microindentation performed in dried and re-hydrated conditions. The average elastic anisotropy ratio measured in dried case of microindentation ranged from 1.99-2.10 depending on the morphological zone. This is much higher than was measured on trabecular bone of vertebral bodies by Wolfram et al. (2010a), which resulted in average of 1.43. This could be explained with the uniaxial arrangement of the mineralized collagen fibers in MTLT. The indentations were performed only in two orthogonal planes - axial and transverse to the tendon's main axis, so the unlikely possibility of having the stiffest direction at an angle between the two might have been overlooked. This was the case for bone samples, which elastic anisotropy was studied with acoustic microscopy (Hasegawa et al., 1994) in two directions. The conclusion of little directionality of collagenous matrix was then rejected in a similar acoustic microscopy study, in which the bone samples were cut at 10^o increments between the axial and transverse direction Turner et al. (1995). A similar study performed on angular cuts of the two zones of MTLT: intact, demineralized and decollagenized could provide some interesting structural information, as for example the directionality of mineral in the two zones based on its elastic anisotropy. This could verify our findings of the mean field homogenization model about the fraction of mineral placed within or outside of the fibrils, assuming higher degree of organization of the mineral penetrating the fibrils, as compared to the extrafibrillar one.

Indentation - limitations

Nano- and microindentation techniques were the ones chosen for evaluation of elastic properties at the microscale for this thesis. The techniques were validated and widely used for mineralized tissues, as described in 1.3.1. Nevertheless, there are some limitations of the technique.

One of the technique's limitations is the depth trend - increasing measured indentation modulus value with decreasing final indentation depth. This effect is partially understood in bulk microcrystalline or single-crystal materials, where two types of indentation size effects were noted (Gouldstone et al., 2007). The first one is observed for indentations lead till the final depth maximum of 400nm and is manifested with a step (or a "pop-in") in the loading curve. Interestingly, this phenomena occurs at a load that corresponds to theoretical shear strength of the specimen (Gouldstone et al., 2007). The other effect occurs at indentation depths higher than 400nm and is manifested with continuous decrease of modulus with increasing indentation depth. This issue is not yet resolved quantitatively, even though some modeling attempts were done (Begley and Hutchinson, 1998; Shu and Fleck, 1998). Some phenomenological explanation of this effect by relating the final indentation depth to the dislocations spacing in metals, were given (Voyiadjis and Peters, 2010). The effect was noticed also in het-

erogeneous materials, including mineralized tissues (Zhang et al., 2008) and is likely caused by damage accumulation under the indenter's tip, which is higher for larger indentation depths.

Mineral quantification - limitations

Mineralization of a tissue is one of the main factors determining its stiffness (Reisinger et al., 2010). Among the techniques applied in quantification of mineral content of bones, the most popular are quantitative backscattered electron imaging (qBEI, see Section 6.3.2), (micro) computed tomography and microradiography. The advantage of the two last methods is that they provide volumetric information of the mineral fraction. qBEI provides high resolution of the mineralization content, but in terms of the mass fraction. Transformation of the calcium (recalculated using stoichiometric relationships to mineral) weight fractions to the volume fractions is somewhat troublesome. Porosity (nano- and microporosity) non resolved by the technique is included in the resulting mineral values, which has no impact on mass fraction, but does have an impact on volume fraction. To overcome this problem a direct site-matched assessment of nanoporosity would be required. In the literature, the mass fractions are often cited in comparative studies, where this issue is not critical. Quantification of mineral volume fraction becomes an important issue in modeling of the fibers at lower lengthscales. A possible solution of the issue for MTLT samples was suggested in Chapter 2. A high resolution volumetric method would be needed in order to provide quantitative information, in this sense, microradiography is suitable, but the sample preparation and the accessibility of the technique are the limitations.

Collagen arrangement quantification - limitations

The quantitative polarized light microscopy (qPLM) technique was developed in the course of this thesis and calibrated for the universal quantitative use in assessment of the average out-of-plane collagen angle (see Chapter 3). The limitation in the use of the technique is the fact that the information about the collagen arrangement is averaged over the sample thickness, typically 30 - 60μm. In lamellar bone this may mean that the angle is averaged over more than one lamellae or even more osteons, depending on the sample cut and the variability of organization at the site. This information may not be sufficient to understand the arrangement of the fibers in mineralized tissues with a high resolution. The solution could be development of protocols resulting in thinner bone slices, which could be obtained with for example microtoming technique. Nevertheless, the in-plane resolution is also limited to about 1 micron, which is comparable to a sublamellae thickness, so the variation of the collagen orientation within a lamella might be resolved properly. Additionally, this technique should be confronted with another

one, for example Raman spectroscopy for cross-calibration.

Bone structure-function relationships: other factors

In Chapter 6 the hypothesis that the indentation stiffness of lamellar bone can be locally predicted with the mineralization and collagen fibers arrangement was tested. The correlation between the measured indentation stiffness and the one predicted with these morphological parameters used in the mean field model was low, indicating that there are other factors that are important in determination of stiffness like nanoporosity, collagen cross-linking patterns, non-collagenous proteins and others.

The limitations mentioned above may also contribute to increase the deviation of the parameters predicted (mineralization, collagen arrangement) with the error being transferred to the mean field model used for the stiffness prediction.

7.3 Outlook

In the scope of this thesis, the structure-function relationships in mineralized tissues were accessed using experimental and computational methods. Some interesting results helping understand the performance of mineralized tissues were obtained, but were limited to the elasticity. Future work should include the post-yield properties of mineralized tissues in correlation with their morphological characteristics.

Additionally, there are a few points that could be investigated in order to confirm (or reject) the hypothesis stated in this thesis, as:

- Obtaining biochemical/histochemical evidence showing cells involved in (re)modeling of MTLT or fluorochrome labels showing sequential timepoints.

- Increasing the z-direction resolution of the quantitative polarized light microscopy technique by development of a protocol for producing thin ($\sim$10μm) embedded sections of bone, in order to quantify the extent of the error resulting from the averaging over the $\sim$30-60μm thickness.

- Cross-calibration of the polarized light technique with another one that measures collagen fiber orientation, for example Raman spectroscopy (Gamsjaeger et al., 2010).

- Testing the influence of nanoporosity on the measured indentation modulus in inhomogeneous media, as bone or MTLT. Development of a protocol for a site-matched assessment of micro- and nanoporosity on mineralized tissues slices (for example using scanning laser confocal microscopy of stained bone sections as in (Kerschnitzki et al., 2011)).

- Investigation of damage accumulation in indentation experiments and its relation to the final indentation depth.

List of Figures

1.1 An overview of the hierarchical structure of bone. Image modified from Rho et al. (1998). 4
1.2 A scheme of extraction of the digital tendons from domestic turkey's legs. 6
1.3 An indentation imprint of a Berkovich indenter in axial direction of MTLT sample imaged with the indentation tip used in scanning probe microscopy mode of the TriboIndenter, Hysitron, USA. 9
1.4 An exemplary indentation curve involving a loading, holding and unloading phases. 9
1.5 A scheme of the electron beam (PE - primary electrons) interaction with a sample surface resulting in backscattering of the electrons (BSE - backscattered secondary electrons). a) beam interaction with a standard hydroxyapatite material and the grey levels difference between the resin and mineral. b) bone tissue with a distribution of the grey values. Image from Roschger et al. (1995) 12
1.6 An example of calcium weight fraction evaluation on a human bone. Image adapted from Roschger et al. (1998). 13
1.7 Birefringence patterns of osteons with different morphotypes. Letters in the top corners contain the original scale by Martin (Martin et al., 1996). The bottom corners contain the updated scale by Skedros et al. (2009). Image from (Skedros et al., 2009). 14
1.8 Schematic representation of the circular and linear polarizers set-up. Light source in red, CP - circular polarizer, ϕ - extinction angle, in blue - a sample, LP - linear polarizer, α - angle of the polarizer orientation. 15
1.9 The homogenization scheme involving two levels of tissue hierarchy: first step of homogenization involves modeling of a mineralized collagen fibril and the extrafibrillar matrix. Than the two are assembled in order to model a mineralized collagen fibril array. Image from Reisinger et al. (2010). 17

1.10 An example of von Mises stresses distribution in a sample of MTLT tested in tension. 18

2.1 Graphical representation of the fiber array consiting of mineralized collagen fibrils, mineralized extrafibrillar matrix and micropores. Fibrils consist of collagen and intrafibrillar mineral, and the matrix consists of extrafibrillar mineral and nanopores. Microindentation imprint averaging the properties of a fiber array is schematically represented in white. The proportions are not preserved 27

2.2 Light microscopy images of transverse and longitudinal sections of MTLT: a) a cross-section of MTLT showing different organization of the mineralized collagen fibers in the two morphology zones. Bar - 100μm. b) ciraumferential zone with smaller average fiber diameter and denser packing (on the right), interstitial zone with larger, more loosely packed fibers (on the left). Bar - 10μm. c) Tenocytes placed along the collagenous fibers in ciraumferential zone. Bar - 40μm. d) The tenocytes show high similarity to osteocytes. The lacunocanalicular system is present. Bar - 10μm. e) Nonmineralized tissue is observed at the peripheries of the tendon and in the vicinity of blood vessels (stained red with the Goldner's trichrome stain). Bar - 100μm. f) Non-mineralized collagen fringes around a vascular canal (ciraumferential zone) resemble a bone matrix at a forming site of bone (osteoid). Bar - 25μm 32

2.3 Quantitative backscattered electron images of transverse and longitudinal sections of MTLT. a) Transverse section taken from a proximal part. Uniformly mineralized, large fibers are present, no remodeling sites or ciraumferential zones are present. Bar - 50μm. b) More distal part of a mineralized tendon (older mineral deposits present there). Two types of morphologies can be observed: the ciraumferential region - around the large pores - showing lower mineralization and the interstitial zone with larger, more spread fibers and higher mineralization - resembling the type of morphology seen in vicinity to the mineralization front. Highly mineralized lines resembling the cement lines are visible at the borders between the morphology types. Bar - 50μm. c) A structure resembling a resorption cavity. Bar - 50μm. d) Interstitial zone with distinguishable mineralized collagen fibers. Bar - 15μm. e) Longitudinal section of MTLT showing the two types of the tissue (interstitial on the top and the ciraumferential on the bottom). Bar - 50μm. f) Longitudinal section of MTLT. Cells of different geometries are observed in the two morphology zones. Cuboidal tenocytes are present in the interstitial part of tendon (bottom), while in the ciraumferential regions, the cells resemble osteocytes. Bar - 25μm 33

2.4 Indentation moduli predicted with the fiber array model (dependend on mineralization, porosity and mineral distribution parameter α) as a function of α for the ciraumferential (CIR com) and interstitial (INT com) zones of MTLT. Additionally the experimentally obtained indentation moduli in the two zones (CIR exp, INT exp) with one standard deviation is plotted 35

3.1 Samples extraction scheme and the resulting $|\sin(\delta)|$ false-colored images. 45

3.2 Calibration curve describing relationship between the collagen out-of-plane fibers angle θ and the measured phase factor δ. Errorbars in the δ/L represent one standard deviation. Sample cut angles θ were accurate within about 5^o. 47

3.3 Collagen out-of-plane angles θ evaluated using the calibration curve on a mid-shaft of human femur. Bar 100μm. 48

4.1 Circumferential (CIR) and interstitial (INT) zones of MTLT in two orthogonaldirections (axial - AXI and transverse - TRV) as seen by backscattered electron imaging (a-d) and scanning probe microscopy (e-f). a, b) Bar - 50 μm; c, d) Bar - 25 μm; e, f) Bar - 5 μm. 54

4.2 MTLT two-directional sample extraction scheme resulting in axial (AXI) and transverse samples (TRV). MTLT is schematically represented as mineralized collagen fibers arranged longitudinally along the tendons main axis (z). 56
4.3 Re-hydration effects on microindentation moduli evaluated separately in the two morphology zones circumferential (CIR) and interstitial (INT). Indentation moduli were measured in dried (DRY) and re-hydrated conditions (WET), in the two orthogonal directions (AXI, TRV). The level of significance noted in the figure (*) is $p < 0.05$. The horizontal solid bars represent medians, the top/bottom border of the box represents the interquartile range. Whiskers represent maximum/minimum value. 59
4.4 a) Microindentation plastic work (W_{pl}) measured in dried (DRY) and re-hydrated (WET) conditions, in the two orthogonal directions (AXI, TRV), in the two morphology zones (CIR, INT), b) ratio of elastic to plastic work (W_{el}/Wpl). The level of significance noted in the figure (*) is $p < 0.05$. The horizontal solid bars represent medians, the top/bottom border of the box represents the interquartile range. Whiskers represent maximum/minimum value. 60
4.5 Nanoindentation results in the two morphology zones (CIR, INT), dry indentation in two directions (AXI, TRV). The level of significance noted in the figure (*) is $p < 10^{-6}$. The horizontal solid bars represent medians, the top/bottom border of the box represents the interquartile range. Whiskers represent maximum/minimum value. 61
4.6 Transverse-isotropic stiffness tensors estimated from the average indentation moduli in two orthogonal directions for the dried conditions micro- and nanoindentation in MTLT (fibers arranged along the z-axis, vertically). 62

5.1 Design of the study: the macrolevel validation scheme involved macroscopic tensile tests (a) and μFE modeling (c). Experimental (S_{exp}) and predicted ($S_{\mu FE}$) macroscopic stiffness were compared. At the microlevel, the indentation modulus measured with microindentation ($^{ind}E_{exp}$, b) was compared to the indentation modulus predicted with the mean field fiber array model ($^{ind}E_{FB}$, d). 68
5.2 Comparison of indentation moduli obtained experimentally $^{ind}E_{exp}$ with microindentation and predicted with the fiber array model $^{ind}E_{FB}$ for circumferential (CIR) and interstitial (INT) zone. 73

5.3 Comparison of stiffness obtained with microscopical tension tests and predicted with μFE simulation with elastic properties of the elements obtained from the fiber array model (FB input) and indentation (NI input). 76

6.1 Study design and sample preparation. Seven femoral bone slices were obtained from two different donors at 4 cut angles (0°, 30°, 45°, 60°) relative to the shaft axis. The slices were imaged by qBEI and qPLM and then indented in three regions (OSTeonal, INTerstitial, MIXed). Light microscope images of the indented sites were taken. 82

6.2 Site-matched image analysis. (a) 57 indent patterns are distributed on osteons (ost), the interstitial zones (int) and in not clearly identifiable regions (mix). (b) The position (x_i, y_i) of each indent i is assessed by light microscope images. (c) Calibrated qBEI images of the indentation zone, displaying the tissue mineral volume fraction ${}^{\mathrm{mi,fa}}\varphi(x, y)$, are registered to the light microscope images. The average ${}^{\mathrm{mi,fa}}\varphi$ in the indent-surface interaction zone Γ_i is used to model the local bone tissue stiffness tensor $\mathbf{E}_i$. (d) Calibrated qPLM images of the indentation zone, displaying the local fibril angle $\theta(x, y)$ relative to the sample surface normal, are registered to the qBEI- and light microscope images. The average fibril angle in the indent-surface interaction zone Γ_i is used to model an appropriately oriented indent into the material $\mathbf{E}_i$ yielding $\tilde{E}_{\mathrm{ind},i}$. 84

6.3 Mean field model representations of bone micro- and nanostructures and multiscale workflow: (a) fibril structure is modeled as a composite with prolate isotropic mineral spheroids unidirectionally embedded in an isotropic collagenmatrix; (b) extra-fibrillar mineral-protein network is modeled as a mineral foam with spherical voids; (c) fibril-array is built of highly elongated prolate spheroids of fibril material, embedded in extra-fibrillar matrix material; (d) output is the transverse isotropic stiffness tensor of the fibril-array 87

6.4 (a) Histogram of the measured local mineral volume fraction ${}^{\mathrm{mi,fa}}\varphi_i$ (n=1707). (b) Histogram of the measured local fibril- or collagen angle θ_i relative to the sample surface for the samples that were cut at 0° to the femoral shaft (n=883). . . 89

6.5 Indentation moduli (E_{ind}) as a function of mineral volume fraction (${}^{\mathrm{mi,fa}}\varphi$) for the osteonal, mixed and interstitial regions. 90

6.6 Indentation moduli (E_{ind}) as a function of the collagen out-of-plane angle (θ) for the osteonal, mixed and interstitial regions. 90

6.7 Correlation between the measured indentation modulus $\bar{E}_{\mathrm{ind}}$ and the prediction $\bar{\tilde{E}}_{\mathrm{ind}}$, that is based on the local tissue mineralization as well as on the local fibril orientation. The symbols indicate different regions where the indent patterns were placed. The colors display the angles at which the femoral samples were cut. The errorbars indicate the intra-pattern standard deviations of $\bar{E}_{\mathrm{ind}}$. The intra-pattern standard deviation of the predicted indentation moduli $\bar{\tilde{E}}_{\mathrm{ind}}$ was 3.17 GPa. 92

List of Tables

2.1 Nomenclature used in this manuscript was defined in a way that ϕ stands for volume fraction and ψ for mass fraction. The first part superscript means the quantity described (mi - mineral, col - collagen, org - organics, Ca - calcium, p(nano) - nanoporespores, p(micro) - micropores). The second part of the superscript (after a comma) means the quantity over which the fraction is calculated (fi - fibrils, fb - fiber array). Additionally subscript cir or int refers to the circumferential or interstitial zones. 26

2.2 Morphological parameters of the fibril and fiber arrays in the two zones of MTLT. ${}^{mi,fi}\psi$ - mass fraction of mineral in the solid constituents of MTLT - no porosity considered, ${}^{mi,fi}\phi$ - volume fraction of mineral in the solid constituents of MTLT - no porosity considered, ${}^{col,fb}\phi$ - volume fraction of the collagen in the fiber array, ${}^{fl,fb}\phi$ - volume fraction of the fibrils in the fiber array, ${}^{ind}E(exp)$ - average indentation modulus in axial direction with standard deviation (STD), ${}^{ind}E_{fb}(com)$ indentation modulus in axial predicted with the mean field model and α - mineral distribution parameter between fibrils and extrafibrillar matrix. Indentation moduli are given in GPa, mass and volume fractions, as well as α are dimensionless 34

4.1 Extent of anisotropy measured with nano- and microindentation in two orthogonal directions, in dried (DRY) and rehydrated (WET) conditions. Average indentation moduli in axial (${}^{ind}E_{axi}$) and transverse direction (${}^{ind}E_{trv}$), as well as standard deviations (in brackets), are given in GPa. CIR stands for the circumferential and INT for the interstitial zone. 63

5.1 Summary of the input paramaters in the fiber array model. The top part of the table shows the parameters, which were taken from literature. The bottom part shows results obtained in this study and used as input for the mean field fiber array models. 74
5.2 Validation of the fiber array model at the microlevel. ${}^{ind}E_{exp}$ - indentation modulus measured in axial direction with standard deviation in brackets (STD), ${}^{ind}E_{FB}$ - indentation modulus in axial direction predicted with the mean field model, α - mineral distribution parameter showing the fraction of mineral placed within collagen fibrils. 75
5.3 Comparison of the macroscopic stiffness S with standard deviation in brackets (STD) obtained with the tensile tests and μFE simulations with the elements stiffness obtained with the mean filed models for a given α - mineral distribution parameters. 76

6.1 Set of input parameters for the fibril-array model of Reisinger et al. (2010). 86
6.2 Squared Pearson correlation coefficient r^2 for the dependency of the measured indentation modules $\bar{E}_{\text{ind}}$ on: (1) the modeled indentation modulus $\bar{\tilde{E}}_{\text{ind}}$ including the local fibril orientation; (2) the modeled indentation modulus $\bar{\tilde{E}}^{\theta=0}_{\text{ind}}$ disregarding the fibril orientation; (3) the mineralization ${}^{\text{mi,fa}}\bar{\varphi}$; (4) the fibril angle $\bar{\theta}$. Additionally the respective means and standard deviations are listed. 91
6.3 ANOVA results for $\bar{E}_{\text{ind}}$, ${}^{\text{mi,fa}}\bar{\varphi}$ and $\bar{\theta}$ depending on the cut angle (groups: 0°, 30°, 45°, 60°) and region (groups: osteonal, interstitial). Abbreviations: Degree of Freedoms (Df), Sum of Squares (Sum Sq), Mean Squares (Mean Sq). Significant relations are marked by a *, according to a level of significance of $\alpha = 0.05$ 93

Bibliography

Akkus, O., 2005. Elastic deformation of mineralized collagen fibrils: An equivalent inclusion based composite model. Journal of Biomechanical Engineering 127, 383–390.

Arsenault, A., 1988. Crystal-collagen relationships in calcified turkey leg tendons visualized by selected-area dark field electron microscopy. Calcified Tissue International 43, 202–212. 10.1007/BF02555136.

Ascenzi, A., Baschieri, P., Benvenuti, A., 1994. The torsional properties of single selected osteons. Journal of Biomechanics 27, 875–884.

Ascenzi, A., Bonucci, E., 1967. The tensile properties of single osteons. The Anatomical Record 158, 375–386.

Ascenzi, A., Bonucci, E., 1968. The compressive properties of single osteons. The Anatomical Record 161, 377–391.

Ascenzi, A., Bonucci, E., 1976. Mechanical similarities between alternate osteons and cross-ply laminates. Journal of Biomechanics 9, 65–71.

Ascenzi, M.G., Ascenzi, A., Benvenuti, A., Burghammer, M., Panzavolta, S., Bigi, A., 2003. Structural differences between and isolated human osteonic lamellae. Journal of Structural Biology 141, 22 – 33.

Ascenzi, M.G., Lomovtsev, A., 2006. Collagen orientation patterns in human secondary osteons, quantified in the radial direction by confocal microscopy. Journal of Structural Biology 153, 14–30.

Bakbak, S., Kayacan, R., Akkus, O., 2011. Effect of collagen fiber orientation on mechanical properties of cortical bone. Journal of Biomechanics 44, 11–11.

Balooch, M., Habelitz, S., Kinney, J., Marshall, S., Marshall, G., 2008. Mechanical properties of mineralized collagen fibrils as influenced by demineralization. Journal of Structural Biology 162, 404–410.

Bayraktar, H.H., Keaveny, T.M., 2004. Mechanisms of uniformity of yield strains for trabecular bone. Journal of Biomechanics 37, 1671–1678.

Begley, M.R., Hutchinson, J.W., 1998. The mechanics of size-dependent indentation. Journal of the Mechanics and Physics of Solids 46, 2049–2068.

Berke, P., Tam, E., Delplancke-Ogletree, M.P., Massart, T., 2009. Study of the rate-dependent behavior of pure nickel in conical nanoindentation through numerical simulation coupled to experiments. Mechanics of Materials 41, 154–164.

Bigi, A., Gandolfi, M., Koch, M.H.J., Roveri, N., 1996. X-ray diffraction study of in vitro calcification of tendon collagen. Biomaterials 17, 1195–1201.

Bigley, R.F., Griffin, L.V., Christensen, L., Vandenbosch, R., 2006. Osteon interfacial strength and histomorphometry of equine cortical bone. Journal of Biomechanics 39, 1629–1640.

Bini, F., Marinozzi, A., Marinozzi, F., PatanĂ¨, F., 2002. Microtensile measurements of single trabeculae stiffness in human femur. Journal of Biomechanics 35, 1515–1519.

Birk, D., Zycband, E., Woodruff, S., Winkelmann, D., Trelstad, R., 1997. Collagen fibrillogenesis in situ: Fibril segments become long fibrils as the developing tendon matures. Developmental Dynamics 208, 291–298.

Blouin, S., Thaler, H., Korninger, C., Schmid, R., Hofstaetter, J., Zoehrer, R., Phipps, R., Klaushofer, K., Roschger, P., Paschalis, E., 2009. Bone matrix quality and plasma homocysteine levels. Bone 44, 959–964.

Boivin, G., 1984. Methods of calcified tissue preparation. Elsevier Science Publishers B.V. , 391–412.

Boivin, G., Bala, Y., Doublier, A., Farlay, D., Ste-Marie, L.e., 2008. The role of mineralization and organic matrix in the microhardness of bone tissue from controls and osteoporotic patients. Bone 43, 532–538.

Boivin, G., Meunier, P., 2002. The degree of mineralization of bone tissue measured by computerized quantitative contact microradiography. Calcified Tissue International 70, 503–511. 10.1007/s00223-001-2048-0.

Born, M., Wolf, E., 1999. Principles of optics. Cambridge University Press, Cambridge, UK.

Boskey, A., Pleshko Camacho, N., 2007. Ft-ir imaging of native and tissue-engineered bone and cartilage. Biomaterials 28, 2465–2478.

Bouxsein, M.L., Boyd, S.K., Christiansen, B.A., Guldberg, R.E., Jepsen, K.J., MĂźller, R., 2010. Guidelines for assessment of bone microstructure in rodents using microâcomputed tomography. Journal of Bone and Mineral Research 25, 1468–1486.

Boyde, A., Riggs, C.M., 1990. The quantitative study of the orientation of collagen in compact bone slices. Bone 11, 35 – 39.

Bromage, T.G., Goldman, H.M., McFarlin, S.C., Warshaw, J., Boyde, A., Riggs, C.M., 2003. Circularly polarized light standards for investigations of collagen fiber orientation in bone. Anat Rec B New Anat 274, 157–168.

Buehler, M., 2007. Molecular nanomechanics of nascent bone: fibrillar toughening by mineralization. Nanotechnology , 295102.

Burger, C., Zhou, H., Wang, H., Sics, I., Hsiao, B.S., Chu, B., Graham, L., Glimcher, M.J., 2008. Lateral packing of mineral crystals in bone collagen fibrils. Biophysical Journal 95, 1985–1992.

Burket, J., Gourion-Arsiquaud, S., Havill, L.M., Baker, S.P., Boskey, A.L., van der Meulen, M.C., 2011. Microstructure and nanomechanical properties in osteons relate to tissue and animal age. Journal of Biomechanics 44, 277–284.

Camacho, N., Rinnerthaler, S., Paschalis, E., Mendelsohn, R., Boskey, A., Fratzl, P., 1999. Complementary information on bone ultrastructure from scanning small angle x-ray scattering and fourier-transform infrared microspectroscopy. Bone 25, 287–293.

Canty, E., Kadler, K., 2005. Procollagen trafficking, processing and fibrillogenesis. Journal of Cell Science 118, 1341–1353.

Chevalier, Y., Pahr, D., Allmer, H., Charlebois, M., Zysset, P., 2007. Validation of a voxel-based fe method for prediction of the uniaxial apparent modulus of human trabecular bone using macroscopic mechanical tests and nanoindentation. Journal of Biomechanics 40, 3333–3340.

Cox, G., Kable, E., Jones, A., Fraser, I., Manconi, F., et.al., 2003. 3-dimensional imaging of collagen using second harmonic generation. Journal of Structural Biology 141, 53–62.

Crawley, M., 2005. Statistics. An introduction using R. John Wiley and Sons Ltd, Chichester, England.

Curnier, A., He, Q.C., Zysset, P., 1995. Conewise linear elastic materials. Journal of Elasticity 37, 1–38. 10.1007/BF00043417.

Cusack, S., Miller, A., 1979. Determination of the elastic constants of collagen by brillouin light scattering. Journal of Molecular Biology 135, 39–51.

Dall'Ara, E., Schmidt, R., Pahr, D., Varga, P., Chevalier, Y., Patsch, J., Kainberger, F., Zysset, P., 2010a. A nonlinear finite element model validation study based on a novel experimental technique for inducing anterior wedge-shape fractures in human vertebral bodies in vitro. Journal of Biomechanics 43, 2374–2380.

Dall'Ara, E., Schmidt, R., Zysset, P., 2010b. Microindentation can discriminate between damaged and intact human bone tissue, in: 17th Congress of the ESB, Edinburgh, Scotland.

Dall'Ara, E., Varga, P., Pahr, D., Zysset, P., 2011. A calibration methodology of qct bmd for human vertebral body with registered micro-ct images. Medical Physics 38, 2602–2608.

De Micheli, P., Witzel, U., 2011. Microstructural mechanical study of a transverse osteon under compressive loading: The role of fiber reinforcement and explanation of some geometrical and mechanical microscopic properties. Journal of Biomechanics 44, 1588–1592.

Donnelly, E., Williams, R.M., Downs, S.A., Dickinson, M.E., Baker, S.P., Van Der Meulen, M.C.H., 2006. Quasistatic and dynamic nanomechanical properties of cancellous bone tissue relate to collagen content and organization. Journal of Materials Research 21, 2106–2117.

Ebenstein, D.M., Pruitt, L.A., 2006. Nanoindentation of biological materials. Nano Today 1, 26–33.

Ehrlich, H., Koutsoukos, P., Demadis, K., Pokrovsky, O., 2009. Principles of demineralization: Modern strategies for the isolation of organic frameworks: Part Decalcification. Micron 40, 169 – 193.

Evans, E., Prior, B., Arngrimsson, S., Modlesky, C., Cureton, K., 2001. Relation of bone mineral density and content to mineral content and density of the fat-free mass. Journal of Applied Physiology 91, 2166–2172.

Fan, Z., Swadener, J.G., Rho, J.Y., Roy, M.E., Pharr, G.M., 2002. Anisotropic properties of human tibial cortical bone as measured by nanoindentation. Journal of Orthopaedic Research 20, 806–810.

Fischer-Cripps, A.C., 2002. Nanoindentation. Springer-Verlag New York.

Follet, H., Boivin, G., Rumelhart, C., Meunier, P.J., 2004. The degree of mineralization is a determinant of bone strength: a study on human calcanei. Bone 34, 783–789.

Franzoso, G., Zysset, P.K., 2009. Elastic anisotropy of human cortical bone secondary osteons measured by nanoindentation. Journal of Biomechanical Engineering 131, 021001–1–021001–11.

Fratzl, P., 2008. Collagen. Structure and Mechanics. Springer, New York, USA.

Fratzl, P., Gupta, H., Paschalis, E., Roschger, P., 2004. Structure and mechanical quality of the collagen-mineral nano-composite in bone. J. Mater. Chem. 14, 2115 – 2123.

Fratzl, P., Weinkamer, R., 2007. Nature's hierarchical materials. Progress in Materials Science 52, 1263–1334.

Fratzl-Zelman, N., Roschger, P., Fisher, J., Duong, L., Klaushofer, K., 2010. Effects of odanacatib on bone mineral density distribution (bmdd) in lumbar vertebrae and femora of ovariectomized adult rhesus monkeys: A qbei study. Bone 47, Supplement 1, S201–.

Fratzl-Zelman, N., Valenta, A., Roschger, P., Nader, A., Gelb, B., Fratzl, P., Klaushofer, K., 2004. Decreased Bone Turnover and Deterioration of Bone Structure in Two Cases of Pycnodysostosis. Journal of Clinical Endocrinology & Metabolism 89, 1538–1547.

Freeman, J.W., Silver, F.H., 2004. Elastic energy storage in unmineralized and mineralized extracellular matrices (ecms): A comparison between molecular modeling and experimental measurements. Journal of Theoretical Biology 229, 371–381.

Fritsch, A., Hellmich, C., 2007. Universal microstructural patterns in cortical and trabecular, extracellular and extravascular bone materials: Micromechanics-based prediction of anisotropic elasticity. Journal of Theoretical Biology 244, 597–620.

Gamsjaeger, S., Masic, A., Roschger, P., Kazanci, M., Dunlop, J., et.al., 2010. Cortical bone composition and orientation as a function of animal and tissue age in mice by raman spectroscopy. Bone 47, 392–399.

Gao, H., Ji, B., Jager, I., Arzt, E., Fratzl, P., 2003. Materials become insensitive to flaws at nanoscale: Lessons from nature. PNAS 100 (10), 5597–5600.

Gautieri, A., Vesentini, S., Redaelli, A., Buehler, M.J., 2011. Hierarchical structure and nanomechanics of collagen microfibrils from the atomistic scale up. Nano Letters 11, 757–766.

Gebhardt, W., 1906. Ueber funktionell wichtige anordnungsweisen der feineren und groeberen bauelemente des wirbeltierknochens. ii. spezieller teil. der bau der haversschen lamellensysteme und seine funktionelle bedeutung. Arch Entwickl Mech Org 20, 187–322.

Geday, M., Kaminsky, W., Lewis, J., Glazer, A., 2000. Images of absolute retardance $l\delta$n, using the rotating polariser method. Journal of Microscopy 198, 1–9.

Ghanbari, J., Naghdabadi, R., 2009. Nonlinear hierarchical multiscale modeling of cortical bone considering its nanoscale microstructure. Journal of Biomechanics 42, 1560 – 1565.

Giraud-Guille, M., 1998. Plywood structures in nature. Current Opinion in Solid State and Materials Science 3, 221–227.

Glimcher, M., 2006. Bone: Nature of the calcium phosphate crystals and cellular, structural, and physical chemical mechanisms in their formation. Reviews in Mineralogy and Geochemistry 64, 223–282.

Glimcher, M., Brickley-Parsons, D., Kossiva, D., 1979. Phosphopeptides and Îł-carboxyglutamic acid-containing peptides in calcified turkey tendon: Their absence in uncalcified tendon. Calcified Tissue International 27, 281–284. 10.1007/BF02441198.

Goldman, H.M., Bromage, T.G., Thomas, C.D.L., Clement, J.G., 2003. Preferred collagen fiber orientation in the human mid-shaft femur. The Anatomical Record Part A: Discoveries in Molecular, Cellular, and Evolutionary Biology 272A, 434–445.

Gouldstone, A., Chollacoop, N., Dao, M., Li, J., Minor, A.M., Shen, Y.L., 2007. Indentation across size scales and disciplines: Recent developments in experimentation and modeling. Acta Materialia 55, 4015–4039.

Grabner, B., Landis, W., Roschger, P., Rinnerthaler, S., Peterlik, H., Klaushofer, K., Fratzl, P., 2001. Age- and genotype-dependence of bone material properties in the osteogenesis imperfecta murine model (oim). Bone 29, 453–457.

Granke, M., Grimal, Q., Sadž″ed, A., Nauleau, P., Peyrin, F., Laugier, P., 2011. Change in porosity is the major determinant of the variation of cortical bone elasticity at the millimeter scale in aged women. Bone In Press, Uncorrected Proof, –.

Gruber, H.E., 1992. Adaptations of goldner's masson trichrome stain for the study of undecalcified plastic embedded bone. Biotech Histochem 67, 30–34.

Gupta, H., Messmer, P., Roschger, P., Bernstorff, S., Klaushofer, K., Fratzl, P., 2004. Synchrotron diffraction study of deformation mechanisms in mineralized tendon. Phys. Rev. Lett. 93, 158101.

Gupta, H., Wagermaier, W., Zickler, G., Raz-BenAroush, D., Funari, S., Roschger, P., Wagner, H., Fratzl, P., 2005. Nanoscale deformation mechanisms in bone. Nano Lett. 5, 2108–2111.

Hasegawa, K., Turner, C., Burr, D., 1994. Contribution of collagen and mineral to the elastic anisotropy of bone. Calcified Tissue International 55, 381–386.

Hellmich, C., Ulm, F., 2002. Micromechanical model for ultrastructural stiffness of mineralized tissues. J. Engrg. Mech. 128, 898–908.

Hengsberger, S., Boivin, G., Zysset, P.K., 2002a. Morphological and mechanical properties of bone structural units: A two-case study. JSME International Journal Series C Mechanical Systems, Machine Elements and Manufacturing 45, 936–943.

Hengsberger, S., Kulik, A., Zysset, P., 2002b. Nanoindentation discriminates the elastic properties of individual human bone lamellae under dry and physiological conditions. Bone 30, 178 – 184.

Hodge, A., Petruska, A., 1963. Recent studies with the electron microscope on ordered aggregates of the tropocollagen molecule. Aspects of Protein Structure , 289–300.

Huiskes, R., Chao, E., 1983. A survey of finite element analysis in orthopedic biomechanics: The first decade. Journal of Biomechanics 16, 385–409.

Jaeger, A., Bader, T., Hofstetter, K., Eberhardsteiner, J., 2011. The relation between indentation modulus, microfibril angle, and elastic properties of wood cell walls. Composites Part A: Applied Science and Manufacturing 42, 677–685.

Jaeger, I., Fratzl, P., 2000. Mineralized collagen fibrils: A mechanical model with a staggered arrangement of mineral particles. Biophysical Journal 79, 1737–1746.

Kabel, J., van Rietbergen, B., Odgaard, A., Huiskes, R., 1999. Constitutive relationships of fabric, density, and elastic properties in cancellous bone architecture. Bone 25, 481–486.

Kalmey, J.K., Lovejoy, C.O., 2002. Collagen fiber orientation in the femoral necks of apes and humans: do their histological structures reflect differences in locomotor loading? Bone 31, 327–332.

Kaminsky, W., Gunn, E., Sours, R., Kahr, B., 2007. Simultaneous false-colour imaging of birefringence, extinction and transmittance at camera speed. J Microsc 228, 153–64.

Kazanci, M., Roschger, P., Paschalis, E., Klaushofer, K., Fratzl, P., 2006. Bone osteonal tissues by raman spectral mapping: Orientation-composition. Journal of Structural Biology 156, 489–496.

Kazanci, M., Wagner, H., Manjubala, N., Gupta, H., Paschalis, E., et.al., 2007. Raman imaging of two orthogonal planes within cortical bone. Bone 41, 456–461.

Kerschnitzki, M., Wagermaier, W., Roschger, P., Seto, J., Shahar, R., Duda, G.N., Mundlos, S., Fratzl, P., 2011. The organization of the osteocyte network mirrors the extracellular matrix orientation in bone. J Struct Biol 173, 303–311.

Keyak, J.H., 2000. Nonlinear finite element modeling to evaluate the failure load of the proximal femur. J Orthop Res 18, 337.

Keyak, J.H., 2001. Improved prediction of proximal femoral fracture load using nonlinear finite element models. Med Eng Phys 23, 165–173.

Keyak, J.H., Fourkas, M.G., Meagher, J.M., Skinner, H.B., 1993. Validation of an automated method of three-dimensional finite element modelling of bone. J Biomed Eng 15, 505–509.

Knott, L., Bailey, A.J., 1998. Collagen cross-links in mineralizing tissues: A review of their chemistry, function, and clinical relevance. Bone 22, 181–187.

Knott, L., Tarlton, J., Bailey, A., 1997. Chemistry of collagen cross-linking : biochemical changes in collagen during the partial mineralization of turkey leg tendon. Biochemical Journal 322, 535 – 542.

Kohler, D.M., Crenshaw, M.A., Arsenault, A.L., 1995. Three-dimensional analysis of mineralizing turkey leg tendon: Matrix vesicle-collagen relationships. Matrix Biology 14, 543–552.

Landis, W., Hodgens, K., Song, M., Arena, J., Kiyonaga, S., Marko, M., Owen, C., McEwen, B., 1996. Mineralization of collagen may occur on fibril surfaces: Evidence from conventional and high-voltage electron microscopy and three-dimensional imaging. Journal of Structural Biology 117, 24–35.

Landis, W., Silver, F., 2002. The structure and function of normally mineralizing avian tendons. Comparative Biochemistry and Physiology - Part A: Molecular & Integrative Physiology 133, 1135–1157.

Landis, W.J., 1986. A study of calcification in the leg tendons from the domestic turkey. Journal of Ultrastructure and Molecular Structure Research 94, 217–238.

Lees, S., Hanson, B., Page, E., 1996. Some acoustical properties of the otic bones of a fin whale. The Journal of the Acoustical Society of America 99, 2421–2427.

Lees, S., Page, E.A., 1992. A study of some properties of mineralized turkey leg tendon. Connect Tissue Res 28, 263–287.

Lees, S., Prostak, K.S., Ingle, V.K., Kjoller, K., 1994. The loci of mineral in turkey leg tendon as seen by atomic force microscope and electron microscopy. Calcified Tissue International 55, 180–189.

LeGeros, R., Trautz, O., Klein, E., LeGeros, J., 1969. Two types of carbonate substitution in the apatite structure. Experientia 25, 5 – 7.

Lewis, G., Nyman, J.S., 2008. The use of nanoindentation for characterizing the properties of mineralized hard tissues: state-of-the art review. Journal of Biomedical Materials Research Part B: Applied Biomaterials 87, 288–303.

Liu, A., Kuboki, Y., 1996. Changes of noncollagenous extracellular matrix in turkey leg tendon during calcification. Journal of hard tissue biology 5, 201–206.

Liu, D., Weiner, S., Wagner, H., 1999. Anisotropic mechanical properties of lamellar bone using miniature cantilever bending specimens. Journal of Biomechanics 32, 647–654. Tolle Bilder in hoher Aufloesung von Bruchflaechen von Knochen im .pdf.

Manjubala, I., Liu, Y., Epari, D., Roschger, P., Schell, H., Fratzl, P., Duda, G., 2009. Spatial and temporal variations of mechanical properties and mineral content of the external callus during bone healing. Bone 45, 185–192.

Martin, R., Lau, S., Mathews, P., Gibson, V., Stover, S., 1996. Collagen fiber organization is related to mechanical properties and remodeling in equine bone a comparsion of two methods. Journal of Biomechanics 29, 1515–1521.

Martin, R.B., Ishida, J., 1989. The relative effects of collagen fiber orientation, porosity, density, and mineralization on bone strength. Journal of biomechanics 2, 419–426.

Mori, T., Tanaka, K., 1973. Average stress in matrix and average elastic energy of materials with misfitting inclusions. Acta Metallurgica 21, 571–574.

Nikolov, S., Raabe, D., 2008. Hierarchical modeling of the elastic properties of bone at submicron scales: The role of extrafibrillar mineralization. Biophysical Journal 94, 4220–4232.

Ohman, C., Baleani, M., Perilli, E., Dall'Ara, E., Tassani, S., Baruffaldi, F., Viceconti, M., 2007. Mechanical testing of cancellous bone from the femoral head: Experimental errors due to off-axis measurements. Journal of Biomechanics 40, 2426–2433.

Oliver, W.C., Pharr, G.M., 1992. An improved technique for determining hardness and elastic modulus using load and displacement sensing indentation experiments. J Mater Res 7, 1564–1583.

Olszta, M.J., Cheng, X., Jee, S.S., Kumar, R., Kim, Y.Y., Kaufman, M.J., Douglas, E.P., Gower, L.B., 2007. Bone structure and formation: A new perspective. Materials Science and Engineering: R: Reports 58, 77 – 116.

Orwoll, E.S., Marshall, L.M., Nielson, C.M., Cummings, S.R., Lapidus, J., Cauley, J.A., Ensrud, K., Lane, N., Hoffmann, P.R., Kopperdahl, D.L., Keaveny, T.M., in Men Study Group, O.F., 2009. Finite element analysis of the proximal femur and hip fracture risk in older men. J Bone Miner Res 24, 475–483.

Oyen, M.L., 2006. Nanoindentation hardness of mineralized tissues. Journal of Biomechanics 39, 2699 – 2702.

Oyen, M.L., 2011. Handbook of nanoindentation with biological applications. Pan Stanford, Singapore.

Pajdzik, L.A., M., G.A., 2006. Three-dimensional birefringence imaging with a microscope tilting-stage. uniaxial crystals. Journal of Applied Crystallography 39, 326–227.

Paschalis, E., Tatakis, D., Robins, S., Fratzl, P., Manjubala, I., Zoehrer, R., Gamsjaeger, S., Buchinger, B., Roschger, A., Phipps, R., Boskey, A., Dall'Ara, E., Varga, P., Zysset, P., Klaushofer, K., Roschger, P., 2011. Lathyrism-induced alterations in collagen cross-links influence the mechanical properties of bone material without affecting the mineral. Bone , –.

Pistoia, W., van Rietbergen, B., LochmĂźller, E.M., Lill, C., Eckstein, F., RĂźegsegger, P., 2002. Estimation of distal radius failure load with micro-finite element analysis models based on three-dimensional peripheral quantitative computed tomography images. Bone 30, 842–848.

Preininger, B., Checa, S., Molnar, F.L., Fratzl, P., Duda, G.N., Raum, K., 2011. Spatial-temporal mapping of bone structural and elastic properties in a sheep model following osteotomy. Ultrasound in Medicine & Biology 37, 474–483.

Prostak, K.S., Lees, S., 1996. Visualization of crystal-matrix structure. in situ demineralization of mineralized turkey leg tendon and bone. Calcified Tissue International 59, 474–479.

Ramasamy, J., Akkus, O., 2007. Local variations in the micromechanical properties of mouse femur: The involvement of collagen fiber orientation and mineralization. Journal of Biomechanics 40, 910–918.

Raum, K., Leguerney, I., Chandelier, F., Bossy, E., Talmant, M., Saied, A., Peyrin, F., Laugier, P., 2005. Bone microstructure and elastic tissue properties are reflected in qus axial transmission measurements. Ultrasound in Medicine & Biology 31, 1225–1235.

Raum, K., Leguerney, I., Chandelier, F., Talmant, M., Saied, A., Peyrin, F., Laugier, P., 2006. Site-matched assessment of structural and tissue properties of cortical bone using scanning acoustic microscopy and synchrotron radiation uct. Physics in Medicine and Biology 51, 733–746.

Reisinger, A., Pahr, D., Zysset, P., 2010. Sensitivity analysis and parametric study of elastic properties of an unidirectional mineralized bone fibril-array using mean field methods. Biomech Model Mechanobiol .

Reisinger, A.G., Pahr, D.H., Zysset, P.K., 2011. Principal stiffness orientation and degree of anisotropy of human osteons based on nanoindentation in three distinct planes. Journal of the Mechanical Behavior of Biomedical Materials , –.

Rho, J., Currey, J., Zioupos, P., Pharr, G., 2001. The anisotropic Young's modulus of equine secondary osteones and interstitial bone determined by nanoindentation. J Exp Biol 204, 1775–1781.

Rho, J., Kuhn-Spearing, L., Zioupos, P., 1998. Mechanical properties and the hierarchical structure of bone. Medical Engineering & Physics 20, 92–102.

Rho, J.Y., Ashman, R.B., Turner, C.H., 1993. Young's modulus of trabecular and cortical bone material: Ultrasonic and microtensile measurements. Journal of Biomechanics 26, 111–119.

Rho, J.Y., Zioupos, P., Currey, J.D., Pharr, G.M., 1999. Variations in the individual thick lamellar properties within osteons by nanoindentation. Bone 25, 295–300.

van der Rijt, J., van der Werf, K., Bennink, M., Dijkstra, P., Feijen, J., 2006. Micromechanical testing of individual collagen fibrils. Macromolecular Bioscience 6, 697–702.

Roschger, P., Eschberger, J., Plenk, H.J., 1993. Formation of ultracracks in methacrylate-embedded undecalcified bone samples by exposure to aqueous solutions. Cells and Materials 3, 361–365.

Roschger, P., Fratzl, P., Eschberger, J., Klaushofer, K., 1998. Validation of quantitative backscattered electron imaging for the measurement of mineral density distribution in human bone biopsies. Bone 23, 319–326.

Roschger, P., Gupta, H.S., Berzlanovich, A., Ittner, G., Dempster, D.W., Fratzl, P., Cosman, F., Parisien, M., Lindsay, R., Nieves, J.W., Klaushofer, K., 2003. Constant mineralization density distribution in cancellous human bone. Bone 32, 316–323.

Roschger, P., Jr., H.P., Klaushofer, K., Eschberger, J., 1995. A new scanning electron microscopy approach to the quantification of bone mineral distribution: backscattered electron image grey-levels correlated to calcium kα-line intensities. Scanning Microscopy 9, 75 – 88.

Roschger, P., Rinnerthaler, S., Yates, J., Rodan, G., Fratzl, P., Klaushofer, K., 2001. Alendronate increases degree and uniformity of mineralization in cancellous bone and decreases the porosity in cortical bone of osteoporotic women. Bone 29, 185–191.

Rubin, M.A., Rubin, J., Jasiuk, I., 2004. Sem and tem study of the hierarchical structure of c57bl/6j and c3h/hej mice trabecular bone. Bone 35, 11–20.

Ruffoni, D., Fratzl, P., Roschger, P., Klaushofer, K., Weinkamer, R., 2007. The bone mineralization density distribution as a fingerprint of the mineralization process. Bone 40, 1308–1319.

Sasaki, N., Tagami, A., Goto, T., Taniguchi, M., Nakata, M., Hikichi, K., 2002. Atomic force microscopic studies on the structure of bovine femoral cortical bone at the collagen fibril-mineral level. Journal of Materials Science: Materials in Medicine 13, 333–337.

Sevostianov, I., Kachanov, M., 2000. Impact of the porous microstructure on the overall elastic properties of the osteonal cortical bone. Journal of Biomechanics 33, 881–888.

Shu, J.Y., Fleck, N.A., 1998. The prediction of a size effect in microindentation. International Journal of Solids and Structures 35, 1363–1383.

Siegmund, T., Allen, M., Burr, D., 2008. Failure of mineralized collagen fibrils: Modeling the role of collagen cross-linking. Journal of Biomechanics 41, 1427–1435.

Silver, F., Freeman, J., Horvath, I., Landis, W., 2001. Molecular basis for elastic energy storage in mineralized tendon. Biomacromolecules 2, 750–756.

Silver, F.H., Christiansen, D., Snowhill, P.B., Chen, Y., Landis, W.J., 2000. The role of mineral in the storage of elastic energy in turkey tendons. Biomacromolecules 1, 180–185.

Siperko, L.M., Landis, W.J., 2001. Aspects of mineral structure in normally calcifying avian tendon. Journal of Structural Biology 135, 313–320.

Skedros, J.G., Mendenhall, S.D., Kiser, C.J., Winet, H., 2009. Interpreting cortical bone adaptation and load history by quantifying osteon morphotypes in circularly polarized light images. Bone 44, 392–403.

Spiesz, E.M., Kaminsky, W., Zysset, P.K., 2011a. A quantitative collagen fibers orientation assessment using birefringence measurements: calibration and application to human osteons. Journal of Structural Biology , –.

Spiesz, E.M., Roschger, P., Zysset, P.K., 2011b. Influence of mineralization and microporosity on tissue elasticity - experimental and numerical investigation on mineralized turkey leg tendons. Calcified Tissue International In preparation.

Steiger, J.H., 1980. Tests for comparing elements of a correlation matrix. Psychological Bulletin 87, 245–251.

Stroem, O., BorgstrĂśm, F., Kanis, J., Compston, J., Cooper, C., McCloskey, E.V., JĂśnsson, B., 2011. Osteoporosis: Burden, health care provision and opportunities in the european union archives of osteoporosis (2011). DOI 10.1007/s11657-011-0060-1 .

Swadener, J.G., Pharr, G.M., 2001. Indentation of elastically anisotropic half-spaces by cones and parabolae of revolution. Philosophical Magazine A 81, 447–466.

Traub, W., Arad, T., Weiner, S., 1989. Three-dimensional ordered distribution of crystals in turkey tendon collagen fibers. Proc Natl Acad Sci U S A 86, 9822–9826.

Turner, C.H., Chandran, A., Pidaparti, R.M.V., 1995. The anisotropy of osteonal bone and its ultrastructural implications. Bone 17, 85–89.

Valenta, A., Roschger, P., Fratzl-Zelman, N., Kostenuik, P., Dunstan, C., Fratzl, P., Klaushofer, K., 2005. Combined treatment with pth (1â34) and opg increases bone volume and uniformity of mineralization in aged ovariectomized rats. Bone 37, 87–95.

Van Rietbergen, B., Odgaard, A., Kabel, J., Huiskes, R., 1996. Direct mechanics assessment of elastic symmetries and properties of trabecular bone architecture. Journal of Biomechanics 29, 1653–1657.

Varga, P., 2010. Prediction of distal radius fracture loadusing HR-pQCT-based finite element analysis. Ph.D. thesis. Vienna University of Technology.

Varga, P., Baumbach, S., Pahr, D., Zysset, P., 2009. Validation of an anatomy specific finite element model of collesâ fracture. Journal of Biomechanics 42, 1726–1731.

Varga, P., Pahr, D.H., Baumbach, S., Zysset, P.K., 2010. Hr-pqct based fe analysis of the most distal radius section provides an improved prediction of colles' fracture load in vitro. Bone 47, 982–988.

Varga, P., Zysset, P., 2009. Assessment of volume fraction and fabric in the distal radius using hr-pqct. Bone 45, 909–917.

Verhulp, E., van Rietbergen, B., Huiskes, R., 2006. Comparison of micro-level and continuum-level voxel models of the proximal femur. Journal of Biomechanics 39, 2951–2957.

Voyiadjis, G., Peters, R., 2010. Size effects in nanoindentation: an experimental and analytical study. Acta Mechanica 211, 131–153.

Wagermaier, W., Gupta, H.S., Gourrier, A., Burghammer, M., Roschger, P., Fratzl, P., 2006. Spiral twisting of fiber orientation inside bone lamellae. Biointerphases 1, 1–5.

Weiner, S., Arad, T., Sabanay, I., Traub, W., 1997. Rotated plywood structure of primary lamellar bone in the rat: Orientations of the collagen fibril arrays. Bone 20, 509–514.

Weiner, S., Traub, W., Wagner, H., 1999. Lamellar bone: Structure-function relations. Journal of Structural Biology 126, 241–255.

Willems, N.M., Mulder, L., Bank, R.A., Grďż″nheid, T., den Toonder, J.M., et.al., 2011. Determination of the relationship between collagen cross-links and the bone-tissue stiffness in the porcine mandibular condyle. Journal of Biomechanics 44, 1132–1136.

de With, G., Van Dijk, H., Hattu, N., K., P., 1981. Preparation, microstructure and mechanical properties of dense polycrystalline hydr. Journal of Materials Science 16, 1592–1598.

Wolfram, U., Wilke, H.J., Zysset, P.K., 2010a. Rehydration of vertebral trabecular bone: influences on its anisotropy, its stiffness and the indentation work with a view to age, gender and vertebral level. Bone 46, 348–354.

Wolfram, U., Wilke, H.J., Zysset, P.K., 2010b. Valid μ finite element models of vertebral trabecular bone can be obtained using tissue properties measured with nanoindentation under wet conditions. Journal of Biomechanics 43, 1731–1737.

Wu, Z.Y., Hill, R.G., Yue, S., Nightingale, D., Lee, P.D., Jones, J.R., 2011. Melt-derived bioactive glass scaffolds produced by a gel-cast foaming technique. Acta Biomaterialia 7, 1807–1816.

Yao, H., Ouyang, L., Ching, W., 2007. Ab initio calculation of elastic constants of ceramic crystals. Journal of the American Ceramic Society 90, 3194–3204.

Zebaze, R.M., Jones, A.C., Pandy, M.G., Knackstedt, M.A., Seeman, E., 2011. Differences in the degree of bone tissue mineralization account for little of the differences in tissue elastic properties. Bone 48, 1246–1251.

Zhang, J., Michalenko, M.M., Kuhl, E., Ovaert, T.C., 2010. Characterization of indentation response and stiffness reduction of bone using a continuum damage model. Journal of the Mechanical Behavior of Biomedical Materials 3, 189–202.

Zhang, J., Niebur, G.L., Ovaert, T.C., 2008. Mechanical property determination of bone through nano- and micro-indentation testing and finite element simulation. Journal of Biomechanics 41, 267–275.

Ziv, V., Wagner, H.D., Weiner, S., 1996. Microstructure-microhardness relations in parallel-fibered and lamellar bone. Bone 18, 417–428.

Zysset, P., 2009. Indentation of bone tissue: a short review. Osteoporosis International 20, 1049–1055.

Zysset, P., Guo, X., Hoffler, C., Moore, K., Goldstein, S., 1999. Elastic modulus and hardness of cortical and trabecular bone lamellae measured by nanoindentation in the human femur. Journal of Biomechanics 32, 1005–1012.

Curriculum Vitae
Ewa M. Spiesz (Cichy)

Born: 13.04.1983 in Oświęcim, Poland
E-mail: ewa.spiesz@ilsb.tuwien.ac.at

Education

2008–2011	**Doctor of Engineering Sciences** in Biomechanics, Vienna University of Technology, Department of Mechanical and Industrial Engineering, Institute of Lightweight Design and Structural Biomechanics, Austria
2009	**Visiting scholar**, University of Washington, Seattle, WA, USA
2002–2007	**Master of Science** in Materials Science (Biomaterials and Composites), AGH The University of Science and Technology, Cracow, Poland
2002–2007	**Master of Science** in Chemical Technology (Glass and Ceramics), AGH The University of Science and Technology, Cracow, Poland
2006–2007	**Socrates-Erasmus students exchange**, Universitat Jaume I, Castellon, Spain
2006	**Research project**, Imperial College London, Department of Materials, United Kingdom

Honours and Awards

2008	Young Investigator Poster Award from the Austrian Society of Biomedical Engineering, Vienna, Austria
2007	Prizewinner of the Primus Inter Pares contest and obtaining a title of the best student of AGH the University of Science and Technology and the best student of the Malopolskie State, Warsaw, Poland
2005, 2006	Rector's Prize for outstanding achievements in learning and the title of the best student of Chemical Technology Department, Cracow, Poland
2004	Rector's Prize for outstanding achievements in learning and the title of the best student of Materials Science Department, Cracow, Poland
2002–2007	Scholarschips for outstanding achievements in learning awarded after each year of undergraduate and graduate study, Cracow, Poland

Publications

E. M. Spiesz, A. G. Reisinger, P. Roschger, Ph. K. Zysset, "Experimental validation of a mean filed model of mineralized collagen fiber arrays at two levels of hierarchy", In preparation, 2011.

A.G. Reisinger, E.M. Spiesz, W. Kaminsky, P. Roschger, D. H. Pahr, P.K. Zysset, "Variability of Indentation Modulus of Human Lamellar Bone Cannot be Explained by Fibril Orientation and Mineralization", In preparation, 2011.

E. M. Spiesz, A. G. Reisinger, P. Roschger, Ph. K. Zysset, "Experimental validation of a multiscale model of mineralized collagen fibers at two levels of hierarchy", In *Osteoporosis International, 22, 4, 561-666; Proc. IOF Regionals - 2nd Asia-Pacific Osteoporosis and Bone Meeting in conjunction with the ANZBMS Annual Scientific Meeting 2011*, Gold Coast, Australia, 2011.

E. M. Spiesz, W. Kaminsky, Ph. K. Zysset, "A quantitative collagen fibers orientation assessment using birefringence measurements: calibration and application to human osteons", Accepted in *Journal of Structural Biology*, 2011.

E. M. Spiesz, Ph. K. Zysset, "Elastic anisotropy of mineralized turkey leg tendon measured using two-directional indentation. Effects of hydration state and indentation depth", Submitted to *Journal of Mechanical Behaviour of Biomedical Materials*, 2011.

E. M. Spiesz, P. Roschger, Ph. K. Zysset, "Influence of mineralization and microporosity on tissue elasticity. Experimental and numerical investigation on mineralized turkey leg tendons", Accepted in *Calcified Tissue International*, 2011.

E. M. Spiesz, W. Kaminsky, Ph. K. Zysset, "Quantitative assessment of bone collagen fibers orientation using birefringence measurements", In *Proc. International Society of Biomechanics Conference*, Brussels, Belgium, 2011.

A. Gerisch, S. Tiburtius, Q. Grimal, F. Molnar, E. Spiesz, M. Langner, Ph. Zysset, F. Peyrin, K. Raum "A micromechanical model of the mineralized collagen fibril bundle with application to mineralized turkey leg tendon data", In *Proc. International Congress on Industrial and Applied Mathematics*, Vancouver, Canada, 2011.

E. Cichy, A. Reisinger, P. Roschger, Ph. K. Zysset, "Morphology-elasticity relationships in mineralized turkey leg tendon", In *Proc. 44th Annual Conference of the German Association of Biomedical Engineering (DGBMT)*, Rostock, Germany, 2010.

E. Cichy, W. Kaminsky, Ph. K. Zysset, "Bone collagen fibers orientation assessment using birefringence measurements", In *Proc. Northwest Biomechanics Symposium*, Seattle, WA, 2010.

E. Cichy, M. Schnieder, Ph. K. Zysset, "Transverse-isotropic properties of mineralized collagen fibers: dependence of nanoindentation depth and hydration state", In *Proc. Junior Scientists Conference 2010, H. Kaiser, R. Kirner (Hrg.)*, ISBN: 978-3-200-01797-9; S. 269 - 270. Vienna, Austria, 2010.

E. Cichy, P. Roschger, Ph. Zysset, "Micromechanical and structural analysis of mineralized turkey leg tendon (MTLT)", In *Proc. 3rd Viennese Symposium on Biomaterials*, Vienna, Austria, 2008.

J. Laska, M. Blazewicz, A. Fital, E. Cichy, Malgorzata Martowicz, "Poly(methyl methacrylate) nanocomposites obtained by suspension and block polymerization", In *Engineering of Biomaterials*, Polish Association for Biomaterials, vol. 11, 74, 15-22. ISSN 1429-7248, 2008.